Title
Angle-resolved Photoemission Studies of a Doped Bilayer Iridate

Author
Affeldt, Gregory

Publication Date
2018

Angle-resolved Photoemission Studies of a Doped Bilayer Iridate

by

Gregory Affeldt

A dissertation submitted in partial satisfaction of the

requirements for the degree of

Doctor of Philosophy

in

Physics

in the

Graduate Division

of the

University of California, Berkeley

Committee in charge:

Professor Alessandra Lanzara, Chair
Professor James Analytis
Professor Lane Martin

Fall 2018

Angle-resolved Photoemission Studies of a Doped Bilayer Iridate

Abstract

Angle-resolved Photoemission Studies of a Doped Bilayer Iridate

by

Gregory Affeldt

Doctor of Philosophy in Physics

University of California, Berkeley

Professor Alessandra Lanzara, Chair

Interest has been rising in systems, such as the iridates, where both spin-orbit coupling and Coulomb correlations play a prominent role, with theoretical proposals for a variety of exotic states. One such state, the spin-orbit Mott insulator, was discovered by Kim et al in Sr_2IrO_4 using angle-resolved photoemission spectroscopy, the experimental technique used in this work. Such states were later discovered in a variety of materials, including $Sr_3Ir_2O_7$, Na_2IrO_3, and $RuCl_3$ and provide a concrete testing ground for the physics of Mott insulators. This includes, naturally, the search for nearby exotic states which are the frequent companion of the Mott state. Indeed, significant attention has been given to doped Sr_2IrO_4 as an analog to the cuprate high-temperature superconductors, and to Na_2IrO_3, Li_2IrO_3, and $RuCl_3$ as candidates for hosting a spin-liquid state.

This work focuses on $(Sr_{1-x}La_x)_3Ir_2O_7$, which is notable in the weakness of its parent Mott state and thus its likely proximity to other ground states. The substitution of La on the Sr site adds electrons as carriers to the system. This eventually destroys the insulating state, though manifestations of both Coulomb correlations and spin-orbit coupling remain well beyond the insulator-metal transition. Chapter 1 covers the physics relevant to the ground state of $(Sr_{1-x}La_x)_3Ir_2O_7$, starting from the effects of Coulomb correlations and spin-orbit coupling in general and including an overview of the current experimental results in doped and undoped Sr_2IrO_4 and $Sr_3Ir_2O_7$. Chapter 2 summarizes the theory of (spin- and) angle-resolved photoemission spectroscopy (ARPES), and describes analysis techniques used in the later chapters. The main experimental results of the work obtained using spin-integrated photoemission are in chapter 3, including evidence for a novel ground state in lightly-doped $(Sr_{1-x}La_x)_3Ir_2O_7$ and a thorough exploration of the evolving role of Coulomb correlations with doping. Chapter 4 goes into more recent results from several spin-resolved ARPES measurements and their possible implications, including some outstanding puzzles in the results.

Contents

Contents **ii**

List of Figures **iv**

1 Introduction **1**
- 1.1 Single-electron band physics 1
  - 1.1.1 Coulomb correlations and the Hubbard model 4
  - 1.1.2 Spin-orbit coupling 5
- 1.2 Ruddlesden-Popper Iridates: Sr_2IrO_4 and $Sr_3Ir_2O_7$ 10
  - 1.2.1 Formation of the spin-orbit Mott state 11
  - 1.2.2 Theory of Magnetism in j_{eff} states 12
  - 1.2.3 Layer-dependent metal-insulator transition 14
  - 1.2.4 Pseudogaps and possible superconductivity in Sr_2IrO_4 15
- 1.3 Properties of doped $(Sr_{1-x}La_x)_3Ir_2O_7$ 17
  - 1.3.1 Transport properties 17
  - 1.3.2 Magnetic structure and excitations 18
  - 1.3.3 Optical properties 22

2 Angle-resolved photoemission spectroscopy **28**
- 2.1 Theory of ARPES 28
- 2.2 Experimental considerations 30
  - 2.2.1 Sample surface 31
  - 2.2.2 Matrix element effects 31
  - 2.2.3 Out-of-plane momentum considerations 32
  - 2.2.4 Sample charging and space charging 34
- 2.3 ARPES analysis 34
  - 2.3.1 Analysis methods 35
  - 2.3.2 Application to gap extraction 36
- 2.4 Spin-resolved ARPES 40
  - 2.4.1 Spin-dependent matrix elements 41

3 Electronic structure of $(Sr_{1-x}La_x)_3Ir_2O_7$ **43**

- 3.1 Introduction: Electronic structure of $Sr_3Ir_2O_7$ . . . 43
- 3.2 Band structure effects . . . 45
  - 3.2.1 Population and evolution of the conduction band . . . 46
  - 3.2.2 Effects in the valence band . . . 49
- 3.3 Correlation-related changes . . . 52
  - 3.3.1 Reduction in the Mott gap . . . 52
  - 3.3.2 Enhancement of band masses . . . 53
- 3.4 Effects of spin-orbit coupling and bilayer splitting . . . 56
- 3.5 Low energy spectral weight suppression . . . 57
  - 3.5.1 Doping dependence . . . 57
  - 3.5.2 Temperature dependence . . . 59
  - 3.5.3 Momentum dependence . . . 61
- 3.6 Temperature-dependent coherence loss . . . 63
- 3.7 Electronic phase diagram . . . 65

4 Spin-polarized photoemission from $(Sr_{1-x}La_x)_3Ir_2O_7$ 68
- 4.1 Unusual momentum dependence . . . 69
- 4.2 Doping dependence . . . 72
- 4.3 Photon polarization dependence . . . 73
- 4.4 Photon energy dependence . . . 74
- 4.5 Conclusion . . . 74

Bibliography 77

List of Figures

1.1 Phase diagram of ground states with spin-orbit coupling and Coulomb correlations, from [9] . . . 2
1.2 Antiferromagnetic order in Mott insulators . . . 5
1.3 Spin-orbit coupling in semiconductors . . . 7
1.4 Schematic of the Rashba effect . . . 8
1.5 Effective magnetic field for the linear Dresselhaus effect . . . 9
1.6 Local Rashba effect . . . 10
1.7 Crystal structure of Ruddlesden-Popper iridates . . . 11
1.8 Schematic of energy scales in a spin-orbit Mott insulator . . . 13
1.9 Geometries considered for superexchange in iridate systems, from [20] . . . 14
1.10 Layer-dependent metal-insulator transition in RP iridates. (a), (b): Optical conductivity for single crystal Sr_2IrO_4 and $Sr_3Ir_2O_7$, respectively. (c): Optical conductivity for thin-film $SrIrO_3$. (d): Schematic of low-energy features in the optical conductivity. . . . 16
1.11 Psuedogap in Sr_2IrO_4 . . . 17
1.12 Transport measurements of $(Sr_{1-x}La_x)_3Ir_2O_7$ . . . 18
1.13 Crystallographic and magnetic structure of $Sr_3Ir_2O_7$ . . . 19
1.14 Spin flop transition in $(Sr_{1-x}La_x)_3Ir_2O_7$ and Sr_2IrO_4 . . . 20
1.15 Evolution of antiferromagnetism in $(Sr_{1-x}La_x)_3Ir_2O_7$. . . . 21
1.16 Phase diagram of $(Sr_{1-x}La_x)_3Ir_2O_7$ from scattering and transport . . . 22
1.17 Magnon dispersion in $Sr_3Ir_2O_7$ . . . 23
1.18 Magnon dispersion in $(Sr_{1-x}La_x)_3Ir_2O_7$ . . . 23
1.19 Optical conductivity of $Sr_3Ir_2O_7$ . . . 24
1.20 Phonon modes in $Sr_3Ir_2O_7$ . . . 25
1.21 Ultrafast reflectivity oscillations in metallic $(Sr_{1-x}La_x)_3Ir_2O_7$ . . . 27

2.1 Inelastic mean free path for electrons in various materials . . . 32
2.2 ARPES scattering geometry . . . 33
2.3 Simulated ARPES spectrum for gap determination . . . 37
2.4 Using EDC peak analysis to find a band position . . . 38
2.5 Using MDC analysis to find a band edge . . . 39

3.1 Dispersion in undoped $Sr_3Ir_2O_7$ 44
3.2 Schematic of carrier addition in a Mott insulator 45
3.3 Fermi surface of $(Sr_{0.94}La_{0.06})_3Ir_2O_7$ 46
3.4 Dispersion in $(Sr_{0.94}La_{0.06})_3Ir_2O_7$ 47
3.5 Lifschitz-like transition in $(Sr_{1-x}La_x)_3Ir_2O_7$ 48
3.6 Evolution of conduction band with doping 49
3.7 Near E_F dispersion for $(Sr_{1-x}La_x)_3Ir_2O_7$ 50
3.8 Constant energy maps for $(Sr_{1-x}La_x)_3Ir_2O_7$ samples 51
3.9 Doping dependence of the Mott gap in $(Sr_{1-x}La_x)_3Ir_2O_7$ 53
3.10 Effective masses of near-E_F bands 54
3.11 Doping dependence of band renormalization in cuprates and iridates 55
3.12 X and Γ band locations in $(Sr_{1-x}La_x)_3Ir_2O_7$ 56
3.13 Conduction band dispersions in $(Sr_{1-x}La_x)_3Ir_2O_7$ 58
3.14 Doping dependence of the spectral weight suppression 59
3.15 Temperature dependence of the spectral weight suppression 60
3.16 Thermal shifts of band features in $(Sr_{1-x}La_x)_3Ir_2O_7$ 61
3.17 Momentum dependence of the observed spectral weight suppression 62
3.18 Temperature dependent coherence loss in $(Sr_{1-x}La_x)_3Ir_2O_7$ 64
3.19 Temperature cycle for coherent peak 65
3.20 ARPES extended phase diagram 67

4.1 Momentum dependence of spin polarization in $(Sr_{1-x}La_x)_3Ir_2O_7$ 70
4.2 Fine momentum dependence of spin polarization near M 71
4.3 Doping dependence of the spin polarization at the X point 72
4.4 Spin flipping in $(Sr_{1-x}La_x)_3Ir_2O_7$ 73
4.5 Photon energy dependence of the observed spin signal 75

Acknowledgments

In coming to the end of my time in graduate school, I am humbled by and grateful for how much help and support I have received from so many people along the way. First, I offer my heartfelt thanks to my advisor, Alessandra Lanzara. As a scientist, her vision in seeking out and focusing on interesting questions and her ability to find the right collaborators to get a project done were invaluable. As a mentor, I have appreciated her drive to keep moving toward our goals, as well as her intuition for when it was time to take a step back and look at the bigger picture.

I am thankful for the guidance and training I received early in my time in the Lanzara group by more senior members. Chris Smallwood took the time to teach me the basics of ARPES, data analysis in Igor, and life in the lab. His generosity and expertise are perfectly encapsulated for me by a particularly trying night at the ALS, when he helped me to fix a transfer arm in the small hours of the morning. Wentao Zhang was always kindly willing and able to help with running experiments in our lab and fixing whatever was going on with the laser. I was fortunate to coincide with Tristan Miller through most of my time in the group, but am particularly grateful for his help in running and understanding time-resolved experiments early on.

Through my years in graduate school, I have had the immense pleasure working in of a group whose members go out of their way to help and support one another. Cassi Hunt was a pleasure to work alongside as we worked on building the THz experiment, always patient as I learned the technique and ever ready with relevant classic pop-culture references. Kenny Gotlieb was always incredibly generous with his time, cheer, expertise on his experiment, and his stash of late-night snacks. I deeply enjoyed our many conversations about physics, our pasts, and our futures. I am thankful that essentially my entire time in the Lanzara group coincided with that of Drew Latzke, with whom I had numerous adventures. Conferences, experiments, and after-work events were all greatly improved by his thoughtful presence. Ryo Mori was similarly a consistent friendly presence over the years whose passion regarding his work is infectious. I worked directly with Chiu-Yun Lin only rarely, but she was always a friendly face and enthusiastic in helping me understand the spin-resolved experiment. Jonathan Ma and I shared an office, several long nights during beamtime, and deeply impactful conversations about research and life.

The newer generation of group members have brought an exciting energy and variety of ideas to the group. Sam Ciocys has an eagerness to try new things and ability to fix the inevitable problems along the way without ever, seemingly, getting discouraged. Nick Dale and Conrad Stansbury likewise are pushing the group forward with new experimental techniques and technologies, and are both truly impressive in their simultaneous dedication to their research and to lending a helping hand when it's needed. I admire the ambition and enthusiasm of Kayla Currier, Prosper Dzanwa, Claudia Fatuzzo, and Danny Eilbott, who are attempting challenging experiments, many of which I would not have imagined.

The scientific content of this dissertation was also enabled by an excellent community of collaborators in Berkeley and beyond. Tom Hogan and Stephen Wilson provided the samples

for my experiments, as well as fruitful discussions of the data. Sung-Kwan Mo and Jonathan Denlinger provided essential support on their respective beamlines. Ashvin Vishwanath, Dung-Hai Lee, and Tanmoy Das provided theoretical insights into various aspects of these results.

I have also been fortunate to find a community far from home among my friends in Berkeley. In particular I'd like to note Jonathan, Michael, Justine, Greg, Emily, David, Will, and Alex for sharing a home and important parts of our lives. There are so many other people I am thankful to have met–I will always remember the board games, taco nights, bonfires, and intramural soccer games, and especially those with whom I shared them as essential parts of my life the past several years.

Finally and most fundamentally, I am thankful for the love and support of my family. My grandparents, Mimi and David, Janet and Don, have always been clear in their unconditional love and encouraged me to dream big. My brothers, Doug and Matt, provide constant reminders of the value of working hard for the things we care about and inspiration to do the same. My parents, Don and Katie, have given me everything I have ever needed to be successful, most importantly belief in myself and unfailing support through the most challenging parts of my life. I am who I am because of you, and for that I am overwhelmingly grateful.

Chapter 1

Introduction

The past several decades of research in condensed matter physics have been focused on materials falling into one of two categories: those in which the correlation of charge carriers via the Coulomb force are important, and those in which the relativistic interaction between an electron's spin and its orbital angular momentum is relevant. Recently, interest has been growing in materials where both Coulomb correlations and spin-orbit coupling are relevant to the ground state. This extends the separate domains of Mott insulators and topological materials to a rich landscape summarized in figure 1.1, which hosts a variety of exotic states.

The iridates, including the material that is the focus of this dissertation, lie in the relatively unexplored middle ground of this landscape with moderate strength of both spin-orbit coupling and Coulomb correlations. In many iridates, including Sr_2IrO_4 where it was first discovered[1], $Sr_3Ir_2O_7$ [2, 3], Na_2IrO_3[4, 5], and Li_2IrO_3[6] the parent state is the spin-orbit Mott insulator. Theoretical proposals for alternate ground states including spin liquids[7] and superconductors [8] have spurred efforts to look for these states in related materials. Here, we explore the properties of the spin-orbit Mott state in $(Sr_{1-x}La_x)_3Ir_2O_7$ after it has been perturbed by carrier doping.

This chapter explores the physics underpinning experimental studies in chapters 3 and 4. Section 1.1 briefly discusses concepts of band theory used later in this dissertations, with a sketch of the fundamentals of Mott insulators (section 1.1.1) and an overview of the role of spin-orbit coupling in solids (section 1.1.2). The spin-orbit Mott state exemplified by $(Sr_{1-x}La_x)_3Ir_2O_7$ and several other iridates is described in detail in section 1.2. The remainder of the chapter is devoted to experimental characterizations of $Sr_3Ir_2O_7$, $(Sr_{1-x}La_x)_3Ir_2O_7$, and variants of its relative Sr_2IrO_4.

1.1 Single-electron band physics

In order to get a handle on the problem of 10^{23} electrons interacting with 10^{23} ionic cores, a series of approximations must necessarily be made. First among these is the Born-Oppenheimer approximation, in which the physics of the ionic cores and electrons are treated separately–

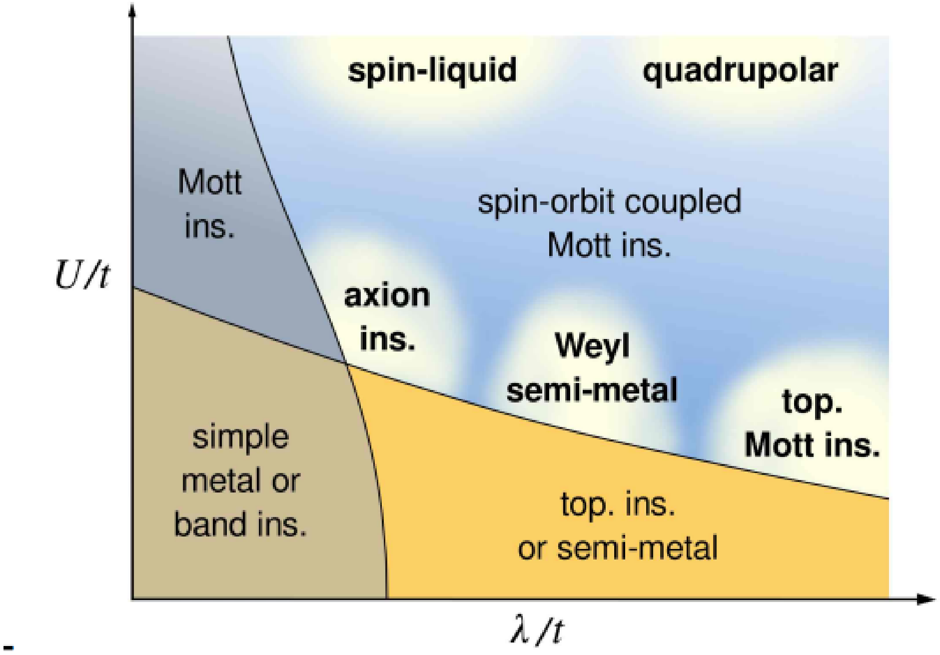

Figure 1.1: Phase diagram of ground states with spin-orbit coupling and Coulomb correlations, from [9]

when considering the state of the electrons, the ionic cores are considered as fixed sources of potential due to Coulomb interactions. Next, one brings in the (empirically supported) notion of a crystal, i.e. that these ionic cores form a periodic lattice, and the thermodynamic limit of an infinite crystal, allowing one to not worry about boundary conditions (though for surface and interface effects these can be explicitly addressed). In this world of an infinite periodic potential, Bloch's theorem is essential: the energy eigenstates for an electron in a periodic potential are of the form

$$\psi_{n\vec{k}}(\vec{r}) = e^{i\vec{k}\cdot\vec{r}}\phi_{n\vec{k}}(\vec{r}) \tag{1.1}$$

where $\phi_{\vec{k}}(\vec{r})$ has the same periodicity in $\vec{r}$ as the underlying potential and is labeled by the *crystal momentum* $\vec{k}$ (which differs from true momentum in that it is only defined up to a reciprocal lattice vector) and a band index n, as many states can exist with the same $\vec{k}$. The energy eigenvalues corresponding to these states $E_n(\vec{k})$ is known as the dispersion relation, and is a function of fundamental interest as it governs the behavior of electrons; derivatives of the dispersion give electron velocities and effective masses, and the availability of unoccupied electron states at small excitation energies defines the difference between metals and insulators.

This reduced problem is still in general quite difficult, but can be solved using a variety of approximations. Among the most useful builds the Bloch wavefunction perturbatively from the atomic wavefunctions at each site. This is known as the tight binding approximation (because it is most relevant when electron are tightly bound to their ionic cores), and is the basis for talking about orbital character of electron bands, as well as models for correlated system discussed later in section 1.1.1.

As an example of how this works, consider a 1D chain of atoms with one electron each, separated by a distance a. Electron wave functions must, by Bloch's theorem, be of the form $\psi_k(x) = e^{ikx}\phi_k(x)$, with $\phi_k(x)$ periodic over a length a. While the ϕ_k can in principle differ for inequivalent k, the most natural choice in a picture starting from the independent atomic picture is just a superposition of the atomic orbitals, so that

$$\psi_k(x) = \frac{1}{\sqrt{N}} e^{ikx} \sum_{j=0}^{N} \phi(\vec{r} - \vec{r_j}), \tag{1.2}$$

The energy of each ψ_k state is then given by evaluating the expectation of the full Hamiltonian in that state

$$\begin{aligned}
E(k) =& < \psi_k^* | H | \psi_k >= \int \psi_k^* H \psi_k && (1.3)\\
&= \frac{1}{N} \sum_j \sum_\ell e^{i(\ell - j)ka} \int \phi^*(\vec{r} - ja\hat{x}) H \phi(\vec{r} - \ell a\hat{x}) d\vec{r} && (1.4)\\
&= \frac{1}{N} \sum_j \sum_\ell e^{i(\ell - j)ka} \int \phi^*(\vec{u}) H \phi(\vec{u} - (\ell - j)a\hat{x}) d\vec{x} && (1.5)\\
&= \frac{1}{N} \sum_j \sum_m e^{imka} \int \phi^*(\vec{u}) H \phi(\vec{u} - ma\hat{x}) d\vec{u} && (1.6)\\
&= \sum_m e^{imka} \int \phi^*(\vec{u}) H \phi(\vec{u} - ma\hat{x}) && (1.7)
\end{aligned}$$

where this last sum can be broken down by the distance m between sites. Since the atomic orbitals ϕ is localized near the origin, the overlap integrals decrease rapidly with increasing $|m|$. Assuming it vanishes for $|m| > 1$ gives

$$\begin{aligned}
E(k) &= \int \phi^*(\vec{u}) H \phi(\vec{u}) + \cos(ka) \int \phi^*(\vec{u}) H \phi(\vec{u} - a\hat{x}) && (1.8)\\
&= E_0 + \gamma \cos(ka) && (1.9)
\end{aligned}$$

where E_0 is the energy of the free atomic orbital. While in principle the overlap integral γ is calculable, it is typically left as an experimental fitting parameter.

In a more complicated system there can be degenerate orbitals, orbitals of higher ℓ (so that they are not spherically symmetric), and atoms of multiple elements in the lattice. In the case of $Sr_3Ir_2O_7$, all three of these come into play–the relevant physics is the result of 5 electrons in each Ir $5d$ shell, and interaction between adjacent iridium sites is mediated by the filled $2p$ orbitals on the intermediate oxygen sites. This has implications for the magnetic interactions between moments on the Ir sites, which is discussed further in 1.2.2.

1.1.1 Coulomb correlations and the Hubbard model

The band theory outlined above explicitly ignores one of the fundamental properties of electrons–their negative charge, which gives rise to complicated interactions between the many electrons in the lattice. Band theory can be extended with the Fermi liquid theory first developed by Landau[10], which takes into account weak interactions between electrons. In this picture, electrons are replaced conceptually with electronic quasiparticles, collective excitations of the many-body electron wavefunction. These move through a metal in the same way as an electron in the simple band picture, but have a finite lifetime as interactions with other states give a nonzero probability of decay.

In many transition metal oxides, however, band theory predicts metallic behavior while experiment shows insulating behavior. In these systems (of which NiO was an early example), it was proposed by Mott and Peierls in 1937 that electron-electron interactions drive the insulating behavior[11]. This led eventually to the 1963 Hubbard model[12], whose Hamiltonian is written in second quantization as

$$\hat{H} = -t \sum_{<ij>,\sigma} \hat{c}^{\dagger}_{i,\sigma}\hat{c}_{j,\sigma} + \hat{c}^{\dagger}_{j,\sigma}\hat{c}_{1i,\sigma} + U \sum_{i} \hat{n}_{i,\uparrow}\hat{n}_{i,\downarrow} \tag{1.10}$$

where the first sum is over all nearest neighbor pairs i and j, $c_{i,\sigma}, c^{\dagger}_{i,sigma}$ are fermion annihilation and creation operators on site i with spin σ, respectively, and $n_{i,\sigma}$ is the number of electrons on site i with spin σ. The first term is commonly known as the hopping term and gives rise to the tight-binding band structure as in section 1.1. The second term is the Hubbard U term and causes an energy penalty for having a site doubly occupied as its mechanism for encoding electron-electron repulsion.

For Mott insulators, a common starting point in the Hubbard model is the case of half filling (one electron per site), and treating hopping as a perturbation on the localized ground state ($t << U$). Second order perturbation theory starting from this ground state gives rise to an antiferromagnetic interaction between neighboring spins, as hopping is forbidden for neighboring spins that are aligned (due to Pauli exclusion) while hopping lowers the energy for antiparallel spins.

It is empirically observed that most Mott insulators are antiferromagnets at sufficiently low temperature. This, however, gives rise to a second method for an insulating state to arise: in the case of a square lattice, the antiferromagnetic ground state partially breaks translational symmetry (as two neighboring sites with opposite spins are inequivalent) and thus doubles the size of the unit cell. This causes there to be an even number of electrons per unit cell, which is necessary but not sufficient for an insulating ground state in simple

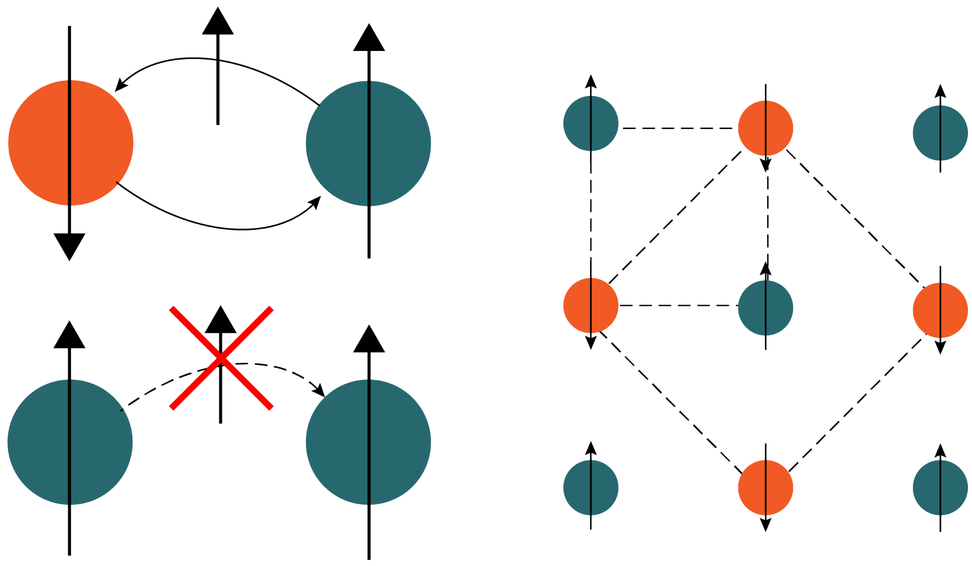

Figure 1.2: Antiferromagnetic order in Mott insulators

band theory. A metal which becomes insulating due to antiferromagnetic ordering is known as a Slater insulator, while in a Mott insulator the gap precedes the magnetic ordering.

1.1.2 Spin-orbit coupling

The above discussion of electronic physics in solids neglects the spin of an electron except as an additional degree of freedom that allows two electrons to have the same energy and momentum. Here we discuss the relativistic spin-orbit coupling, which changes the energy of electrons according to the relationship between their spin and orbital angular momenta. This is first discussed in the more well-known atomic case, followed by its immediate analog in semiconductors. The section ends with descriptions of several states that emerge in the presence of both spin-orbit coupling and broken symmetry.

Atomic spin-orbit coupling

The general Hamiltonian for a spin $m\vec{u}_s$ in a magnetic field $\vec{B}$ is given by

$$H = -\vec{\mu_s} \cdot \vec{B} \tag{1.11}$$

and serves to lower the electron energy if it is more nearly aligned with the magnetic field. An electron bound to an atomic nucleus does not ordinarily experience a magnetic field, but for a charged particle moving with velocity $\vec{v}$ in an electric field $\vec{E}$ there is an effective magnetic field given by

$$\vec{B} = -\frac{\vec{v}}{c^2} \times \vec{E} \tag{1.12}$$

which arises from a Lorentz transformation into the particle's rest frame. For the case of an electron bound to an atom, a spherically symmetric potential (and thus, electric field) is expected, so that one may write $\vec{E}(\vec{r}) = E(r)\vec{r}/r$. Substituting this form into equations 1.11 and 1.12 gives

$$\begin{aligned} H &= -\frac{E(r)}{rc^2}\vec{\mu_s}\cdot(\vec{v}\times\vec{r}) && (1.13)\\ &= \left(\frac{E(r)}{m_e rc^2}\right)\left(\frac{g_e\mu_B}{\hbar}\right)\vec{S}\cdot(\vec{r}\times\vec{p}) && (1.14)\\ &= \frac{2\mu_B}{\hbar m_e ec^2}\frac{1}{r}\frac{\partial U}{\partial r}\left(\vec{L}\cdot\vec{S}\right) && (1.15)\end{aligned}$$

So that the spin-orbit coupling favors states where $\vec{L}$ and $\vec{S}$ are antiparallel, i.e., the total angular momentum $\vec{J}$ is minimized. The potential U is given by the Coulomb potential for an atom with atomic number Z:

$$U(r) = -\frac{1}{4\pi\varepsilon_0}\frac{Ze}{r} \tag{1.16}$$

so that

$$\frac{\partial U}{\partial r} = \frac{1}{4\pi\varepsilon_0}\frac{Ze}{r^2} \tag{1.17}$$

and

$$H \propto \frac{Z}{r^3}\left(\vec{L}\cdot\vec{S}\right) \tag{1.18}$$

The expectation of the radius for a hydrogen-like atom is $r = a_0/Z$, and the magnitude of the spin-orbit coupling in hydrogen-like atoms is proportional to Z^4. Note that a more exact treatment takes into account that the electron's orbital frame is not inertial, which gives rise to a factor of $\frac{1}{2}$ in the final result, but all the scaling dependencies are encapsulated in this treatment.

It is for this reason that systems with heavier elements (e.g., iridium) are those where spin-orbit coupling is relevant, despite the screening by other electrons that necessarily occurs in most real systems. This is borne out by figure 1.3. In the left panel is a schematic for a common band structure near the Fermi level for GaAs and other semiconductors, with an energy splitting Δ_{SO} between the light and heavy hole valence bands and a deeper split-off band. The value of this splitting for a range of semiconductors is plotted in the right panel (data from [13] and [14]) vs the atomic number of the heaviest component element. There is an overall upward trend, though a wide spread in spin-orbit splitting values.

Symmetry considerations

In prior discussions of the effects of spin-orbit coupling, both inversion and time-reversal symmetries were preserved. This guarantees spin degeneracy as these spatial symmetries

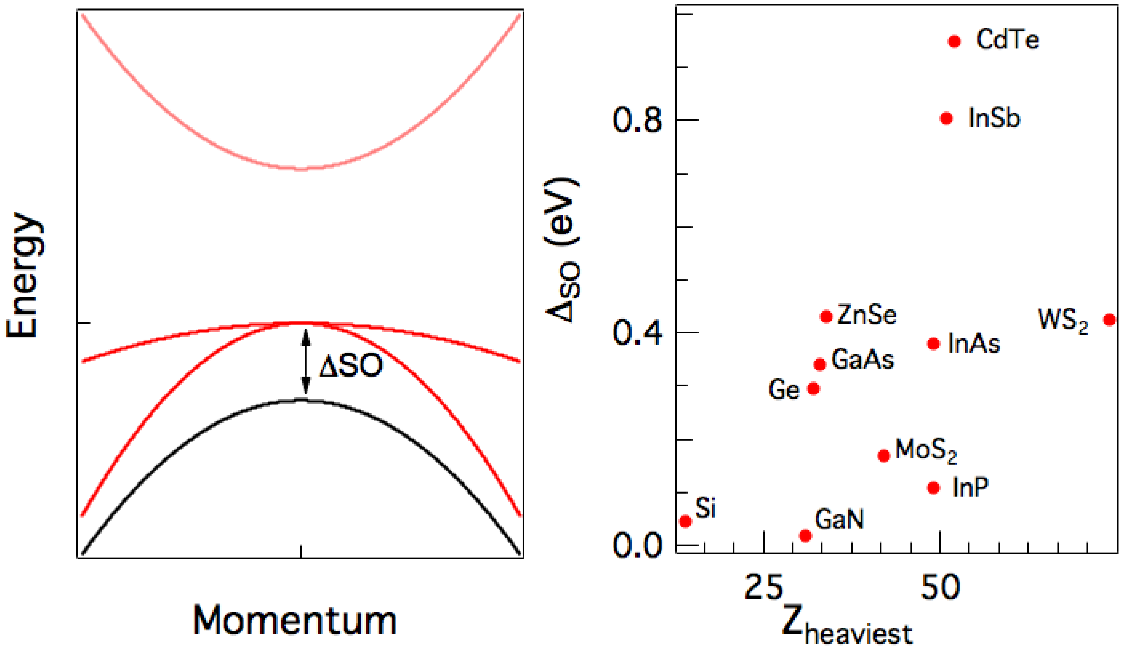

Figure 1.3: Spin-orbit coupling in semiconductors. Left: schematic of typical near-E_F band structure with spin-orbit split-off band. Right: Band splitting due to spin-orbit coupling vs. the atomic number of heaviest constituent element for several common semiconductors

manifest in symmetries of the allowed energy states:

$$E(\vec{k},\uparrow) = E(-\vec{k},\uparrow) \text{ (inversion)} \tag{1.19}$$

$$E(\vec{k},\uparrow) = E(-\vec{k},\downarrow) \text{ (time reversal)} \tag{1.20}$$

$$E(\vec{k},\uparrow) = E(\vec{k},\downarrow) \text{ (inversion and time reversal)} \tag{1.21}$$

Thus, in order to have states with spin non-degenerate bands, either time-reversal or inversion symmetry must be broken. The latter case is the domain of magnetism, where states of spin along a particular direction are lowered in energy relative to those antiparallel. The rest of this section will explore system with broken inversion symmetry and its effects on the electronic ground state.

Rashba effect

One common way for inversion symmetry to be broken is at the interface between a sample and the vacuum, i.e. its surface. At such a boundary, the charges of the ions nearest the surface are not counterbalanced by their partners above and an electric field arises. As in

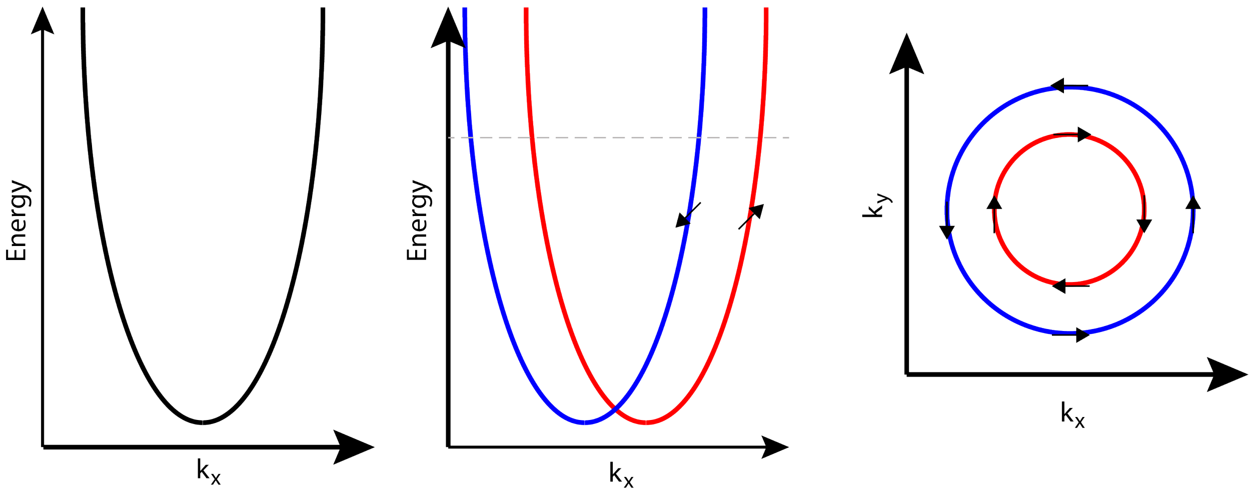

Figure 1.4: Schematic of the Rashba effect

the case of atomic spin-orbit coupling, electrons moving in this electric field see an effective magnetic field

$$\vec{B} = -\frac{1}{c^2}\left(\vec{v} \times \vec{E}\right) = \frac{1}{mc^2}\left(\vec{p} \times \vec{E}\right) \tag{1.22}$$

which will then interact with the spin of the electron via the Hamiltonian in equation 1.11. Ignoring the possible addition of a reciprocal lattice vector, $\vec{p} = \hbar\vec{k}$ and substituting $\vec{E} = E_0\hat{z}$ gives

$$H_{\text{Rashba}} = \alpha\left(\vec{\sigma} \times \vec{k}\right) \cdot \hat{z} \tag{1.23}$$

which clearly induces a splitting between spins aligned along the positive and negative z-axis. Restricted to $\vec{k} = k_x\hat{x}$ and considering separately the Hamiltonians for "up" and "down" spins with respect to the z-axis, this is a splitting proportional to k_x.

A schematic of the effect of the Rashba effect on a free electron band (applicable to, for instance, the (111) surface state on gold) is shown in figure 1.1.2. At left is the unperturbed spin-degenerate dispersion along the k_x direction which, as the Rashba effect is turned on, splits into two bands based on the spin in the perpendicular direction in the center panel. When viewed from the perspective of a constant energy slice in the k_x, k_y plane, there are two spin-polarized bands with counter-rotating helical spins, as shown in the right panel.

Dresselhaus effect

While inversion symmetry is always broken at material boundaries, in many materials the underlying crystal structure lacks inversion symmetry to begin with. These so-called noncentrosymmetric crystals include common III-V semiconductors with the "zincblende" structure, including GaAs. With this structure, there is a spin-momentum interaction which, up

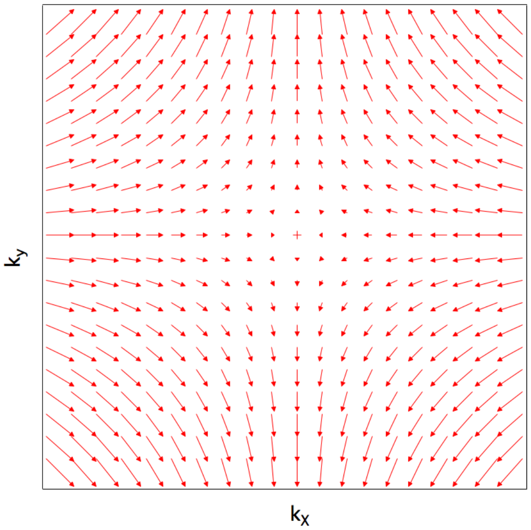

Figure 1.5: Effective magnetic field for the linear Dresselhaus effect

to prefactors is given by

$$H_D \propto k_x \left(k_y^2 - k_z^2\right) \sigma_x + k_y \left(k_z^2 - k_x^2\right) \sigma_y + k_z \left(k_x^2 - k_y^2\right) \sigma_z \tag{1.24}$$

In many thin or quasi-2D systems, k_z is not a meaningful momentum and should be averaged over. In these cases, there is a cubic term (in k_x, k_y) that comes from the parts of the above with no k_z dependence, and a linear term from the parts proportional to k_z^2, which is

$$H_{\text{D, linear}} \propto -k_x \sigma_x + k_y \sigma_y \tag{1.25}$$

The effective magnetic field with respect to crystal momentum (i.e., the direction in which it is energetically favorable for the spins to point) for this linear Dresselhaus effect is shown in figure 1.5. Note that, as expected, this arrangement does not respect inversion symmetry, but still respects time reversal as the field flips with opposite $\vec{k}$.

Local inversion symmetry breaking

It has recently been discovered that, even in materials with an inversion center, local effects can give rise to spatially dependent spin structures in momentum space[15]. Because spin-orbit coupling is due to an interaction between valence electrons and heavy ionic cores, the symmetry at these sites is also relevant. If an ion does not sit at an inversion center of its crystal structure, electrons that are localized there can experience local electric fields.

As an example, consider the two-dimensional crystal structure illustrated in figure 1.6 which consists of layers of two types of atoms. The overall structure is defined by a rectangular lattice and has inversion symmetry centered at the two locations marked with stars,

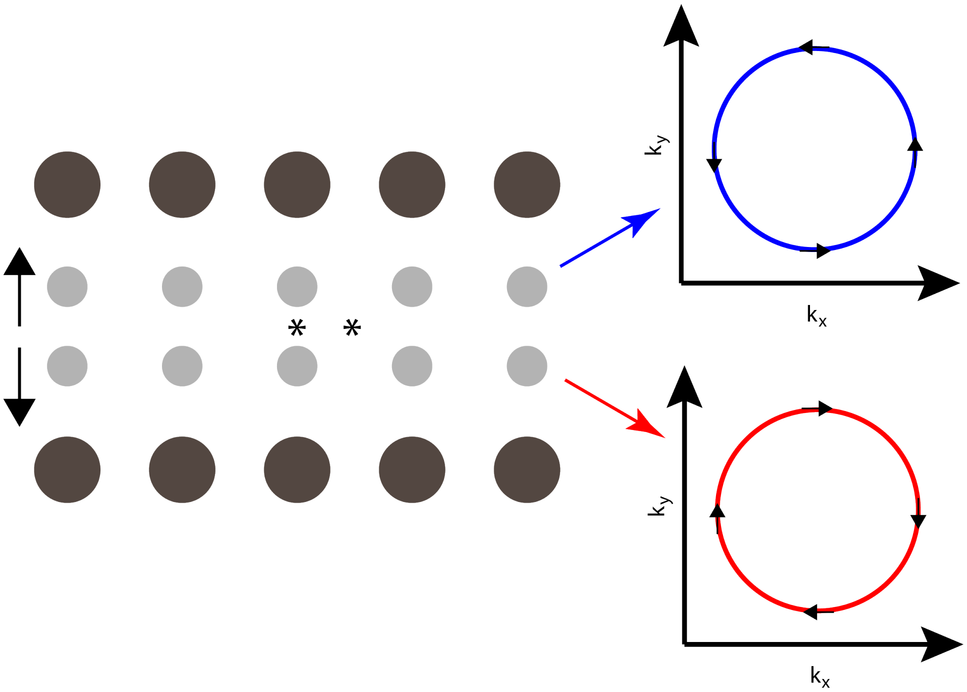

Figure 1.6: Local Rashba effect in a layered material

and thus for the overall system (assuming also time reversal symmetry) opposite spin states must be degenerate. Limiting the scope to the electrostatic environment on one of the light gray sites, however, reveals a lack of inversion symmetry as a dark ion sits on one side of it, a light ion the other. The charges on these sites can be different due to different oxidation states in the bonding process, so that a net dipole field can exist. This electric field, similar to that at an interface, can give rise to a Rashba-like effect where the spin of electrons in a given layer is locked to its momentum. This is offset by the opposite dipole field, and thus a spin texture of the opposite chirality, in the adjacent layer, and the total spin polarization is zero.

This sort of spin polarization is in practice difficult to measure, as any bulk probe will see offsetting signatures from the two layers. It has, however, been observed using angle-resolved photoemission spectroscopy (discussed in chapter 2) in $PtSe_2$[16] and WSe_2, as this selectively probes the surface of a material, allowing for stronger signal from the spin chirality in the top layer than in the one beneath it.

1.2 Ruddlesden-Popper Iridates: Sr_2IrO_4 and $Sr_3Ir_2O_7$

This section will discuss the physics of the Ruddlesden-Popper iridates–a family of materials $Sr_{2n}Ir_nO_{3n+1}$ that share the same layered structure of Ir-O octahedra. The structure of the n=1 compound, Sr_2IrO_4, is shown at left in figure 1.7 and is essentially the same as that

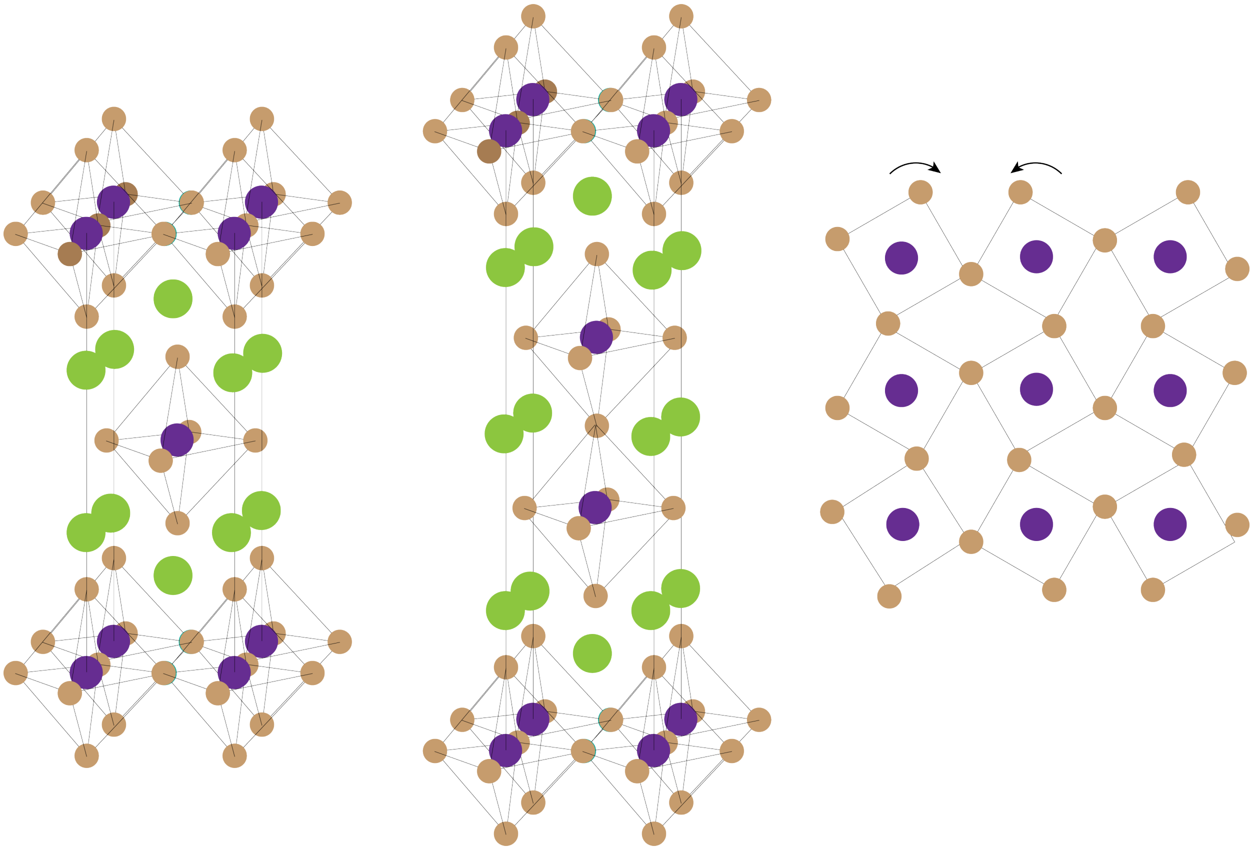

Figure 1.7: Crystal structure of Ruddlesden-Popper iridates. Left: 3D view of basic structure in Sr_2IrO_4 Center: 3D view of basic structure in $Sr_3Ir_2O_7$. Right: Structure in the Ir-O plane showing staggered octahedral rotations. Purple circles are Ir sites, brown O, and green Sr.

of La_2CuO_4, with iridium in the place of copper and strontium in that of lanthanum. The n=2 compound, $Sr_3Ir_2O_7$, and its doped relatives $(Sr_{1-x}La_x)_3Ir_2O_7$, are the subject of the experimental work discussed in this dissertation. Both Sr_2IrO_4 and $Sr_3Ir_2O_7$ deviate from the ideal layered perovskite structure in that the Ir-O octahedra rotate, alternating in clockwise and counterclockwise directions. This doubles the size of the true unit cell in the system (as it must contain octahedra of both rotations) and leads to a slight change in the magnetic interactions discussed in the following sections. More recent measurements have suggested a somewhat lower symmetry than that implied here[17, 18], though deviations are small.

1.2.1 Formation of the spin-orbit Mott state

From the chemistry of the parent compound $Sr_3Ir_2O_7$ and given the strong oxidation states of Sr (2+) and O (2-), charge neutrality demands that Ir is in a 4+ state with an electron configuration $[Xe]4f^{14}5d^5$. The $4f$ levels are deeper in energy and thus the near-E_F features will be due to the $5d$ orbitals in a tight binding picture. These d orbitals are labeled based on the angular part of their wavefunctions as $|xy>$,$|xz>$,$|yz>$,$|z^2>$, and $|x^2-y^2>$. The latter two (known as e_g orbitals) have high occupation probability along the directions of the Ir-O bonds, and due to the negative charge of the O site are energetically more costly to occupy. The former three orbitals (known as t_{2g}) have maxima in directions between these bonds and thus do not pay this energy penalty. The energy between these two sets of orbitals is known as the crystal field splitting, and at 3.6 eV[19], are the largest energy scale relevant to these d orbitals. Thus, the unoccupied e_g orbitals are ignored in the following discussion.

In this restricted framework of the t_{2g} orbitals, the spin-orbit coupling due to the iridium ions can be considered. As in the semiconductor case above, this will give a splitting $\Delta_{SO} \propto \vec{\ell}\cdot\vec{s}$ and thus the eigenstates of the angular momentum operators $\vec{\ell}$ should be considered. In terms of the eigenstates of the ℓ_z operator, the orbitals are

$$\begin{aligned}
|xy> &= \frac{1}{\sqrt{2}}(|+2> - |-2>) \\
|xz> &= \frac{1}{\sqrt{2}}(|+1> - |-1>) \\
|yz> &= \frac{i}{\sqrt{2}}(|+1> + |-1>) \\
|z^2> &= |0> \\
|x^2-y^2> &= \frac{i}{\sqrt{2}}(|+2> + |-2>)
\end{aligned}$$

Considering only the t_{2g} orbitals, the only nonzero elements of the ℓ_z operator are $<xz|\ell_z|yz>= i$ and its conjugate. The t_{2g} states can then be grouped into states with ℓ_z eigenvalues of +1, 0, and -1, so that they have an effective $|\vec{\ell}_{eff}| = 1$ and the spin-orbit coupling drives a splitting between a pair of $j_{eff} = \frac{3}{2}$ states and a $j_{eff} = \frac{1}{2}$ state. The latter are lower in energy and thus filled with four electrons, leaving only one electron in the $j_{eff} = \frac{1}{2}$ state. This state is then analogous to the half-filled Hubbard model, and the moderate U corresponding to this system is sufficient to split off a lower and upper Hubbard band and the sample is insulating.

1.2.2 Theory of Magnetism in $\mathbf{j_{eff}}$ states

The Hamiltonian governing the behavior of the spin and orbital degrees of freedom on a single site is taken to be:

$$H_0 = \lambda\vec{\ell}\cdot\vec{s} + \Delta\ell_z^2 \tag{1.26}$$

where the λ term is the usual spin-orbit coupling and the Δ term is related to the tetragonal distortion of the oxygen octahedra along the c-axis. This Hamiltonian has a degenerate

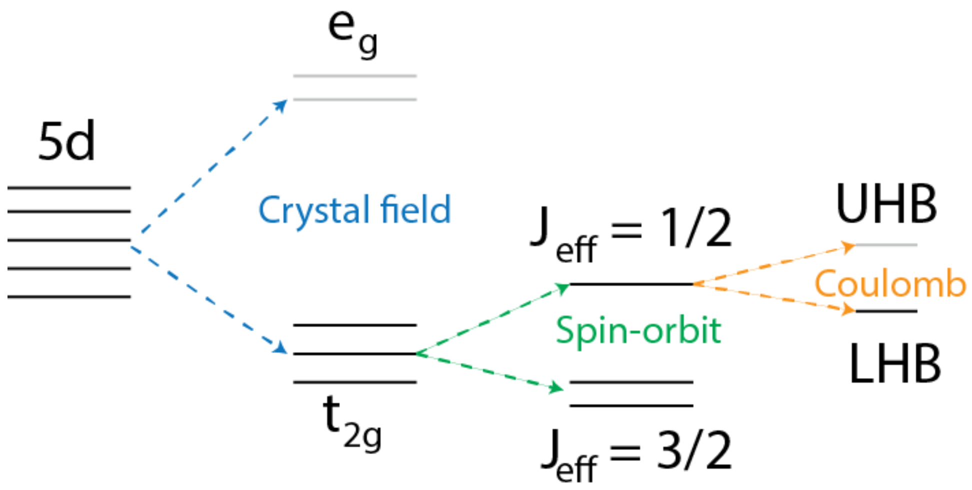

Figure 1.8: Schematic of energy scales in a spin-orbit Mott insulator

ground state given by spin-orbit entangled pseudospins:

$$|\tilde{\uparrow}> = \sin\theta|0,\uparrow> - \cos\theta|1,\downarrow> \quad (1.27)$$

$$|\tilde{\downarrow}> = \sin\theta|0,\downarrow> + \cos\theta|1,\uparrow> \quad (1.28)$$

with θ defined by $\tan(2\theta) = 2/\sqrt{(}2)\lambda/(\lambda - 2\Delta)$. In the limit of no tetragonal distortion these states are just the typical $\vec{j}$ states.

The magnetism of these pseudospin states on the Ir sites is governed by a Hamiltonian related to superexchange across intermediate oxygen atoms and depend significantly on the position of these oxygen atoms. Most physical systems can be approximated by geometries in which the Ir-O-Ir bond angle is 180° (corner-sharing octahedra, notably Sr_2IrO_4) or 90° (edge-sharing octahedra, notably Li_2IrO_3 and Na_2IrO_3). This dependency is due to the overlap integrals involved in superexchange and the coupling between the different Ir d orbitals and the spin degree of freedom, as shown in figure 1.9. In the corner-sharing case, the only non-vanishing orbital overlaps come from the $|xz>$ and $|xz>$ Ir states with the p_y (for the bond along the x direction) and p_z O states, respectively. Other states can be seen as zero on symmetry grounds: the product of the Ir state and the O state must be symmetric with respect to the y and z axes, while the symmetry along x is already broken by the displacement between the Ir and O ions. In the edge sharing case it is different orbitals on each Ir site that comes into play, with contributions from a $|yz>$ state on one Ir site and a $|xz>$ state on the other as well as the O p_z state.

For the corner-sharing case relevant to the material studied in this work, the resulting pseudospin interaction Hamiltonian is

$$H_{ij} = J_1\vec{S_i}\cdot\vec{S_j} + J_2\left(\vec{S_1}\cdot\vec{r_{ij}}\right)\left(\vec{r_{ij}}\cdot\vec{S_j}\right) \quad (1.29)$$

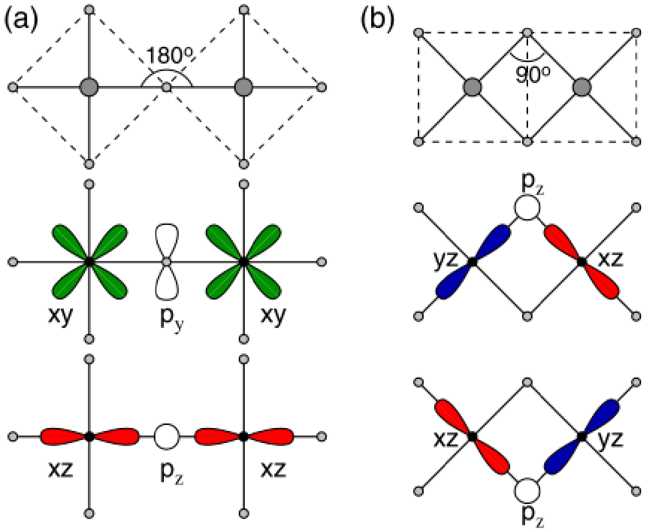

Figure 1.9: Geometries considered for superexchange in iridate systems, from [20]

where the $\vec{S_i}$ refer to the pseudospin states, $\vec{r_{ij}}$ is the unit vector along the bond between sites i and j, and J_1, J_2 are coupling constants, with J_2 a small perturbation on the otherwise isotropic antiferromagnetic Heisenberg model. Thus, up to small corrections, the interaction between spin-orbit entangled pseudospins in corner-sharing iridates is the same as in the widely-used t-J model for cuprates.

Further corrections added to the prior argument due to the rotation and elongation of Ir-O octahedra break the symmetry of the Heisenberg model, and the ground state can thus either have pseudospins aligned antiferromagnetically in the Ir-O plane (observed in Sr_2IrO_4) or along the perpendicular c axis (observed in $Sr_3Ir_2O_7$).

In the alternate case of edge sharing octahedra, the magnetic Hamiltonian reduces to a quantum compass model and has been proposed as a realization of the Kitaev model[20], which should give rise to a quantum spin liquid with fractional excitations[21, 22, 23]. Systems with this structure have been widely explored, including Na_2IrO_3[24, 25, 5, 26, 27, 28, 29, 30] and Li_2IrO_3[6, 31].

1.2.3 Layer-dependent metal-insulator transition

The prior discussion restricted its attention to a single Ir-O layer, approximating three-dimensional crystals as a two-dimensional system. From the structures in figure 1.7, we see that the Ir-O layers are more separated in the case of Sr_2IrO_4 than in $Sr_3Ir_2O_7$, and thus this system is more nearly two-dimensional. X-ray scattering shows that in this two-dimensional sample the $\mathrm{j_{eff}} = \frac{1}{2}$ picture very nearly holds [19], while $Sr_3Ir_2O_7$ is farther from this ideal picture [32]

Among the first measurements exploring the role of dimensionality in these systems was an optical conductivity measurement conducted on Sr_2IrO_4, $Sr_3Ir_2O_7$, and the fully three-dimensional $n = \infty$ compound, $SrIrO_3$. Since the latter is not easily grown in single bulk crystals, an epitaxially grown (on MgO) film was used. The results of this measurement are shown in figure 1.10. Panel (a) of this figure shows the optical conductivity spectrum for Sr_2IrO_4. In line with its insulating nature, the conductivity vanishes near zero energy, and exhibits two main peaks in the energy range measured, labeled α and β. These peaks are due to transitions into the unoccupied upper Hubbard band from the lower Hubbard band and $j_{\text{eff}} = \frac{3}{2}$ band, respectively, as illustrated in the cartoon of panel (d). In the spectrum for $Sr_3Ir_2O_7$ shown in panel (b), these two peaks have both broadened and shifted to lower energy. Finally, in the $SrIrO_3$ spectrum shown in panel (c), the α peak has reached zero energy, indicating a transition to a metallic state. The β peak in this spectrum has broadened further and shifted to slightly lower energy when compared to the $Sr_3Ir_2O_7$ measurement. This phenomenology is consistent with what one might expect from a tight binding picture for these samples. As the number of Ir-O layers grows, the average number of nearest neighbors for a given Ir atom increases from 4 in the most two-dimensional case (Sr_2IrO_4) to six in the cubic three-dimensional case ($SrIrO_3$). This increase in coordination number will increase the bandwidth until finally it is sufficiently great to bridge the separation caused by the Mott gap, as illustrated by the dashed lines in panel (d). At this point, the Hubbard bands merge and a partially-filled $j_{\text{eff}} = \frac{1}{2}$ band crosses the chemical potential. This allows for arbitrarily small excitations and the system is metallic, provided that the spin-orbit coupling is sufficiently strong to maintain separation between the $j_{\text{eff}} = \frac{1}{2}$ and $j_{\text{eff}} = \frac{3}{2}$ bands [33]. While this appears to hold experimentally, there is also a theoretical suggestion that the metallic state in $SrIrO_3$ is related to topology [34], similar to a proposal in Na_2IrO_3[30].

A similar argument suggests that by applying hydrostatic pressure will decrease the distance between neighboring Ir sites, increasing the overlap integrals and thus the bandwidth. Early experimental efforts in this direction found insulating behavior up to at least 55 GPa in Sr_2IrO_4 [35]. In $Sr_3Ir_2O_7$, a second-order structural transition is observed near 14 GPa [36], with a decreasing electronic gap up to 104 GPa [35]. A later study shows a first-order structural transition at 54 GPa and metallic behavior starting near 20 GPa [37].

1.2.4 Pseudogaps and possible superconductivity in Sr_2IrO_4

The experiment that shows the clearest connection to the particular physics of the cuprates started with an undoped parent Sr_2IrO_4 sample, which is then doped via the surface deposition of potassium ions. Since potassium is an alkali metal, it has a strong 1+ oxidation state and donates electrons to the surface layers of Sr_2IrO_4. The resulting spectral weight at the chemical potential for a deposition of half a potassium monolayer is shown at left in figure 1.11, and is remarkably similar to that seen in cuprates. Namely, there is a finite arc of ungapped states (positions marked with x's 1-4) as shown by the symmetrized EDCs at right. This analysis technique will be discussed in the next chapter, but the local minima in the spectral intensity at E_F correspond to the pseudogap. Similarly, surface potassium

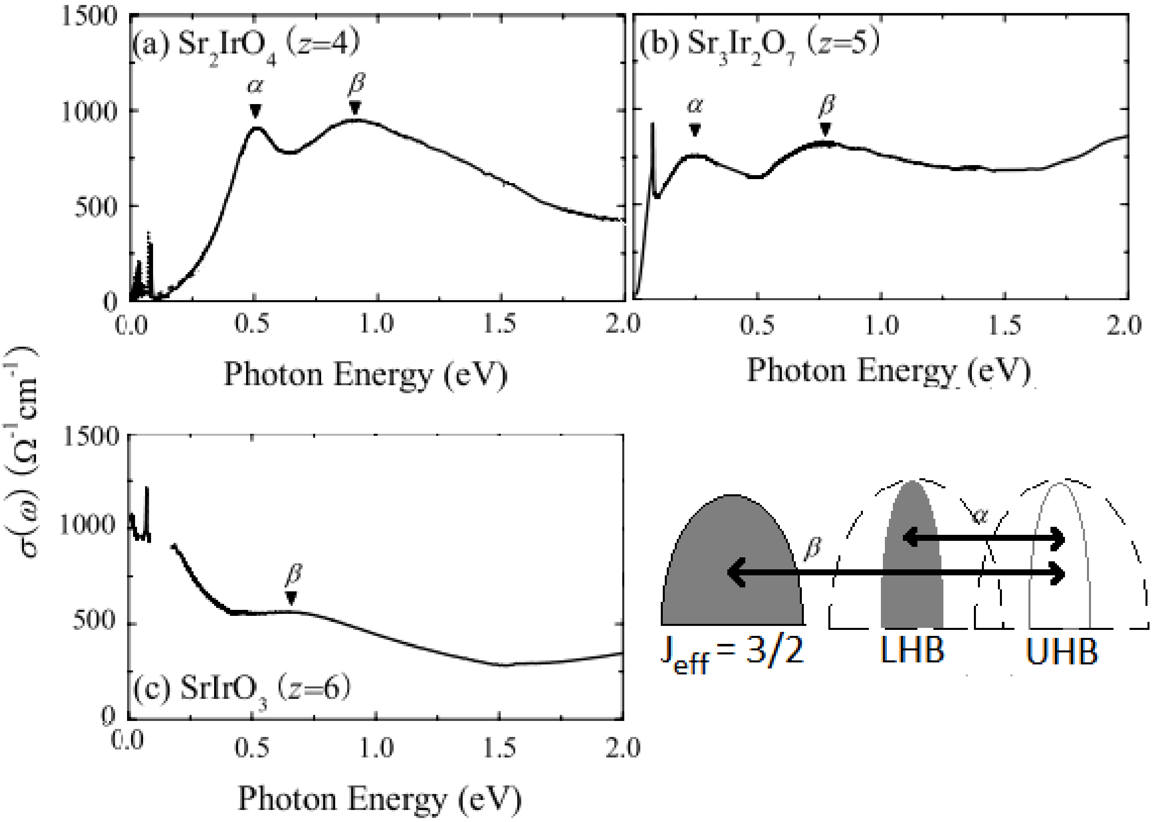

Figure 1.10: Layer-dependent metal-insulator transition in RP iridates. (a), (b): Optical conductivity for single crystal Sr_2IrO_4 and $Sr_3Ir_2O_7$, respectively. (c): Optical conductivity for thin-film $SrIrO_3$. (d): Schematic of low-energy features in the optical conductivity.

doping on a $Sr_2IrO_4/Sr_3Ir_2O_7$ heterostructure sample appears to give rise to a d-wave gap in analogy to the superconducting gap in cuprates that would point to a T_c near 30 K[38, 39].

While the ARPES data suggest superconductivity in Sr_2IrO_4 the nature of the surface doping experiment, which dopes only the first few layers and must be conducted in ultra-high vacuum, make traditional measures of superconductivity (i.e., magnetic susceptibility and electrical transport) difficult. Further, this sort of state is not observed in other measurements on chemically electron-doped samples[40, 41], pointing to a either a role of the potassium layer beyond chemical doping or to disorder induced by chemical doping decreasing the tendency toward superconductivity and the pseudogap state. There are, however, indications of a pseudogap in hole-doped Sr_2IrO_4 [42], though the doping on the Ir site makes interpretation more difficult.

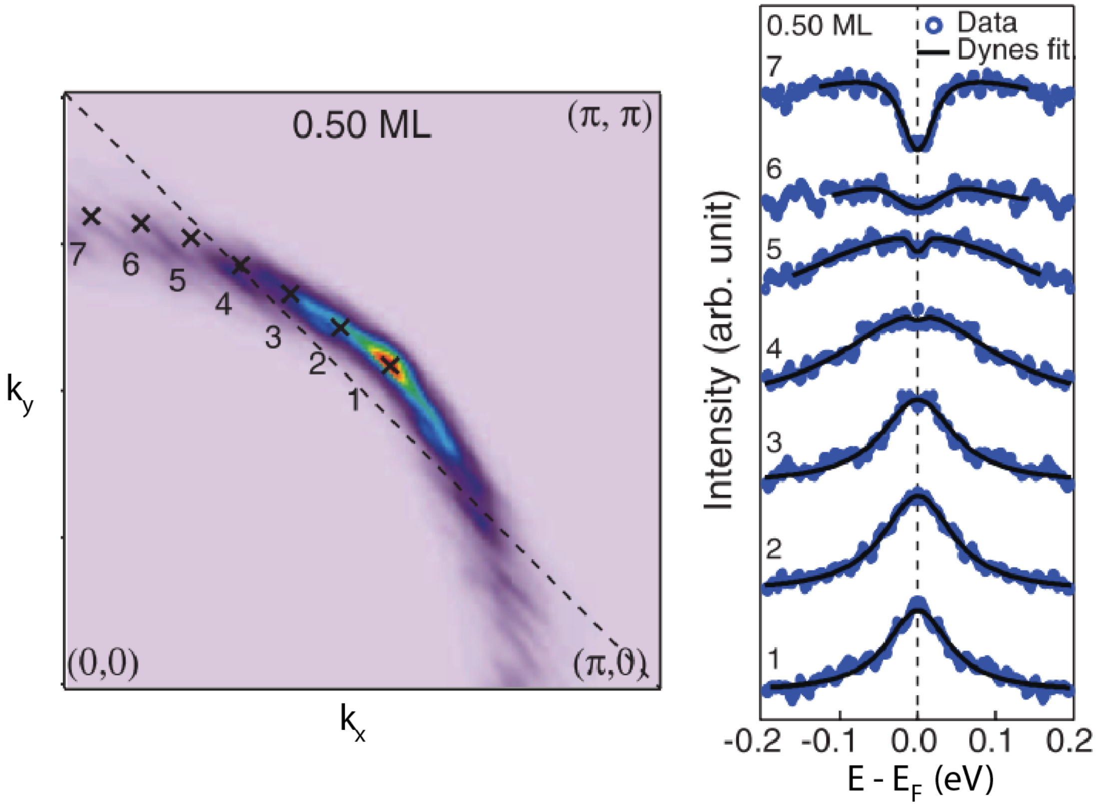

Figure 1.11: ARPES data revealing a pseudogap in Sr_2IrO_4

1.3 Properties of doped $(Sr_{1-x}La_x)_3Ir_2O_7$

While surface-doped Sr_2IrO_4 has similarities to the cuprate superconductors upon doping, as discussed in the previous section, there are many other systems in which carrier doping Sr_2IrO_4 induces a metal-insulator transition through the breakdown of the Mott state [43, 44, 45, 46, 47]. $Sr_3Ir_2O_7$ differs from its single-layer relative in magnetic and electrical ground states, and exhibits different phenomena with La substitution for Sr. This section will explore the ways in which $Sr_3Ir_2O_7$ evolves with doping, as measured by transport, magnetization, scattering, and optical experiments.

1.3.1 Transport properties

One of the first effects to consider upon doping an insulator is the ability to create a conductive system. In the case of a band insulator, this simply means occupying a previously empty conduction band that has a continuum of states available, so that even a very small number additional electrons should induce some metallic behavior. In a Mott insulator such as $Sr_3Ir_2O_7$, the picture is less clear. The addition of electrons to a half-filled insulating Mott

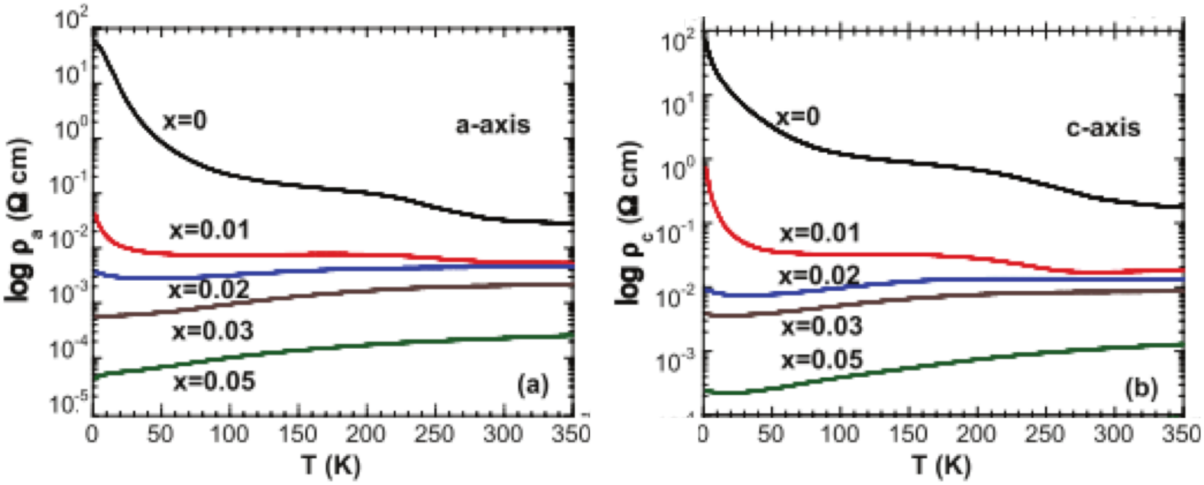

Figure 1.12: Resistivity measurements along both the a (left) and c (right) axis of $(Sr_{1-x}La_x)_3Ir_2O_7$ for several doping levels.

state will eventually diminish the energy barrier to hopping.

The most straightforward way to assess this transition is the measurement of electrical resistivity as a function of doping and temperature. This was done in [48] for a range of $(Sr_{1-x}La_x)_3Ir_2O_7$ samples from the parent compound to x = 0.05. These results are shown in figure 1.12. At left is the resistivity along the crystallographic *a*-axis, with the *c*-axis resistivity on the right. The quasi-two-dimensional nature of $(Sr_{1-x}La_x)_3Ir_2O_7$ is seen in the anisotropy between the resistivity in these two directions–resistivity along the *c* axis is roughly a factor of 10 greater than that along the *a* axis in samples with nonzero doping. In both cases the resistivity at all temperatures steadily drops with increasing doping, as additional carriers create a path for transport. The sign of a complete transition to a metal from an insulator is decreasing resistance as the temperature goes toward 0 K. This is achieved in the x = 0.05 sample but not the x = 0.03 sample, indicating an insulator-to-metal transition near x = 0.04.

1.3.2 Magnetic structure and excitations

Magnetic ground state

Earlier in this chapter, it was shown that the pseudospin Hamiltonian for Sr_2IrO_4 and, presumably, also $Sr_3Ir_2O_7$, was that of a Heisenberg antiferromagnet within a single Ir-O plane. Neither the direction of the spins nor the relationship between spins of neighboring Ir-O layers is obvious from this Hamiltonian. Empirically, in $Sr_3Ir_2O_7$, the spins point along the crystallographic *c* axis[49, 50]. Further, spins along the *c* axis are anti-aligned, as shown in the right side of figure 1.13 from [51]. This structure leads to the same periodicity of the

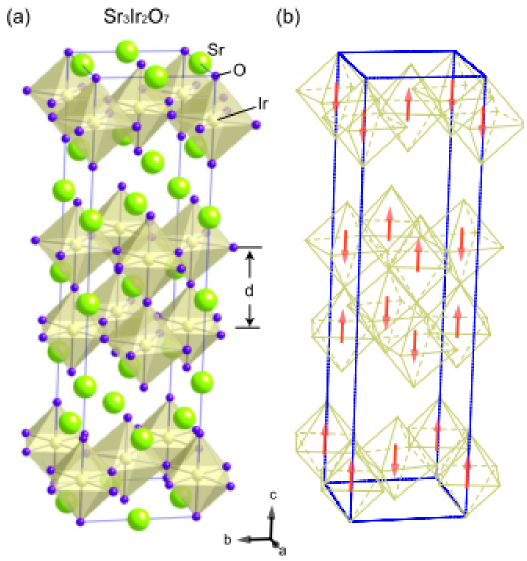

Figure 1.13: Crystallographic and magnetic structure of $Sr_3Ir_2O_7$ from [51].

Ir-O octahedral rotations discussed in section 1.2 and thus does not break any additional symmetries or change the unit cell with the onset of antiferromagnetic order.

This antiferromagnetic ground state is one of the clearest empirical differences between $Sr_3Ir_2O_7$ and Sr_2IrO_4, where the spins align antiferromagnetically within the ab plane, along the direction of the Ir-O bonds[52]. The susceptibility measurements in the literature ([48]) show significant ability for the spins to tilt away from the c-axis with small magnetic fields and thus that the magnetic anisotropy is relatively small. This in turn suggests that the c axis ground state is near in energy to one with spins aligned in the ab plane as in the case of Sr_2IrO_4. Indeed, a theoretical study [51] found that these states are near in energy, with the transition between these two states governed by the compression or elongation of the Ir-O octahedra along the c axis. This result is illustrated in figure 1.14 in the form of a phase diagram for undoped $Sr_3Ir_2O_7$ and Sr_2IrO_4 with respect to this distortion (parameterized by θ) and the strength of the Hund's coupling in the system. The solid line shows the phase boundary between a canted in-plane AF order and the c-axis collinear order actually observed in $Sr_3Ir_2O_7$. The dashed vertical line represents the same for Sr_2IrO_4, which differs from that for $Sr_3Ir_2O_7$ due to additional interlayer interaction terms in $Sr_3Ir_2O_7$. The shaded region represents the experimentally constrained parameter space that may be occupied by $Sr_3Ir_2O_7$. This so-called "spin flop" is observed experimentally in Sr_2IrO_4 upon doping with either Ru[53] or Mn [54]. Other theoretical studies also suggests that a transition to the in-plane magnetic configuration may be driven by oxygen vacancies [55], and that the Hubbard model derived for the bilayer system in analogy to the calculation for Sr_2IrO_4 naturally results in c-axis order [56].

The evolution of the magnetic state with doping in $(Sr_{1-x}La_x)_3Ir_2O_7$ was measured using

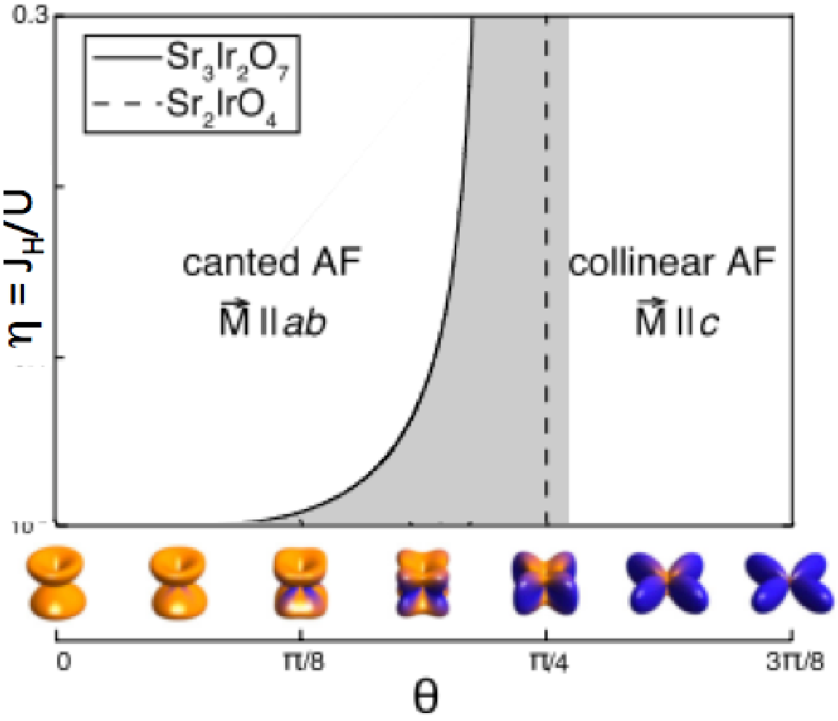

Figure 1.14: Spin flop transition in $(Sr_{1-x}La_x)_3Ir_2O_7$ and Sr_2IrO_4 as a function of octahedral distortion and Hund's coupling.

polarized neutron scattering in [57], and is summarized in figure 1.15. The panel at left shows the evolution of the magnetic ordering between samples with x ≈ 2% and x ≈ 3%. In both samples, the order parameter is zero above an onset temperature near 250 K, then increases monotonically toward a saturation value at low temperature. While the difference between these samples in La concentration is only 1%, the x ≈ 3% sample shows a significant suppression of the ordered moment. Adding data from measurements at x = 0, x ≈ 4% gives the curve in the panel on the right. This evolution of the magnetic order parameter with doping points to a phase transition near x = 4%.

Combining this magnetic phase boundary with the transport results in figure 1.12 and several other measurements gives rise to the phase diagram for $(Sr_{1-x}La_x)_3Ir_2O_7$ in figure 1.16. At the lowest doping levels and temperatures, the system is both antiferromagnetic and insulating, as expected for a Mott insulator. With increasing doping both the insulating and antiferromagnetic behaviors weaken, and vanish near the critical doping x ≈ 4%. Beyond this doping level, there is no long-range magnetic ordering, though later works reveal signatures of short-range magnetic correlations. Hogan et al make the point in [57] that this doping-driven phase transition is, in fact, first order, with the most compelling evidence being scanning tunneling microscopy measurements of samples in the region just to the left of the critical doping in this phase diagram. These measurements reveal phase separation, i.e., isolated

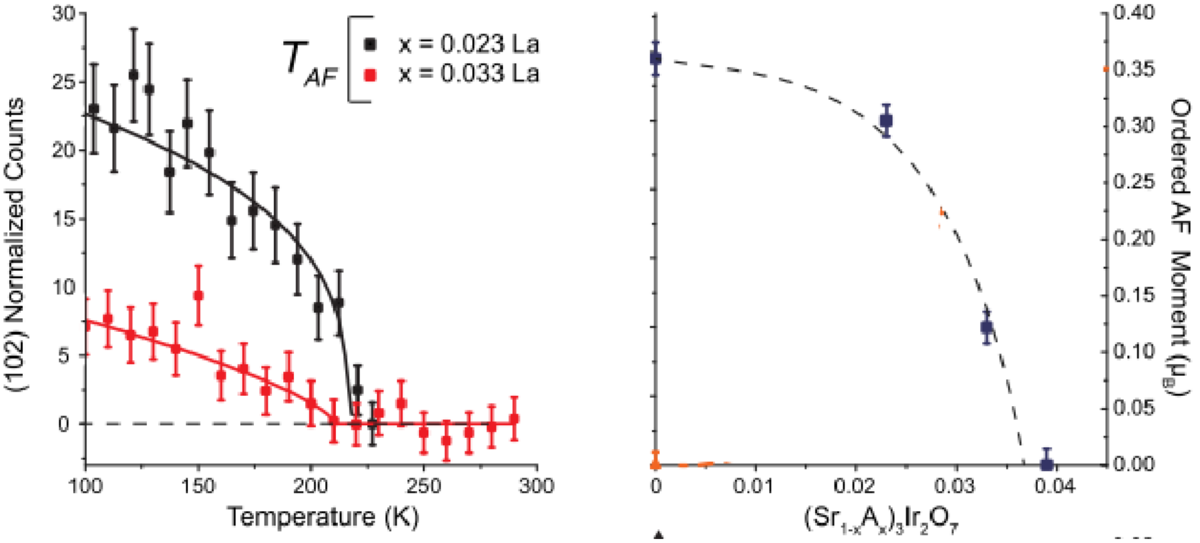

Figure 1.15: Doping evolution of antiferromagnetism in $(\mathrm{Sr}_{1-x}\mathrm{La}_x)_3\mathrm{Ir}_2\mathrm{O}_7$ measured by neutron scattering from [57]. Left: Temperature dependence of the order parameter for two samples (x $\approx 2\%, 3\%$. Right: Low-temperature orderer AF moment as a function of doping in $(\mathrm{Sr}_{1-x}\mathrm{La}_x)_3\mathrm{Ir}_2\mathrm{O}_7$.

pockets of metallic and insulating behaviors on a nanometer length scale. They further identify an additional structural transition from neutron scattering in the form of a reflection that should be symmetry-forbidden from the structure of $(\mathrm{Sr}_{1-x}\mathrm{La}_x)_3\mathrm{Ir}_2\mathrm{O}_7$, indicated by the red squares and denoted T_S in the figure. This structural distortion appears to exist in all samples with at least some metallic concentrations. Hints of further transition to a glassy state appear below 100 K in susceptibility and scattering measurements[58].

Magnetic excitation spectra

Understanding the physics of the pseudospins in $\mathrm{Sr}_3\mathrm{Ir}_2\mathrm{O}_7$ beyond the ground state is accomplished by observing the possible magnon excitations above this ground state. This is accomplished via resonant inelastic x-ray scattering (RIXS) where the difference in energy and momentum between x rays incident upon the sample and those that reach the detector after scattering is used to infer the energy and momentum of excitations in the sample. This spectrum for undoped $\mathrm{Sr}_3\mathrm{Ir}_2\mathrm{O}_7$ is shown in figure 1.17 along high symmetry directions in momentum space. There are three distinct features in this spectrum: elastic and nearly-elastic scattering events (A), a dispersive magnon band (B), and a weaker, broader two-magnon spectrum (C). The magnon dispersion B is notable for the absence of an acoustic branch and the large gap between the band minimum near (π, π) and zero energy. An acoustic mode is generally expected as a consequence of symmetry and Goldstone's theorem, but the broken rotational symmetry caused by pinning the pseudospins to the c axis allows for a gap

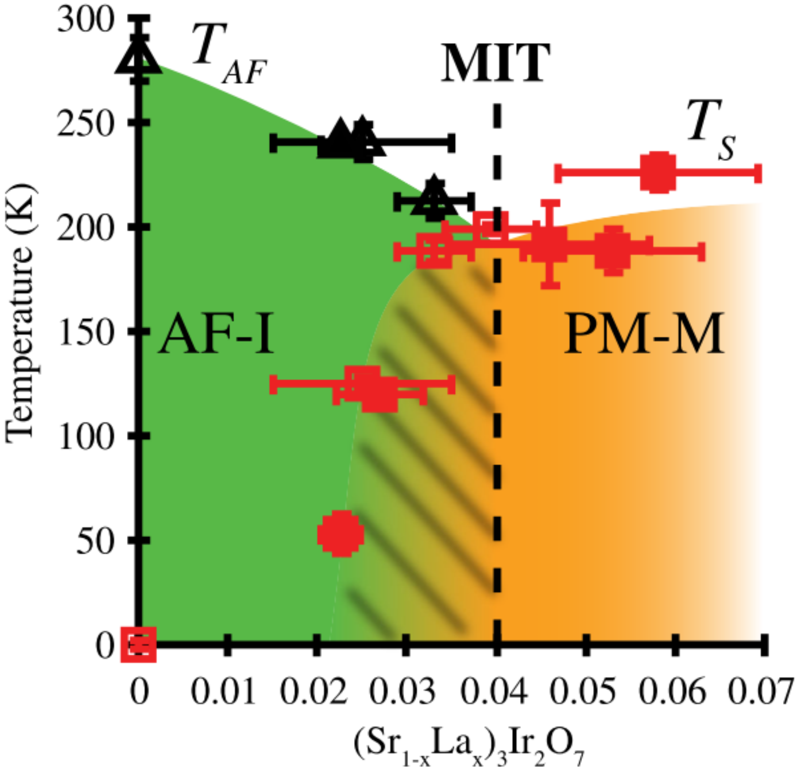

Figure 1.16: Phase diagram of $(Sr_{1-x}La_x)_3Ir_2O_7$ from scattering and transport

in the expectation spectrum. This same experiment can be performed on doped samples, with results shown in figure 1.18. The three panels of this figure show RIXS spectra for an x = 0, x = 0.02, and x = 0.065 sample, which correspond to the parent, doped antiferromagnetic, and doped paramagnetic ground states, respectively. The primary change with doping is the decrease and eventual closure of the gap at the band minimum. This corresponds to the suppression of anisotropic terms in the spin Hamiltonian, and indeed the magnetic correlations along the c axis are suppressed at higher doping levels. The continued existence of well-defined magnon dispersion is a sign of remnant short range order in the system beyond the region of the phase diagram where the long range antiferromagnetic ground state exists[59].

1.3.3 Optical properties

Equilibrium optical conductivity

The optical conductivity spectra of $Sr_3Ir_2O_7$ are shown in figure 1.19. The two peaks α and β correspond to direct optical transitions at energies $\hbar\omega \approx 0.35$ eV and 0.8 eV, which is consistent with published band structure calculations of $Sr_3Ir_2O_7$. At higher temperature,

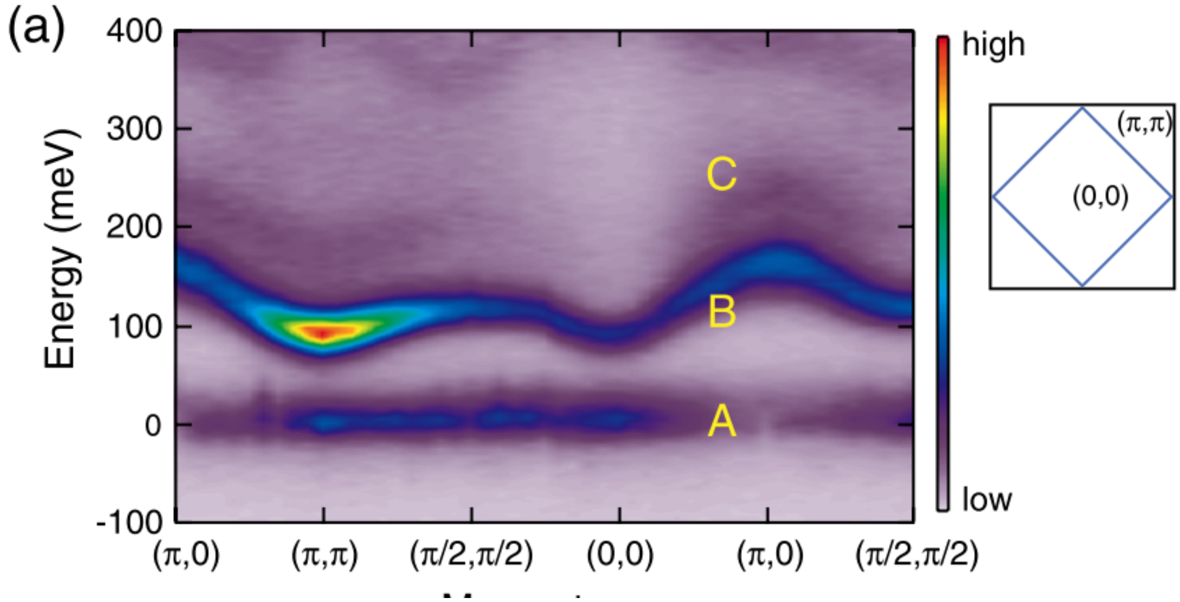

Figure 1.17: Magnon dispersion along high-symmetry directions in $Sr_3Ir_2O_7$, measured by RIXS

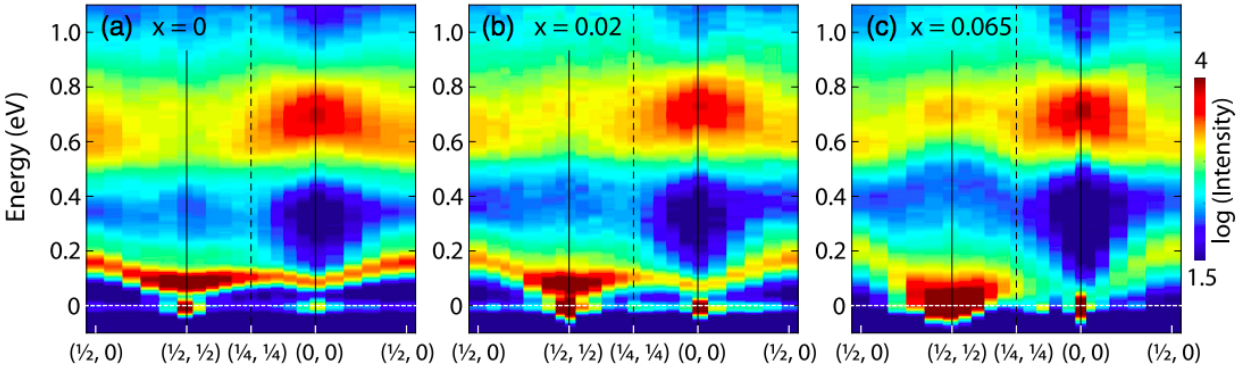

Figure 1.18: Magnon dispersion along high-symmetry directions in $(Sr_{1-x}La_x)_3Ir_2O_7$, measured by RIXS, for three different doping levels.

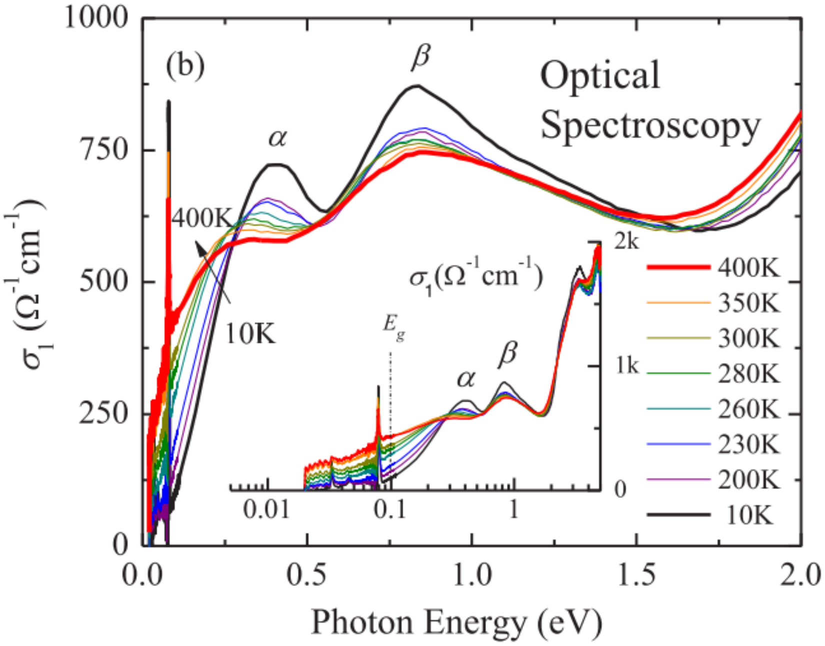

Figure 1.19: Infrared optical conductivity of $Sr_3Ir_2O_7$ as a function of temperature, from [60]. Inset: the same data on a semilogarithmic plot.

these features broaden and weaken, and the peak labeled α shifts to lower energy. The broadening of these peaks is expected, as the increase in the population of phonons provides more channels with slightly different energy for the interband transitions. The shift of the α peak is attributed to the emergence of states near E_F at high temperature. The features at lower energy are directly related to phonons in the system. The sharp edge near the indirect gap energy of 0.1 meV corresponds to interband transitions, where phonons in the system provide the necessary momentum and enhance the conductivity here with increasaing temperature. The sharp peaks at lower energy correspond to optical phonons, discussed below. Figure 1.20 (a) and (b) show the optical conductivity near three optical phonon modes at low energy in $Sr_3Ir_2O_7$ for a range of temperatures. The two lower-energy modes near 264 cm^{-1} and 374 cm^{-1} are identified as bending modes of the in-plane Ir-O-IR bond. The higher energy mode near 639 cm^{-1} corresponds to stretching of the Ir-O bond along the c axis. All three of these modes have relatively flat dispersions [60] and can contribute to the indirect gap transitions observed above. Panel (c) shows the relative shift of these phonon energies with temperature, with virtually no change in the 264 cm^{-1} and 639 cm^{-1} modes over the range measured. The 374 cm^{-1} mode, however, decreases in energy by roughly 6% between 10 K and 400 K. This softening suggests that the O ions can have large displacements perpendicular to the Ir-O-Ir bond direction at high temperature, as illustrated in the inset to panel (c), which in turn may affect the hopping properties and magnetic interactions at high temperature.

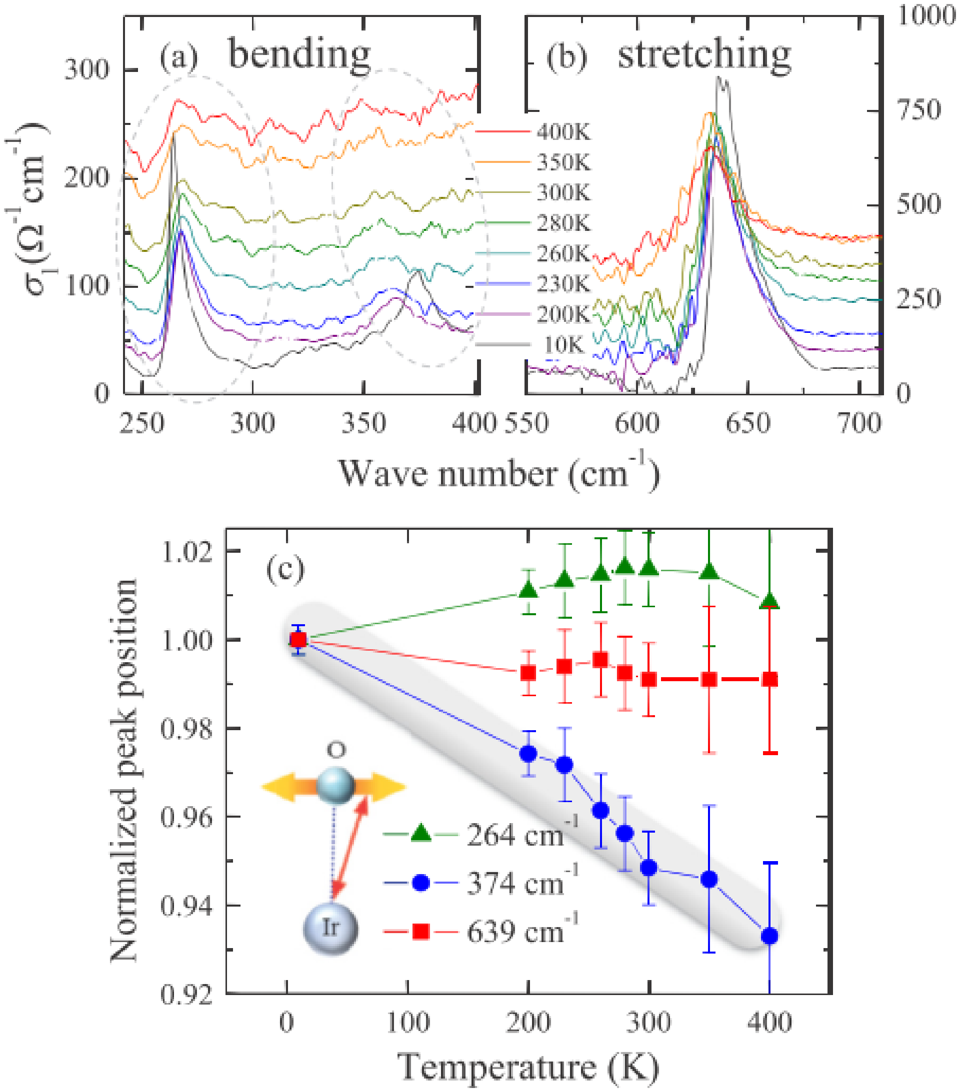

Figure 1.20: Phonon modes in $Sr_3Ir_2O_7$ from [60]. Top: Optical conductivity at energies corresponding to bending (left) and stretching (right) phonon modes in $Sr_3Ir_2O_7$ as a function of temperature. Bottom: Shift in phonon peak positions with temperature.

Charge density wave-like instability

In addition to equilibrium properties, optical reflectivity experiments are well-suited to probing sample phenomena at an ultrafast timescale, shedding light on dynamical properties and instabilities toward orderings not found in equilibrium. The results of one such experiment are shown in figure 1.21 for a metallic (x = 5.8%) $(\mathrm{Sr}_{1-x}\mathrm{La}_x)_3\mathrm{Ir}_2\mathrm{O}_7$ sample. Shown in panel a is the change in reflectivity of 1.55 eV photons after an intense pump pulse (fluence $\approx 400\mu\mathrm{J/cm}^2$) of the same energy. For experimental reasons, this transient is normalized to the overall reflectivity at that energy. In each of these curves, there is a sharp peak near zero delay (corresponding to temporal overlap of pump and probe) caused by rapidly-decaying high energy excitations followed by a slower decay and weak oscillations. The amplitude of these oscillations is plotted as a function of temperature in panel b, and shows a rapid onset near 200 K and saturation at very low temperatures, similar to an order parameter. This temperature of 200 K corresponds closely to the structural distortion temperature for this doping in figure 1.16. Indeed, this trend holds for a range of samples from x = 2.7 % out to this measurement at x = 5.8%, suggesting a connection between the structural distortion and an instability toward density-wave behavior. This supports a picture of $(\mathrm{Sr}_{1-x}\mathrm{La}_x)_3\mathrm{Ir}_2\mathrm{O}_7$ as a system with many competing ground states close in energy, even into the metallic regime away from the parent Mott state.

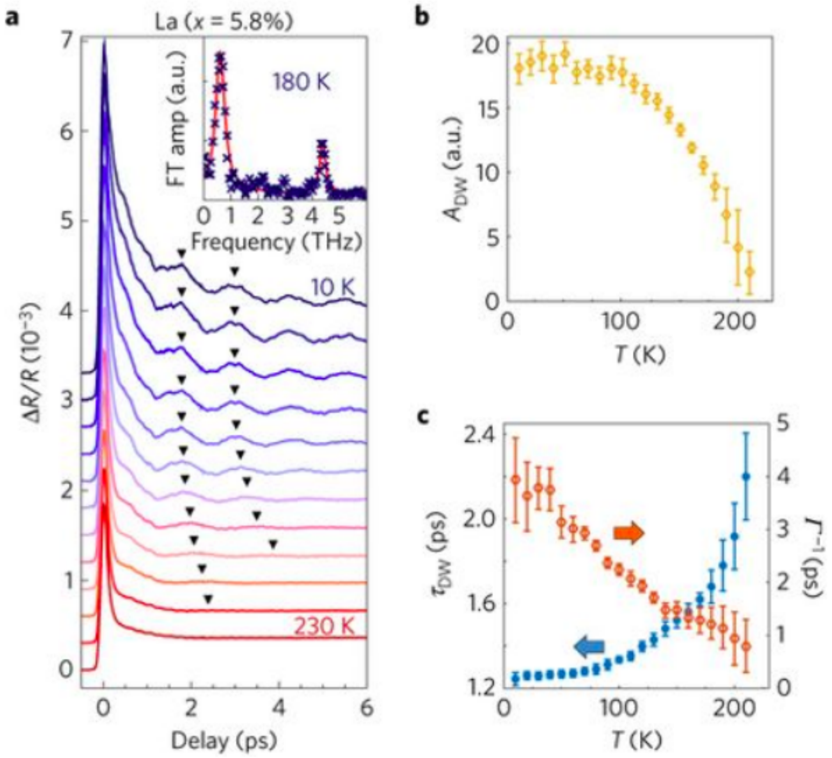

Figure 1.21: Ultrafast reflectivity oscillations in a metallic x =5.8% $(Sr_{1-x}La_x)_3Ir_2O_7$ sample, from [61]. a: Reflectivity transients as a function of temperature. b: Reflectivity oscillation amplitude as a function of temperature. c: Reflectivity oscillation period and damping time as a function of temperature.

Chapter 2

Angle-resolved photoemission spectroscopy

The majority of the work presented in this dissertation uses the experimental technique of angle-resolved photoemission spectroscopy (ARPES). This chapter outlines the theory behind this experiment and its interpretation, as well as practical concerns in both the experimental realization and its analysis. The final section is a brief introduction to spin-resolved ARPES, used in chapter 4.

2.1 Theory of ARPES

At its most basic level, the ARPES experiment can be understood classically in terms of simple conservations laws. An electron in a solid with binding energy E_b absorbs an incident photon of energy $h\nu$ and is emitted from a sample, so its vacuum kinetic energy is given, as in the photoelectric effect, by conservation of energy as

$$E_{\text{kin}} = h\nu - E_b - \phi \tag{2.1}$$

where ϕ is the sample work function. Additionally, discrete translational symmetry of the lattice along the surface direction gives rise to conservation of crystal momentum in that direction, so that an electron in the solid with in-plane crystal momentum $k_\parallel$ is emitted at an angle θ to the sample normal satisfying

$$\hbar|\vec{k_\parallel}| = \sqrt{2m_e(h\nu - \phi - E_b)}\sin\theta \tag{2.2}$$

Thus, by measuring the kinetic energy of an outgoing electron and its angle relative to the sample surface, we can infer its state before the photoemission process, up to an unknown momentum component normal to the surface where translation symmetry is explicitly broken by the sample-vacuum interface. There are, however, techniques for addressing this k_z, discussed in section 2.2.3.

While the above semi-classical treatment of the photoemission process relates the measured quantities of an outgoing electron with properties of its internal state, understanding the overall state of the electrons in a solid from such data requires the analysis of the probability that electrons in each state are photoemitted in the first place[62]. This is treated quantum mechanically by Fermi's golden rule, where the probability for a transition w_{fi} is given by

$$\frac{2\pi}{\hbar}|< f|H_{\text{int}}|i >|^2\delta(E_f - E_i - h\nu) \tag{2.3}$$

for an initial state $|i >$ and a final state $|f >$, driven by a photon of energy $h\nu$. The interaction Hamiltonian H_{int} comes from the typical Hamiltonian involving an electron in a field:

$$\begin{aligned} H &= \frac{1}{2m}\left(p - \frac{e}{c}A\right)^2 + e\phi & (2.4)\\ &= \frac{1}{2m}\left(p^2 + \frac{e}{c}p \cdot A + \frac{e}{c}A \cdot p + \frac{e^2}{c^2}|A|^2\right) + e\phi & (2.5)\end{aligned}$$

It is typical to assume that the field is small so that the $|A|^2$ term can be neglected. Since $\vec{p}$ is proportional to $\vec{\nabla}$, the $\vec{p} \cdot \vec{A}$ term is small whenever the field is changing over a length scale that is long relative to the system, a reasonable assumption for our purposes as for 100 eV light, the wavelength is 12 nm, which is longer than several lattice spacings and deeper than the typical origin of measured photoelectrons and so the typical interaction Hamiltonian is

$$H_{\text{int}} = \frac{e}{mc}\vec{A} \cdot \vec{p} \tag{2.6}$$

The interaction Hamiltonian then directly depends on the polarization of the incoming light with respect to the momentum of an electron of interest, which will have interesting effects discussed in section 2.2.2.

A rigorous theoretical treatment of the transition matrix element in equation 2.3 would take into account the entire process, from excitation of an electron in the sample to the eventual detection, as a single coherent process, including the reaction of the many-body wavefunction inside the crystal to the emission and its subsequent effect on the measured electron. To make the problem more tractable, it is useful to make several approximations in the framework of the *three-step model*of photoemission where we consider the experiment as a sequence of independent steps: excitation of the electron in the bulk, transport to the crystal surface, and escape into the vacuum. Once the electron is in vacuum it is reasonable to treat it as a classical object subject to the focusing electric fields of the detector. This approximation allows us to treat the three steps separately and simply multiply their probabilities together to find the final detection cross section. The initial excitation step is essentially an optical transition and governed by dipole selection rules (though near the surface the additional $\nabla \cdot A$ term in the Hamiltonian will allow dipole-forbidden transitions). Probability amplitudes for this step are governed by transition matrix elements discussed in section 2.2.2. The transport of the excited electron to the sample surface is limited by its mean free path, discussed in section 2.2.1. Lastly, the transition across the sample surface is related to the sample work function, which comes from the dipole moment near the surface due to broken inversion symmetry.

The measured signal is given by

$$I(k,\omega) = MA(k,\omega)f(\omega) \tag{2.7}$$

where M is a transition matrix element that depends on the experimental geometry, intensity and energy of the incident light. Lastly, $f(\omega)$ is the Fermi-Dirac distribution (as only occupied electron states are accessible by photoemission. $A(k,\omega)$, the single particle spectral function, is the physical quantity of interest and gives the probability of an electron existing with energy $\hbar\omega$ and momentum k in the sample. The spectral function can be expressed in terms of the dispersion ϵ_k and the electron proper self-energy $\Sigma(k,\omega) = \Sigma'(k,\omega) + i\Sigma''(k,\omega)$ with Σ', Σ'' both real functions of k and ω:

$$A(k,\omega) = -\frac{1}{\pi}\frac{\Sigma''(k,\omega)}{\left(\omega - \epsilon_k - \Sigma'(k,\omega)\right)^2 + \Sigma''(k,\omega)^2} \tag{2.8}$$

In the limit of no interactions, the self energy goes to zero and the spectral function is simply a sequence of delta functions at the band energy for each k. If instead we consider only the frequent case of self-energy that is independent of k, we have

$$A(k,\omega) = -\frac{1}{\pi}\frac{\Sigma''(\omega)}{\left(\omega - \epsilon_k - \Sigma'(\omega)\right)^2 + \Sigma''(\omega)^2} \tag{2.9}$$

Considering a constant energy, this gives lineshapes that are Lorentzian with characteristic width given by Σ'' corresponding to electron lifetimes. The effect of Σ' is to change the band position relative to the underlying model, and is manifest in band velocities and masses.

2.2 Experimental considerations

There are several details in which the results of a physical ARPES experiment differ from the ideal theoretical case outlined in section 2.1. Among these, there are straightforward instrumental resolution effects which serve to broaden the linewidths in momentum and energy, matrix element effects related both to orbital symmetry and final state availability, and effects in which the photoelectron charge interacts with either other photoelectrons (space charging) or the holes left behind by the photoemission process (sample charging). The details of these effects are explored below.

2.2.1 Sample surface

In order to measure a given photoelectron, it must make its way out of the sample and to the detector. For this measurement to be meaningful (i.e., give accurate information about the state of the electron before the photoemission process) it must do so without scattering inside the sample. Thus, the depth probed by ARPES is limited by the mean free path of electrons which, for the range of exciting photon energies used in this study, is typically a few monolayers, as seen in figure 2.2.1.

ARPES is therefore an extremely surface sensitive probe and accordingly great care must be taken to ensure surface quality. To this end, most samples are cleaved *insitu* to reveal pristine inner layers as the surface, and experiments are performed in ultrahigh vacuum (typical pressures lower than 5 x 10^{-10} Torr). Even at this pressure, the number of gas molecules incident on the sample surface is sufficient to cover it over the course of a few hours.

2.2.2 Matrix element effects

While the three-step model described in section 2.1 is a simplification of the physical transitions at play in the photoemission process, it serves to logically separate out different sources of effects in an observed spectrum. The leasts intuitive of these is the so-called "transition matrix element", which depends on the initial and final states of the electron in the solid. Often this dependence is due to symmetry with respect to the scattering plane, which is defined by the incoming light vector and outgoing electron vector, shown as a green plane in figure 2.2.2, which is normal to the sample surface in this case (but not always).

If the sample is oriented such that it is symmetric under reflection across the scattering plane, then from elementary quantum mechanics we know that electron wavefunctions are eigenfunctions of this reflection, and thus either purely odd or purely even across this plane. For sufficiently high photon energy, the lattice potential has only small effect on the electron final state and thus its wavefunction is nearly a plane wave:

$$\psi_{\vec{k_f}} = (\vec{r}) \approx e^{i\vec{k_f}\cdot\vec{r}} \tag{2.10}$$

which is clearly even with respect to the scattering plane and the matrix element suppresses intensity for odd initial states if the light polarization is even and vice versa, while allowing transitions where the initial state and light polarization have the same parity with respect to this plane. In the case of normal emission, the outgoing electron wavefunction will have axial symmetry along the sample normal. This can give significant suppression to the intensity of states near the center of the first Brillouin zone, and often necessitates measurements near the zero crystal momentum Γ point in higher Brillouin zones to see all bands.

In some systems the wave function of an electron band is closely related to the atomic or molecular orbitals from which they are derived. In particular, for the near-E_F states in $Sr_3Ir_2O_7$, the bands are derived from a mixture of three $5d$ states–$|xy>$, $|xz>$, and $|yz>$. In the case of measurement at the Brillouin zone corner, the scattering plane coincides with

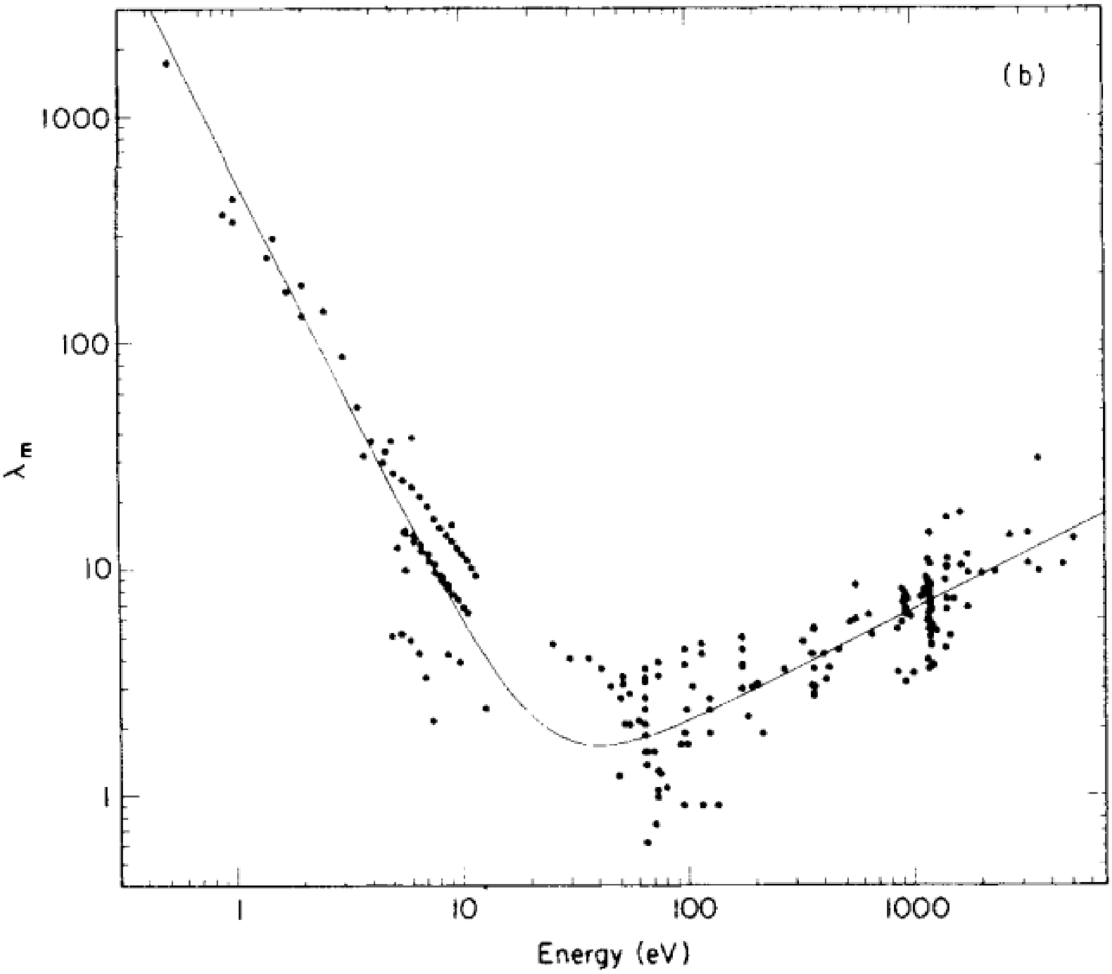

Figure 2.1: Inelastic mean free path for electrons in various materials

the sample xz-plane, and changing between s and p polarized light highlights the $|xz>$ (even) and $|yz>$, $|xy>$ (odd) orbitals.

2.2.3 Out-of-plane momentum considerations

While the in-plane (crystal) momenta are conserved by the photoemission process, symmetry is broken along the direction normal to the sample surface and thus there is no straightforward conservation law for the momentum in this direction (k_z)–it will necessarily change as the photoelectron crosses the surface from the sample into vacuum. To access information about k_z, it is common to employ the sudden approximation, in which it is assumed that this change takes place over a time sufficiently short that the electron does not interact with the solid other than a step change in its momentum. It is common to further assume that

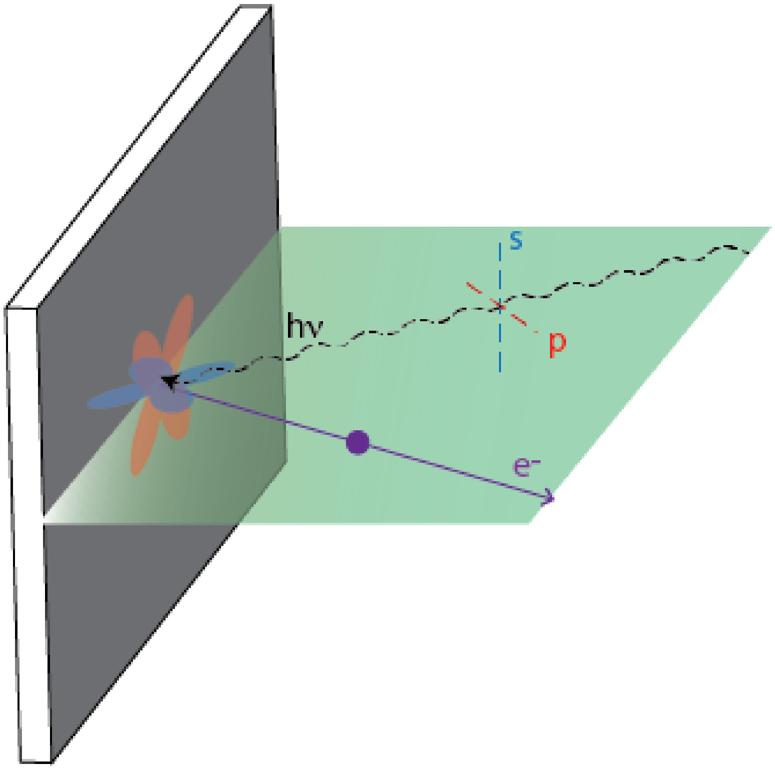

Figure 2.2: Schematic of the scattering geometry for an ARPES experiment

the state of the electron after excitation is well-described by a free-electron-like state (which holds better at higher excitation energies), given by a dispersion

$$E_f = \left(\frac{\hbar^2}{2m}\right)\left(k^2\right) - \phi - V_0 \tag{2.11}$$

where the zero of energy is set to the vacuum, ϕ is the sample work function, and V_0 is a parameter known as the inner potential to be determined experimentally[63]. Under this assumption, conservation of energy gives

$$k_z = \frac{1}{\hbar}\sqrt{2m_e\left(h\nu - \phi - V_0\right) - k_{\parallel}^2}$$

In order to determine V_0, it is most common to measure a set of spectra at normal emission so that $k_{\parallel} = 0$ with a range of incident photon energies, thus changing kinetic energies of the photoelectrons and k_z. For 3D materials, there will be some variation in band locations due to dispersion with k_z, which should be periodic with period $\frac{2*\pi}{c}$, where c is the lattice spacing along the z direction. If this dispersion is taken to be sinusoidal in k_z, then one can fit it with the form

$$\begin{aligned} E(k_z) &= A\sin(k_z c + B) + C && (2.12)\\ &= A\sin\left(\frac{c}{\hbar}\sqrt{2m_e\,(h\nu - V_0)} + B\right) + C && (2.13)\\ & && (2.14)\end{aligned}$$

with the four parameters A, B, C and V_0 to get the inner potential and thus an estimate of the perpendicular momentum k_z.

2.2.4 Sample charging and space charging

Much of the discussion up to this point has considered the ARPES experiment as the measurement of a single photoemitted electron from a system in equilibrium. In reality, the high repetition rate and brightness of both synchrotron and laser light sources for ARPES can give rise to effects that skew the measurement. In measurements where many electrons are emitted in the same bunch, space charging effects can negatively effect energy resolution. Conceptually, this consists of faster electrons being sped up and slower electrons being slowed down by the Coulomb repulsion of electrons in the same bunch. Insulating samples, though well grounded, can have a build up of holes due to photoemitted electrons and long recovery times that serve as a potential lowering the energy of subsequent photoelectrons and shifting all measured bands to higher apparent binding energy. The standard method for assessing whether a measurement is subject to either of these effects is to measure with a range of incoming photon intensities, as each becomes more significant with increasing frequency of photoemission.

2.3 ARPES analysis

Most modern ARPES experiments are conducted using a two-dimensional detection scheme, measuring photoemission intensity over a range of energies and emission angles simultaneously. By taking several such spectra in different experimental geometries and appropriate conversions of emission angles to crystal momenta, one quickly builds a three-dimensional spectrum $I(k_x, k_y, E)$ that needs to be broken down into tractable pieces. For the extraction of physical quantities, it is common to restrict oneself to a one-dimensional space and examine the intensity curve. If momentum is held fixed and the intensity varies with energy, one has and energy distribution curve (EDC). Similarly, if energy is held fixed and one takes the intensity as a function of momentum along some direction, one has a momentum distribution curve (MDC). Alternatively, one can attempt to extract information from two-dimensional slices, either with two dimensions in momentum (referred to as a constant energy map or CEM), or one energy and one momentum (referred to here as an E-k cut). These images are often useful for getting an overall picture of the band structure, but for extracting quantitative information it is more precise to use EDCs or MDCs. In this section we discuss the details of each of these types of analysis, and then apply them to the problem of extracting physical information from a model dataset.

2.3.1 Analysis methods

EDC analysis

A frequently-used model for the inelastic background in an ARPES experiment is the so-called Shirley background, where one considers that an electron may scatter to any state with lower energy, irrespective of momentum, with equal probability

$$I_{\mathrm{BG}} = \int_{\omega}^{\infty} I_0(\omega')d\omega' \tag{2.15}$$

In reality, the details of the background will be more complicated and depend on the details of scattering channels available to photoemitted electrons (e.g., available bosons). Further, the calculation of such a background is simple given a known density of states, but that is not the situation realized in experiments. The calculation of a background only from a spectrum that includes both intrinsic features and the background is difficult, but realizable using iterative methods with an initial guess for the intrinsic structure. It is thus common to use a phenomenological background to fit EDCs when details of the peak are desired. From the form of the Shirley background we see that it should be relatively featureless at energies with no intrinsic density of states, and thus that fitting a smooth phenomenological background at energies away from peaks corresponding to bands will give a similar result more simply.

MDC analysis

For bands away from their extrema, it is common to use MDC analysis to extract the dispersion relation (i.e., $E(\vec{k})$, though this procedure directly gives $\vec{k}(E)$). This is preferred to EDC analysis largely due to the relative momentum independence of the self energy, which gives us the spectral function in equation 2.9. For a fixed energy, the band is simply Lorentzian, which is easy to fit and extract a peak position. These peak positions can be inverted to give the dispersion $E(k)$, which is useful for extracting information about the bandwidth, velocity, and effective masses. If an accurate model of the noninteracting dispersion ϵ_k is known, the difference $E(k) - \epsilon_k$ is a measure of the real part of the electron self-energy.

In addition to extracting band dispersions, MDC analysis is useful for evaluating the size of the Fermi surface. Luttinger's theorem shows that, even in the presence of electronic interactions (i.e., nonzero self energy), the volume of the Fermi surface as a fraction of the Brillouin zone is proportional to the carrier concentration in the system. The Fermi surface in this case is defined by the peaks of the spectral function with momentum. In practice, it is useful to combine MDC fitting with two-dimensional analysis to fit a curve with the appropriate Fermi surface shape to the MDC peaks, rather than summing the Fermi surface area implied by each individual MDC.

2.3.2 Application to gap extraction

Among the most meaningful physical quantities that can be extracted from an ARPES spectrum is an excitation gap, which can have importance as an indicator of physical properties (as in a semiconductor) or even be an order parameter for a ground state in the system (as in superconductors, magnets). The concept is straightforward–we are looking for the energy difference between the maximum of some band and the minimum of another. In cases where the upper gap edge is unoccupied (and thus not visible in an ARPES spectrum), the distance between the highest band maximum and the chemical potential serves as a useful lower bound for the gap. In practice, the chemical potential in these situations is determined by measuring a metal in good electrical contact with the gapped system (usually polycrystalline gold) to get a good reference. There are also some system (e.g., cuprate superconductors) where only a portion of the Fermi surface is gapped, and thus the chemical potential can be taken from a spectrum at the ungapped momentum points.

Several details in the data analysis make gap determination difficult and there are many techniques for doing so, each with strengths and weaknesses. These are discussed below and applied to artificial data, shown in figure 2.3.2. In panel (a) we have a sample dispersion consisting of an electron-like band crossing the Fermi level and one valence band maximum deep below E_F. In panel (b) we have a mock ARPES spectrum, with Lorentzian broadening of the dispersions and a finite-temperature Fermi-function cutoff applied. Additionally, we have added a Shirley-like background function $I_{\text{BG}}(\omega) = \alpha \int_{\omega}^{\infty} I_{\text{intr}}(\omega')d\omega'$. In evaluating each of these techniques for gap extraction, it is desirable to have a gap value near to that of the underlying dispersion. It is physically more relevant, in light of the ordered-state origin of many gaps, to be certain that a method does not indicate a nonzero gap when none exists. The potential for false gaps in each will be discussed.

EDC analysis

The most natural method for finding the position of a band edge is by analyzing the EDC through the band extremum or, in the case of bands that apparently disperse across E_F, at the Fermi momentum. In either case the correct momentum is determined by the peak in the MDC at the correct energy (either E_F or near the extremum of the band). In the oversimplified case that the peak is far from the Fermi level, the self-energy is varying slowly with energy, and small background signal, this EDC will be marked by a peak at the band energy whose maximum can be taken as the location of the band edge. Each of the previous assumptions will fail in general, giving rise to complications with using the EDC to determine the band edge. Since the Fermi-Dirac distribution has a negative slope in a window around E_F, peaks near the Fermi energy will be apparently shifted to the deeper binding energy, and thus this measure can indicate gaps where none exist. Fitting the product of a peak and a

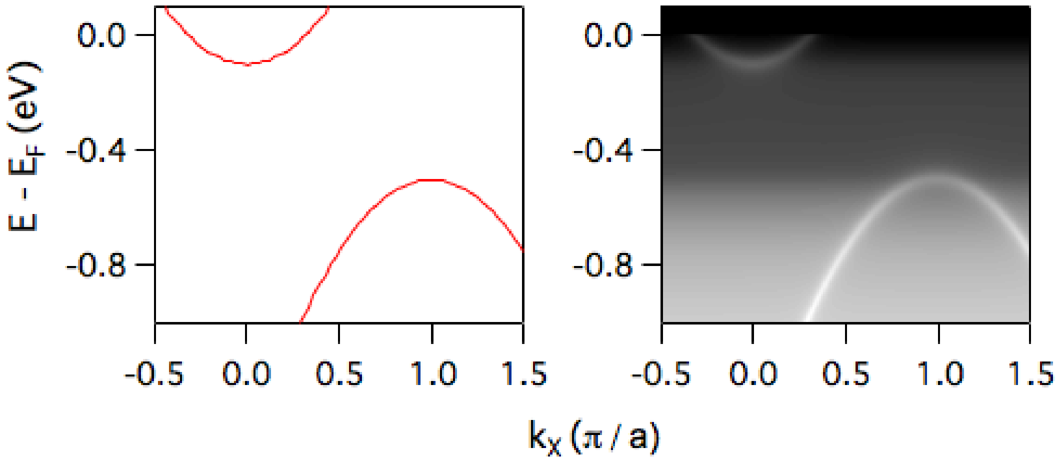

Figure 2.3: Simulated ARPES spectrum for gap determination

Fermi cutoff is difficult, as moving a peak to higher energies where the Fermi function is small gives only a small shift in the apparent peak position. If, however, the gap is significantly larger than kT and the background is flat (or at the worst, locally linear), fitting to a peak (possibly including a background slope) will give an excellent indicator of peak position. A more robust method of extracting a gap from an EDC near E_F is to take the leading edge midpoint, i.e., the energy at which the spectrum attains half its peak value. Since the bare spectrum (before considering the Fermi function) is unlikely to have a negative slope at E_F unless the peak corresponding to the band is below E_F, this midpoint should not move to deeper binding energy when no gap exists.

A sample EDC analysis of the band crossing E_F in our sample data is presented in figure 2.3.2. Panel (a) shows the two-dimensional cut of interest, with a red line marking the Fermi level (at which the MDC in panel c is taken) and a blue line marking the location of k_F (at which the EDCs in panels b and d are taken). In panel d, the EDC has been zoomed in to the area near the Fermi level, and both the leading edge midpoint and peak position have been marked with red Xs. It is clear here that the peak is at some negative binding energy, while the leading edge midpoint remains at the Fermi level.

MDC dispersion analysis

As discussed in section 2.3.1, it is common to extract the position of valence bands in ARPES spectra by fitting peaks to MDCs for each binding energy, and tracing out the peak locations to recover a dispersion. The application of this to gap extraction is conceptually simple–one finds the extremum energy of a band's dispersion, and sets that as either the upper or lower gap edge–and avoids the issues with the Fermi cutoff and energy-dependent background inherent in EDC analysis. In practice, there are two complications with this

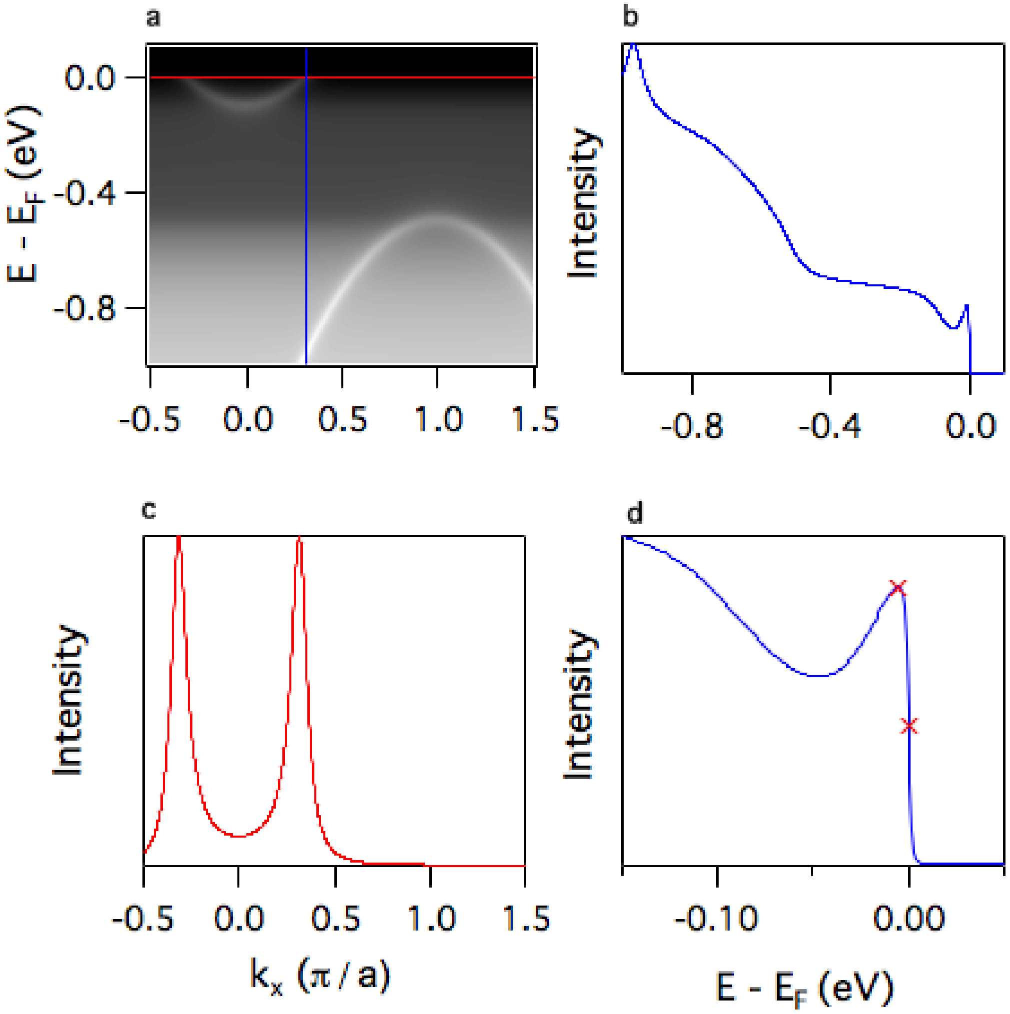

Figure 2.4: Using EDC peak analysis to find a band position

technique. First, as a band flattens out toward its extremum, the more difference there is in band positions between adjacent energy levels, and the energy broadness in the measurement (both inherently from correlation effects and due to limited experimental resolution) serves to make MDC peaks increasingly broad. In cases where matrix elements allow the observation of both sides of a dispersion, the two peaks corresponding to the band will also merge, making tracing the individual peaks difficult. The second effect is that even at energies above the band maximum (or below the band minimum), the energy broadness of the measurement will give rise to MDC peaks where there is no band. While naively this seems a problem, it also provides a route to using MDC analysis to extract band edge positions; beyond the edge of the band, the dispersion will tend toward being vertical, and thus the inflection point of the fit parameter corresponding to the peak location is a reasonable estimate of the band

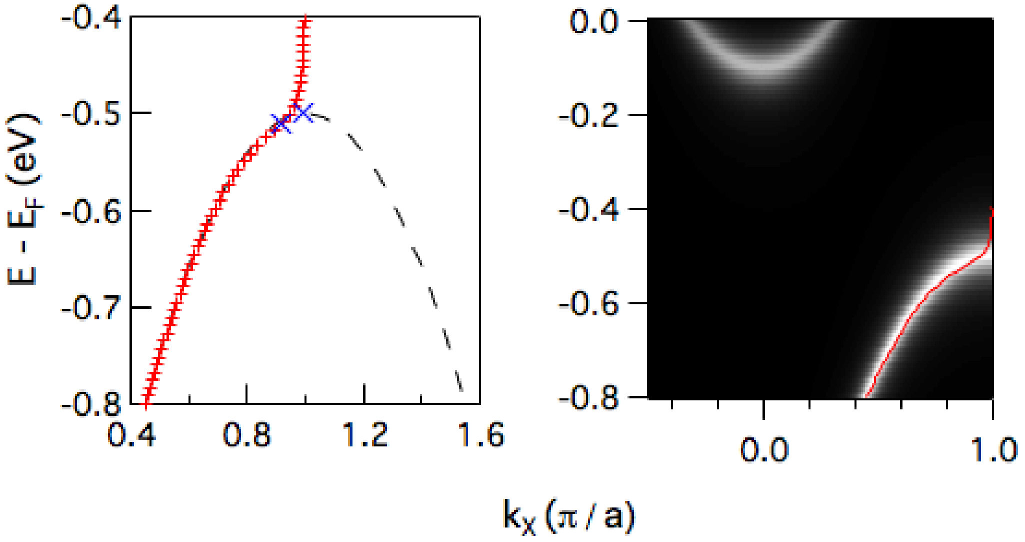

Figure 2.5: Using MDC analysis to find a band edge

edge.

A sample use of this technique for determining a band edge position is shown in figure 2.3.2. The left panel shows the underlying dispersion with a dashed black curve, and MDC peak locations with red crosses. The blue X markers correspond to the positions of the MDC peak upturn and the true band maximum.

In this case, the MDC dispersion analysis reports a larger gap than is present in the data. It is thus possible that this analysis could report a non-zero gap in an ungapped system if a band disperses very near to but does not cross the Fermi level. It additionally suffers from the need for exceedingly high statistics–to get reliable information the signal-to-noise ratio in each of the MDCs must be sufficiently high for the fits to converge.

EDC symmetrization

In special cases where one expects the spectral function to be symmetric with respect to the chemical potential (particle-hole symmetry), one can use symmetrization of EDCs to remove the effect of the Fermi-Dirac distribution from the measured spectrum. That is,

$$\begin{aligned} I(k,\omega) + I(k,-\omega) &= f(\omega)A(k,\omega) + f(-\omega)A(k,-\omega) \quad (2.16)\\ &= f(\omega)A(k,\omega) + (1-f(\omega))A(k,\omega) \quad (2.17)\\ &= A(k,\omega) \quad (2.18)\end{aligned}$$

where we have used that $f(-\omega) = 1 - f(\omega)$ and assumed $A(k,\omega) = A(k,-\omega)$. This is not generally valid, but has been used with success in specific cases where particle-hole symmetry is a reasonable assumption (in particular, in the case of the superconducting gap).

2.4 Spin-resolved ARPES

The last section of the experimental work in this dissertation is an extension of the ARPES experiment that sensitivity to the spin degree of freedom. The utility of this comes from the possibility for bands to be split by electron spin. This occurs in ferromagnets, where spin up and spin down electrons are separated by a constant offset due to the magnetism; in Rashba and Dresselhaus states (as discussed in section 1.1.2), where the spin of an electron is locked to its momentum; and in novel topological states such as the three-dimensional topological insulator. In this last case, the ability to observe the separate band crossings of spin-up and spin-down electrons is essential for identifying topological states and spin-resolved ARPES has proved an invaluable tool in that field.

In practice, there are two distinct methods employed for analyzing the spin of photoelectrons. In the conventional Mott detector, electrons are accelerated to relativistic energies and scatter off of a target with heavy nuclei (typically gold) and thus strong spin-orbit coupling which preferentially reflects electrons with different spins in different directions. This is typically coupled with a hemispherical electron detector for energy spectroscopy. In contrast, the detector used in this work was custom built and utilizes time-of-flight energy spectroscopy along with a low-energy exchange polarimeter[64], which has different reflectivity for electrons polarized parallel and antiparallel to its magnetization. Experiments are conducted by short (typically one minute) periods of measurement with alternating magnetizations of the scattering target. Because this operates at a lower kinetic energy, overall reflectivity is higher than in the case of the Mott detector. The time-of-flight energy analysis also allows for simultaneous detection of electrons with different energies but the same emission angle, increasing experimental efficiency.

A quantity of significant interest in spin-resolved ARPES measurements is the spin asymmetry at a particular momentum and energy,

$$P_{intr}(k,\omega) = \frac{A(k,\omega,\uparrow) - A(k,\omega,\downarrow)}{A(k,\omega,\uparrow) + A(k,\omega,\downarrow)} \tag{2.19}$$

Since the Fermi function is independent of the electron spin, and assuming for the moment that the matrix elements M_σ are independent of spin (this is not always the case as will be discussed later in this section), then this intrinsic polarization is the same as the photoelectron polarization

$$P_{intr}(k,\omega) \approx \frac{I(k,\omega,\uparrow) - I(k,\omega,\downarrow)}{I(k,\omega,\uparrow) + I(k,\omega,\downarrow)} \tag{2.20}$$

It is not generally possible to directly measure the spin-up and spin-down currents separately; a differential measurement is used with finite efficiency in terms of filtering spins. In the exchange polarimetry scheme used in this work, measurements are alternated with opposite target magnetization, which gives different reflectivity for opposite spins. Suppose the first measurement is taken with the exchange target polarized up, so that the reflectivity of spin-up electrons is higher than that of spin-down electrons by a factor α.

$$R_\uparrow = R; R_\downarrow = \alpha R \tag{2.21}$$

The incident beam will have N total electrons, $N_\uparrow$ with spin up and $N_\downarrow$ with spin down. Upon reflection from the target, the number of electrons measured will be

$$N_1 = RN_\uparrow + \alpha RN_\downarrow \tag{2.22}$$

After flipping the magnetization of the target, the reflectivity in the spin-up and spin-down channel will switch, and the number of electrons measured will be

$$N_2 = RN_\downarrow + \alpha RN_\uparrow \tag{2.23}$$

so that to get the incident polarization P we take

$$\begin{aligned}
\frac{N_1 - N_2}{N_1 + N_2} &= \frac{N_\uparrow + \alpha N_\downarrow - N_\downarrow - \alpha N_\uparrow}{N_\uparrow + \alpha N_\downarrow + N_\downarrow + \alpha N_\uparrow} && (2.24)\\
&= \left(\frac{1-\alpha}{1+\alpha}\right)\left(\frac{N_\uparrow - N_\downarrow}{N_\uparrow + N_\downarrow}\right) && (2.25)\\
&= S_{\text{eff}} P && (2.26)
\end{aligned}$$

where S_{eff} is the effective Sherman function, a measure of how efficient a spin polarimeter is at differentiating opposite spins. It is related to the overall scattering cross section at angle θ via

$$\sigma(\theta) = \sigma_0(\theta)\left(1 + S_{\text{eff}}(\theta)\boldsymbol{P}\cdot\hat{\boldsymbol{M}}\right) \tag{2.27}$$

and is determined via scattering with a known spin-polarized electron beam. The desired polarization is thus inferred from inverting the previous equation for P. The uncertainty in this polarization is given by

$$\Delta P = \frac{1}{\sqrt{N}S_{\text{eff}}} = \frac{1}{\sqrt{N_0 R_0}S_{\text{eff}}} \tag{2.28}$$

where N is the number of measured electrons, N_0 is the number of incident electrons and R_0 is the overall reflectivity of the target. The typical figure of merit for spin detectors is

$$FOM = \frac{(\Delta P)^2}{N_0} = S_{\text{eff}} R_0 \tag{2.29}$$

2.4.1 Spin-dependent matrix elements

In interpreting the results of a spin-ARPES measurement, it is important to understand effects other than a polarization in the band that may give rise to a nonzero measured polarization. While the photoemission process does not include impetus for the electron spin to change direction once it has left the sample, it is possible for electrons of a given spin to be preferentially emitted. That is, the matrix element can differ for opposite spins, which will change the measured spin polarization from that intrinsic to the band, or even give rise to a nonzero polarization in a spin-degenerate band. In the common case of linearly-polarized light incident upon an atomic system, the spin polarization induced by these spin-dependent matrix elements is[65]

$$\vec{P}_{\mathrm{SME}} = \frac{2\xi\left(\hat{k}_e \cdot \hat{\epsilon}\right)}{1 + \beta\left(\frac{3}{2}(\hat{k}_e \cdot \hat{\epsilon})^2 - \frac{1}{2}\right)}\left(\hat{k}_e \times \hat{\epsilon}\right) \tag{2.30}$$

where ϵ and k_e are unit vectors in the directions of the photon polarization and electron momentum, respectively, β is an (material-dependent) asymmetry factor and ξ is a factor related to the transition amplitudes from a state with angular momentum ℓ to stats with angular momentum $\ell - 1$ and $\ell + 1$ which couple to the spin degree of freedom and give rise to the polarization. The geometric conditions for nonzero polarization from this effect are that the incident photon polarization and outgoing electron momentum are neither parallel nor perpendicular. In the geometry of figure 2.2.2, this means that the spin-dependent matrix elements are zero with an s polarized photon beam but not, in general, for a p polarized beam.

While the calculations leading to equation 2.30 are for free atomic systems, they have been shown to hold qualitatively for spin-resolved photoemission from core levels of several metallic systems[66, 67, 68], as well as in the Bi core levels, valence band, and conduction band of $\mathrm{Bi_2Se_3}$ [69].

The factors β, ξ, can depend on the material being measured, but for a given sample the spin is dependent only on the experimental geometry. In particular, since different momentum states are measured in our experiment by turning the sample and leaving $\hat{k}_e$ fixed, the expression is independent of $\vec{k}$ and can be accounted for by a constant offset across the entire Brillouin zone which can be determined by measuring the spin polarization at normal emission.

Chapter 3

Electronic structure of $(\mathbf{Sr}_{1-x}\mathbf{La}_x)_3\mathbf{Ir}_2\mathbf{O}_7$

This chapter explores work done using spin-integrated ARPES endstations at the Advanced Light Source to determine the ground state properties of $(Sr_{1-x}La_x)_3Ir_2O_7$, a series of electron-doped compounds related to the parent spin-orbit Mott insulator $Sr_3Ir_2O_7$. As discussed in chapter 1, transport and scattering experiments identified a first-order insulator-to-metal transition near a doping level of $x = 4\%$ that coincides with the antiferromagnetic-to-paramagnetic transition, and will form an important benchmark for other phenomena discussed in this chapter. Most of this work and many of the figures come from two papers [70, 71].

Sections 3.2, 3.3, and 3.4 will explore effects that are understandable at the level of conventional band theory, in particular the states populated by the donor electrons, the changes in band splittings due to modified effects of interactions relevant to $Sr_3Ir_2O_7$ (Coulomb correlation, spin-orbit coupling, bilayer splitting), and the dispersions of bands near the Fermi level. Then section 3.5 will discuss a novel suppression of spectral weight in the conduction band of $(Sr_{1-x}La_x)_3Ir_2O_7$ that is reminiscent of the pseudogaps in cuprates and doped Sr_2IrO_4 and appears to be closely tied to the magnetic ordering in the system. Section 3.6 covers a temperature-dependent loss of coherence in the conduction band across the entire phase diagram, and its place in the known phase diagram for $(Sr_{1-x}La_x)_3Ir_2O_7$.

3.1 Introduction: Electronic structure of $\mathbf{Sr}_3\mathbf{Ir}_2\mathbf{O}_7$

In working toward the electronic structure and properties of $(Sr_{1-x}La_x)_3Ir_2O_7$, it is useful to first examine the electronic structure of the parent compound $Sr_3Ir_2O_7$[72]. As described in the first chapter, $Sr_3Ir_2O_7$ is a spin-orbit assisted Mott insulator with a Mott gap in its half-filled $j_{\text{eff}} = \frac{1}{2}$ band. Dispersions, both theoretical and experimental, from [2, 3] are displayed in figure 3.1. The calculation at left uses a local density approximation including Coulomb correlations and spin-orbit coupling (LDA+SOC+U) and show dispersive bands for both

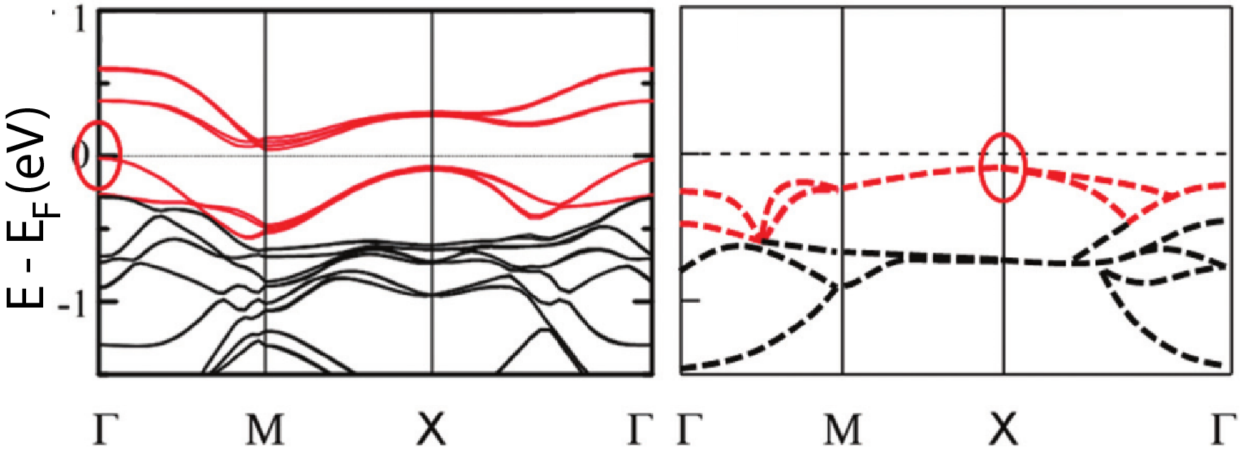

Figure 3.1: Dispersion measured in undoped $Sr_3Ir_2O_7$, from [2]. Left: Theoretical dispersion from an LDA + SOC + U calculation. Right: Experimental dispersions extracted from ARPES data. In each, red bands represent $j_{\text{eff}} = \frac{1}{2}$ bands, black are $j_{\text{eff}} = \frac{3}{2}$ bands.

the half-filled $j_{\text{eff}} = \frac{1}{2}$ band (red) near the Fermi level and the filled $j_{\text{eff}} = \frac{3}{2}$ band (black) at higher binding energy. The right hand panel of the figure is the experimental dispersion in the same work. Bands are colored according to correspondence with the calculations, as ARPES cannot distinguish between $j_{\text{eff}} = \frac{1}{2}$ and $j_{\text{eff}} = \frac{3}{2}$ bands. While the data disagree regarding the energy of the band maximum at Γ they otherwise correspond quite closely. Experimentally, the maximum of the lower Hubbard band is at the X point, and it disperses across the Brillouin zone with a minimum near the M point. Note that this band structure has no Fermi level crossings and thus there is no Fermi surface, in line with its insulating nature. From the calculation we see that the lowest-energy unoccupied states are near the M point.

The addition of electrons in $(Sr_{1-x}La_x)_3Ir_2O_7$ can have one of two basic types of effects, as illustrated in figure 3.2. In the simpler case, akin to simple band insulators and semiconductors, the extra carriers populate the lowest-lying states above the Fermi level. In this case, this is the upper Hubbard band. An alternate case is the introduction of states inside the Mott gap where the strong correlations on the lattice sites relevant to the conduction band localize the extra electrons on the defect/dopant sites. As more carriers are added, the additional charge density will screen the Coulomb repulsion from the singly-occupied sites, and the excitation gap will eventually go to zero and the lower and upper hHubbard band will merge into one filled band. Since ARPES can only observe occupied states, these two scenarios are difficult to distinguish between, especially for small dopant concentratations where the dispersion of the conduction band cannot be determined.

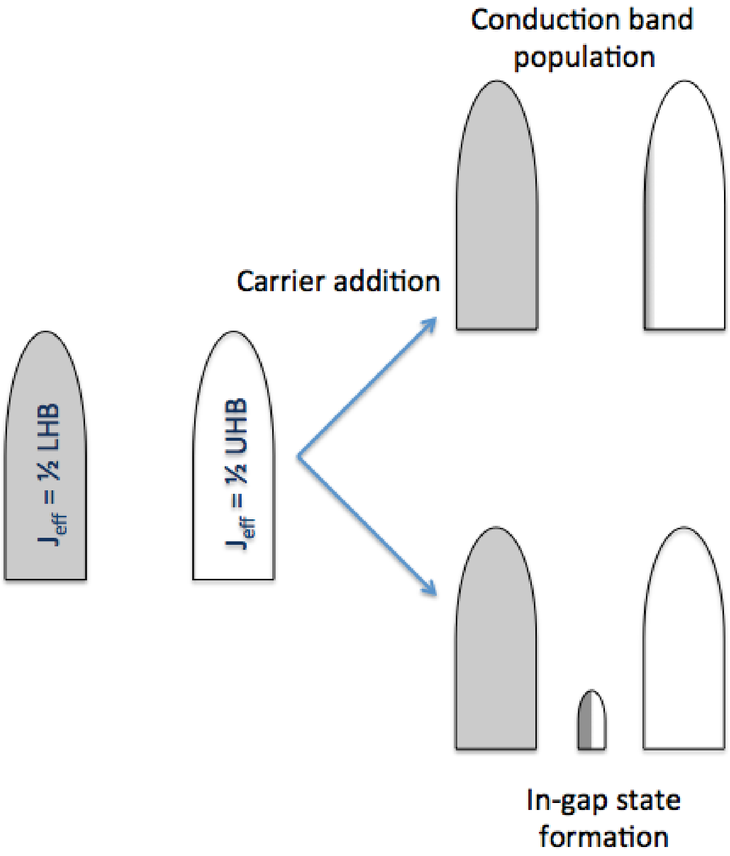

Figure 3.2: Schematic of possible impacts of carrier addition in a half-filled Mott insulator. Added electrons may occupy states in the conduction band (top) or form a state inside the Mott gap (bottom).

3.2 Band structure effects

The Fermi surface of a metallic $(Sr_{0.94}La_{0.06})_3Ir_2O_7$ (x = 6%) sample is shown in figure 3.3. Red/orange regions correspond to regions of high intensity, while blue denotes low intensity. This Fermi surface consists of lens-like pockets on either side of the M point, corresponding to the position of the minimum of the upper Hubbard band from the calculation in figure 3.1.

The low-energy dispersion is seen in the energy-momentum cut in panel along high symmetry directions in the first Brillouin zone. White curves are guides to the eye for the dispersion of the four bands visible in this energy window. The small electron-like bands near the M point give rise to the lens-shaped Fermi surface seen in the Fermi surface. Since in the more heavily doped samples this band crosses the Fermi level, we follow previous ARPES works[73, 74, 75] in referring to it as the "conduction band" independent of its origin. The hole-like band near the X point is identified as the lower Hubbard band, following works on undoped $Sr_3Ir_2O_7$[3, 76]. The band maxima at Γ are commonly attributed to the $J_{\text{eff}} = \frac{3}{2}$ bands[3, 33, 76], and their separation is due to the bilayer splitting present in $Sr_3Ir_2O_7$.

3.2.1 Population and evolution of the conduction band

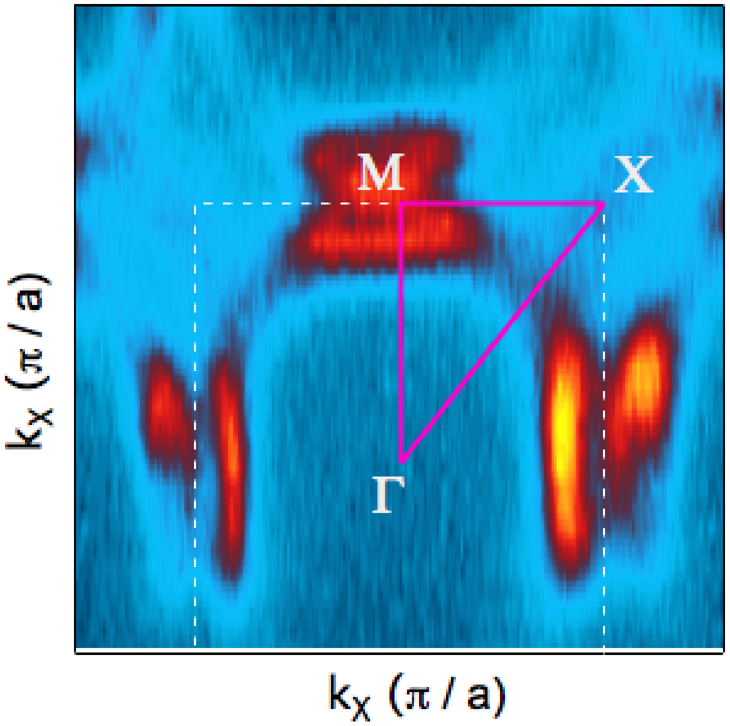

Figure 3.3: Fermi surface of $(Sr_{0.94}La_{0.06})_3Ir_2O_7$. The white dashed square is the boundary of the reduced BZ. (b): Energy-momentum distribution of ARPES intensity along high symmetry directions in the first Brillouin zone. White curves are guides to the eye for the band dispersions.

While the primary change in the Fermi surface with increasing electron concentration is the increasing size of the nearly elliptical Fermi surface pockets in the x = 1% sample, the geometry of these pockets also changes with doping. Notably, in the x = 6% sample, whose Fermi surface is replicated in figure 3.5, there is spectral weight at the Fermi level in a large arc between the pockets not observed in the lower doping levels. This is reflected in the EDCs along this arc-like feature at momentum locations marked by magenta stars in panel a are shown in panels b-d. This arc is manifest by the small peak at E_F for the x = 6%

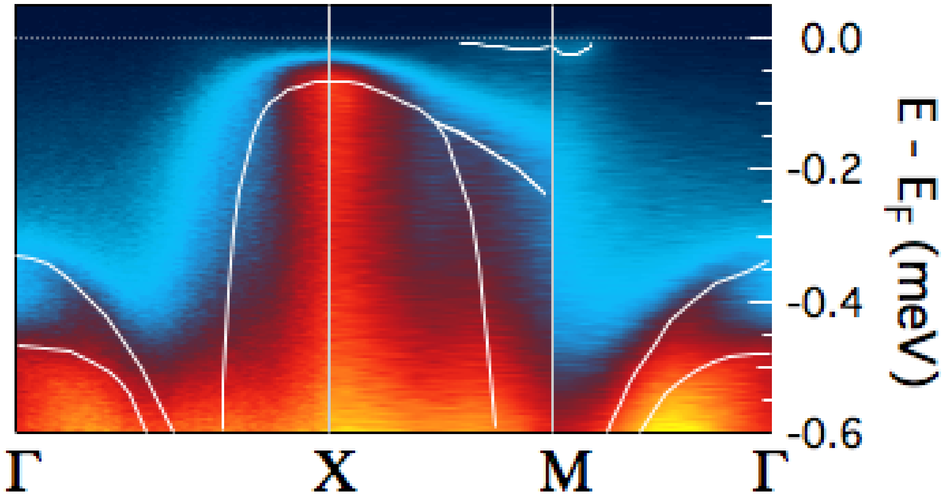

Figure 3.4: Energy-momentum distribution of ARPES intensity along high symmetry directions in the first Brillouin zone. White curves are guides to the eye for the band dispersions.

sample for all momenta observed, and likely corresponds to dispersion of this band slightly above the chemical potential (as suggested in connection to a similar observation in [75]). Indeed, the peak positions are at a lower binding energy nearer the $\Gamma - X$ direction. As expected, no such residual peak is observed in the EDC along the $\Gamma - X$ direction in the x = 1% and x = 3.5% samples.

The width of the electron pocket along its long dimension is extracted from the separation of MDC peaks taken along the k_x direction at the widest part of the pocket, as indicated for the x = 6% sample by the magenta line in panel a of figure 3.6. These MDCs are shown in panel d for the x = 1%, 3.5% and 6% samples. The peak locations, obtained from a fit of two Gaussian peaks and constant background, are marked by magenta squares and grow significantly farther apart with additional doping, as shown by the evolution of the magenta trace in panel g. The width of the pocket along the narrow direction is similarly extracted from MDCs along that direction (k_y for the pocket shown in the figure) and marked by orange circles. In each of these MDCs in panel e, there are three distinct peaks rather than the four that would be expected from the two nearby pockets (one from each band crossing in this direction as shown in panels a and c) due a combination of matrix element effects (like those seen in [74], especially notable in the x = 3.5% sample where the constant energy maps only faintly show one of the two pockets) and the nearness of the two inner Fermi level crossings (especially important in the x = 6% sample). Further, these peaks are difficult to resolve above the noise level in the x = 1%and x = 3.5%samples, making the determination

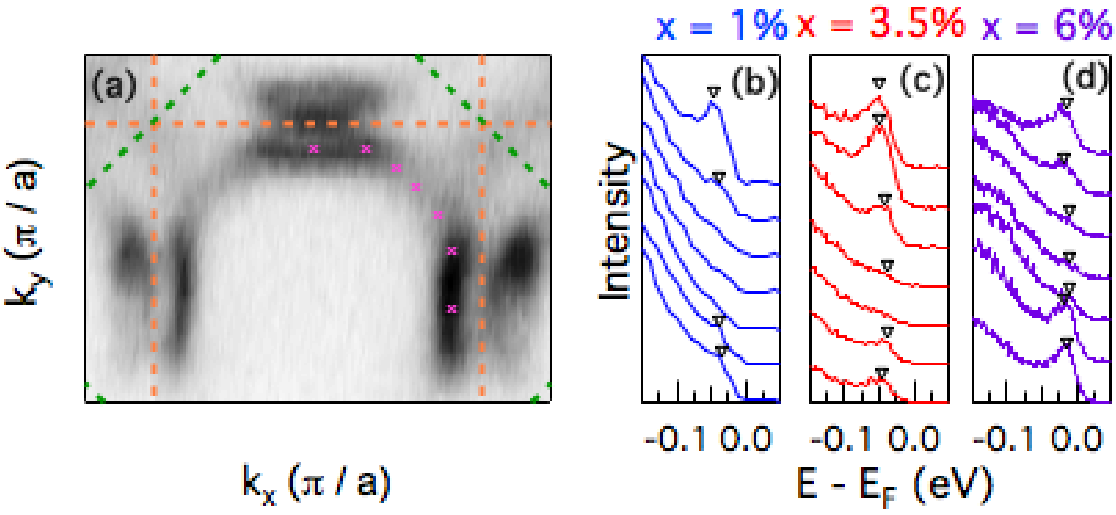

Figure 3.5: Detailed evolution of M point band. (a): Fermi surface of the x = 6% sample in and near the first Brillouin zone. (b),(c),(d): EDCs taken along the arc in the x = 6% Fermi surface for the x = 1%, x = 3.5%, and x = 6% samples, respectively, at momentum locations marked by magenta stars in panel a. (e)-(h): Zoomed in constant energy maps of the electron-like band in the region marked by a yellow rectangle in panel a, from 10 meV above E_F to a binding energy of 40 meV near the band bottom.

of the pocket width difficult. To this end, the error bars reported for this measurement in panel g are set by the width of the overall feature on one side of the Brillouin zone boundary and these less-certain measurements are marked by lighter circles in panel g. This width undergoes a more modest change with doping, increasing from $W_{\text{short}} = 0.04\ \pi/a$ at x = 1% to only $W_{\text{short}} = 0.09\ \pi/a$ at x = 6%.

The band minima for these electron-like bands are offset in momentum from the M point. This offset is not predicted in LDA+SOC+U calculations for the single layer Sr_2IrO_4 compound and thus is likely related to the bilayer splitting in the system. This momentum offset can be measured in the separation between the two band minima along the Γ-M direction, extracted from MDC peak locations at the bottom of the conduction band. The binding energy at which these MDCs are taken is different for each doping, determined from the upturn of the EDC taken at the middle of the Fermi pocket. These MDCs are shown in panel f of figure 3.6 for the three dopings measured here, and the peak locations are marked with green triangles. Contrary to a rigid doping-like picture, the band minima move farther apart with increasing doping.

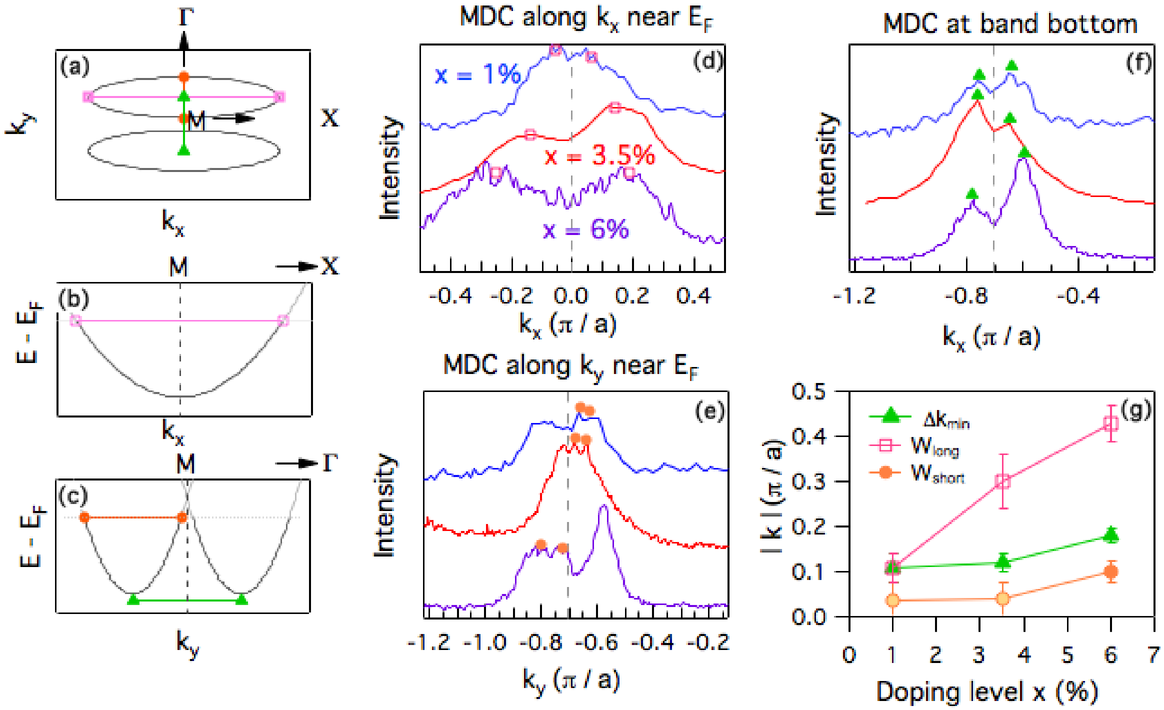

Figure 3.6: Doping evolution of conduction band parameters. (a): Cartoon Fermi surface illustrating the band parameters extracted from MDCs in panels d-f. (b)-(c): Cartoon dispersions along high symmetry directions illustrating the same band parameters. (d): MDCs along the widest part of the Fermi surface pocket for each sample at E_F, with magenta squares marking k_F locations. (e): MDCs along the middle of the Fermi surface pocket in the narrower direction for each sample at E_F, with orange circles marking k_F locations. (f): MDCs along the same direction as in panel f at the binding energy of the minima of the electron-like pockets for each sample, with green triangles marking the momentum location of the band minima. (g): Doping evolution of the Fermi pocket dimensions and separation between band minima.

3.2.2 Effects in the valence band

Figure 3.8 shows constant energy maps of the ARPES intensity from lightly doped (x = 1%) through a doping near the metal-insulator transition (x = 3.5%) to heavily doped (x = 6%) $(Sr_{1-x}La_x)_3Ir_2O_7$ samples. The orange dashed lines represent the boundaries of the surface Brillouin zone in the presence of either AF order or the unit cell doubling generated by the staggered rotation of Ir-O octahedra, while the green dashed lines are the boundaries of the unreduced Brillouin zone. Γ here denotes the momentum coming from normal emission of photoelectrons. Γ' is equivalent to Γ in the reduced Brillouin zone but represents a distinct crystal momentum in the larger zone. The Fermi surface for each is shown in panels (a), (e), and (i) and consists of electron-like pockets near the M point along the boundary of the

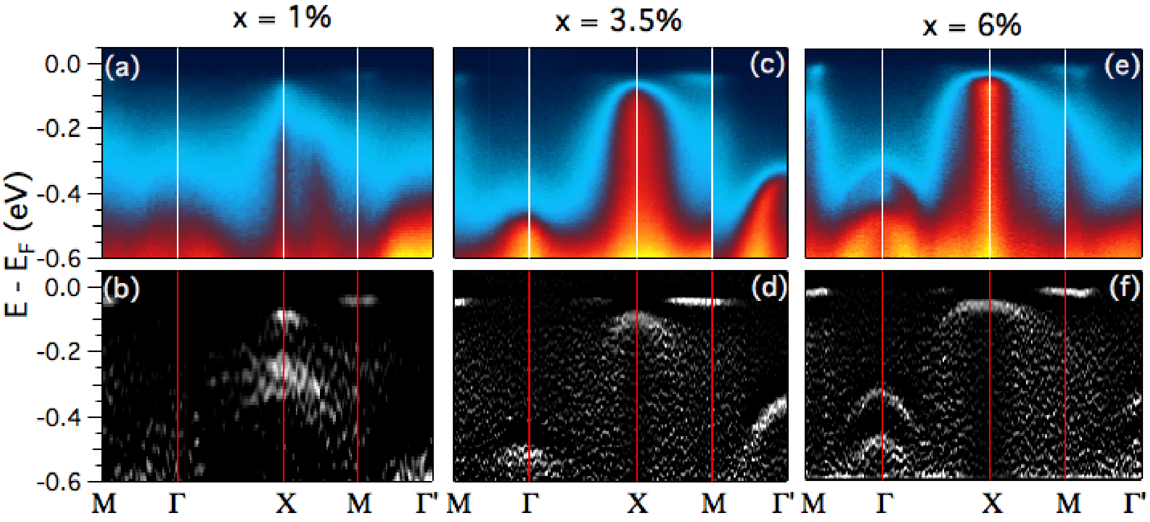

Figure 3.7: Dispersion near the Fermi energy for $(\mathrm{Sr}_{1-x}\mathrm{La}_x)_3\mathrm{Ir}_2\mathrm{O}_7$ samples. (a): Raw ARPES spectrum for the x = 1% sample along a M-Γ-X-M-Γ' path (marked in figure 3.3). (b): Second derivative with respect to energy of (a). (c)-(f): The same as (a) and (b) for the x = 3.5% and x = 6% samples.

reduced Brillouin zone. While these pockets are well separated in the x = 1% sample, the increased pocket size in the x = 6% sample leads to significant deviation from an elliptical shape and hybridization between adjacent pockets near the Γ - X direction as well as along the Brillouin zone boundary. These bands are absent at a binding energy of 200 meV, shown in panels (b), (f), and (j), where the primary spectral weight arises from the $\mathrm{J}_{\mathrm{eff}} = \frac{1}{2}$ lower Hubbard band at the X point. At a binding energy of 400 meV, the $\mathrm{J}_{\mathrm{eff}} = \frac{3}{2}$ bands at Γ/Γ' are visible along with the $\mathrm{J}_{\mathrm{eff}} = \frac{1}{2}$ lower Hubbard band near X. At 600 meV, most bands should be of mostly $\mathrm{J}_{\mathrm{eff}} = \frac{3}{2}$ character, and a large number of band crossings are visible here in the constant energy maps of panels (d), (h), and (l).

While previous ARPES works on $\mathrm{Sr}_3\mathrm{Ir}_2\mathrm{O}_7$ have primarily used the reduced Brillouin zone delineated by the orange boundaries in these figures, two features seemingly align more closely with the green zone boundaries of the unreduced Brillouin zone. The first is the difference between the spectra near the Γ and Γ′ points, especially visible at a binding energy of 400 meV in the x = 3.5% sample in panel g of figure **??** (and to a lesser extent in the x = 6% sample, panel k). In each, a large pocket is observed at Γ′ and only faint spectral weight related to a deeper band maximum is visible at Γ, though this may be related to photoemission matrix element effects at normal emission as seen in undoped $\mathrm{Sr}_3\mathrm{Ir}_2\mathrm{O}_7$ [3]. The second is the elongation of the lower Hubbard band pockets along the $\Gamma' - X$ direction in the x = 1% and x = 3.5% samples and, to a lesser degree along the $\Gamma - X$ direction in the x = 6% sample. In the case of the reduced (orange) Brillouin zone, these pockets

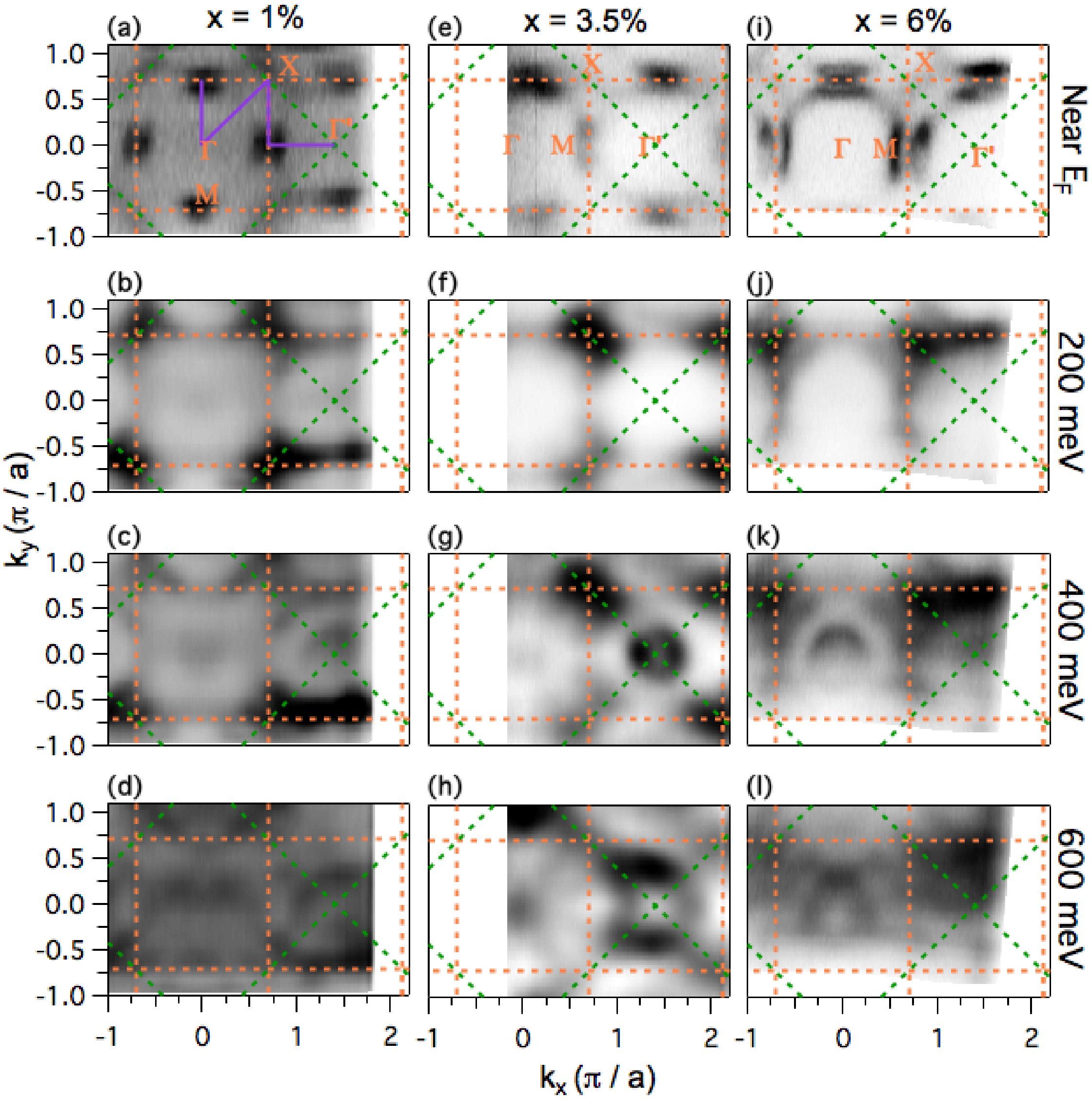

Figure 3.8: Constant energy maps for x = 1% (a - d), x = 3.5% (e - h) and x = 6% (i - l) samples at binding energies from 0 to 600 meV. The orange dashed square represents the Brillouin zone of $Sr_3Ir_2O_7$ while the green dashed squares represent the Brillouin zone when the unit cell doubling due to Ir-O octahedral rotations is ignored.

should have fourfold rotational symmetry about the X point, with the same width along the $\Gamma - X$ and $\Gamma' - X$ directions, while these are not required by the unreduced (green) Brillouin zone. A similar distortion has been noted in undoped $Sr_3Ir_2O_7$ [76, 77], with two distinct explanations that each depend on the incident photon energy. One study suggests that the bonding and antibonding bands have opposite elongations, so that the overall band structure is symmetric under the required rotation, but that a given photon energy will preferentially select one of these bands resulting in the observed elongation. The other explanation of the X point elongation comes from considering a bulk Brillouin zone in which the cross section of the first Brillouin zone at a particular k_z value is not a square. In particular, at $k_z = 0$ the point labeled Γ' here is actually the bulk Z point, and the Brillouin zone boundary is naturally elongated along $\Gamma' - X$. Most published calculations of the band structure of $Sr_3Ir_2O_7$ do not consider this three dimensional zone, and such calculations may be useful to determine the relevance of the bulk Brillouin zone for this system. We further note that there have been recent reports[18] showing broken symmetries in the structure of the Ir-O octahedra such that the correct lattice for $Sr_3Ir_2O_7$ is monoclinic rather than tetragonal, as the square BZ we use here would suggest. The distortions causing the system to depart from tetragonal symmetry are quite small (on the order of 0.1%), and thus should not be clearly visible in the ARPES spectra here.

3.3 Correlation-related changes

3.3.1 Reduction in the Mott gap

The most straightforward manifestation of electron-electron correlations in $Sr_3Ir_2O_7$ is its energy gap (and consequent insulating state). While doping into the conduction band eventually induces a metallic state, the underlying gap between the lower and upper Hubbard bands remains as a signature of the Coulomb correlations in $(Sr_{1-x}La_x)_3Ir_2O_7$. The magnitude of this effect can be extracted from the band structure at each doping level as the energy difference between the maximum of the dispersion of the lower Hubbard band and the minimum of the upper Hubbard band. As previously discussed, there is some ambiguity as to whether the electron-like conduction band at M is the true upper Hubbard band or a state developing in the Mott gap. If it is indeed the upper Hubbard band, the Mott gap is the energy separation between the X point band maximum and the near-M band minimum. In the case of an in-gap band at M, the Mott gap is somewhat larger and not immediately available from APRES spectra, as the upper Hubbard band is unoccupied. We can, however, extract an estimate for the Mott gap by taking the energy separation between the X point band maximum and the chemical potential. This is necessarily a lower bound on the gap for the in-gap state scenario, as the lowest energy for the (unobserved) upper Hubbard band is immediately above the chemical potential. The gap values under each scenario are shown in figure 3.3.1. In panels (a) and (b) are the low-temperature EDCs from the X point and near-M band minimum, respectively, for $x = 1\%, 3.5\%$, and 6%. Triangles mark the fit-extracted peak position, indicative of the energies of the band extrema. Panel (c) shows the Mott gap for each doping, with dark green circles giving the value assuming the M-point band is the upper Hubbard band and light green circles that it is an in-gap state. Green lines provide guides to the eye for the trends of these gap values with doping. In either case, there is a net decrease in the gap magnitude over the doping range studied, with an increase

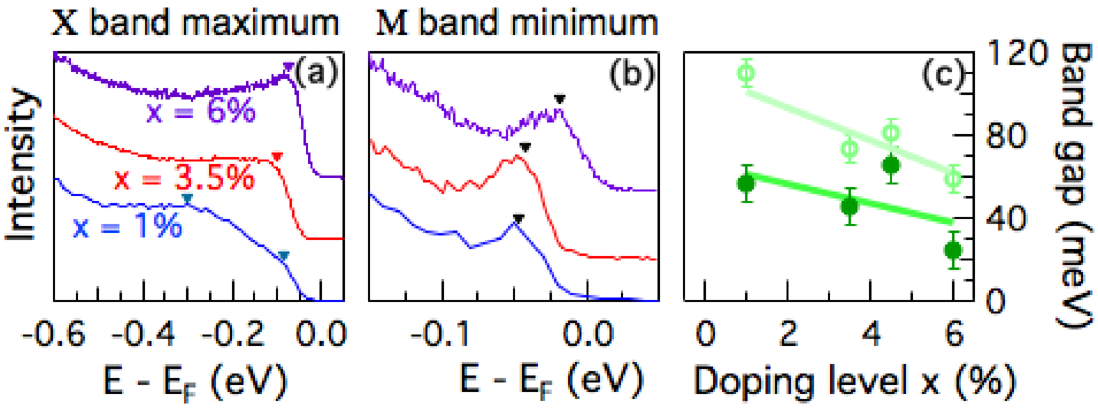

Figure 3.9: Doping dependence of the Mott gap in $(\mathrm{Sr}_{1-x}\mathrm{La}_x)_3\mathrm{Ir}_2\mathrm{O}_7$. (a): EDCs at the X point for $x = 1\%, 3.5\%$, and 6% samples. (b): EDCs at the band minimum near M for $x = 1\%, 3.5\%$, and 6% samples. (c): Extracted Mott gap values by doping using the X point maximum binding energy (light green) and the energy separation between the X point maximum and the near M minimum (dark green).

across the metal-insulator transition between x = 3.5 %and x = 4.5 %. This unexpected increase is well within the error bars for the lower Hubbard band - chemical potential gap, while much larger in the measured gap between the lower Hubbard band and the conduction band. This discrepancy largely comes from the vanishing of a 20 meV spectral weight suppression in the antiferromagnetic samples across the metal-insulator transition, as discussed in section 3.5. This may indicate that the position of the lower Hubbard band is the better indicator of the Mott gap. This is in line with a previous study of $(\mathrm{Sr}_{1-x}\mathrm{La}_x)_3\mathrm{Ir}_2\mathrm{O}_7$, though our gap values are somewhat lower than those reported in that work[74]. The major part of this discrepancy is due to observation of the two bands at the X point. In that work, the lower binding energy band is not observed in samples below a doping level of x = 5%. Both works agree that the gap remains open to high doping levels ($x \geq 6\%$), in contrast to the single-layer $\mathrm{Sr}_2\mathrm{IrO}_4$ where the Mott gap collapses abruptly [78].

3.3.2 Enhancement of band masses

The evolution of the effective mass in the lower Hubbard band and conduction band with doping is illustrated in figure ??. Band dispersions are determined by taking EDCs at each of several momentum points along a line in the Brillouin zone, and extracting a characteristic energy for each. As the lower Hubbard band lacks a clear peak feature in the x = 1% and x = 3.5% samples, the leading edge midpoint was taken as the band position, as shown in panels (a) - (c). Similar EDC stacks for the conduction band are shown in panels (f) - (h), where a peak position can be fit. Panels (d) and (i) show these extracted dispersions for each doping

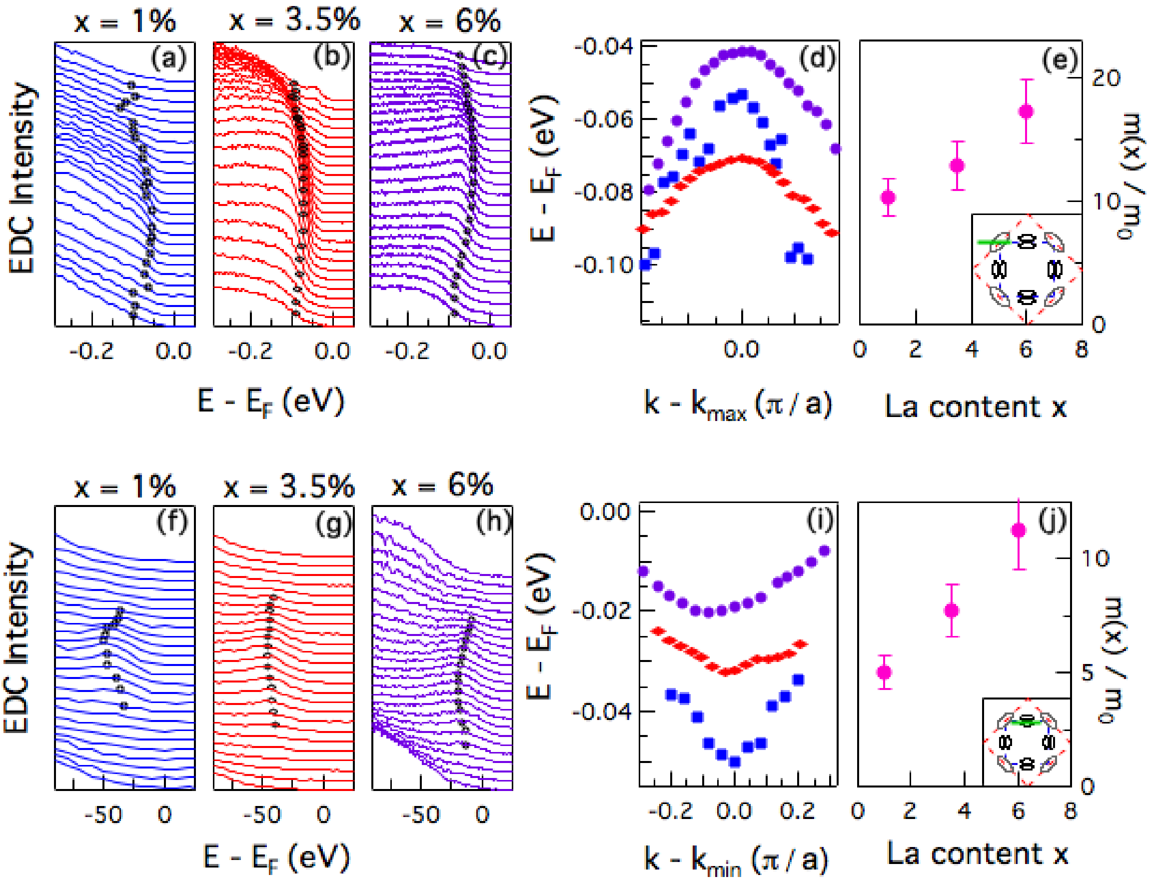

Figure 3.10: Effective masses of near-E_F bands. (a), (b), (c): EDCs taken at momentum positions along the M-X direction (marked in inset to panel (e)) in the x = 1%, 3.5%, and 6% samples. (d) Dispersions for the lower Hubbard band extracted from the EDC fits in (a) - (c). (e): Effective masses in $(\mathrm{Sr}_{1-x}\mathrm{La}_x)_3\mathrm{Ir}_2\mathrm{O}_7$ as a function of doping from the fits to dispersion. (f) - (j): The same as (a) - (e), for the conduction band rather than the lower Hubbard band.

level, which are then fit near the band extremum with a quadratic band in which the effective mass is a parameter. These extracted masses are plotted in panels (e) and (j) as magenta circles, normalized by the free electron mass m_0. Error bars are derived from statistical errors in the quadratic fits, combined with the variation in mass parameter acquired from shifting the fitting range near the extremum, accounting for both the noise in band positions and asymmetry apparent in the bands. The absolute values of these band masses are similar to those reported in some systems of doped SrTiO_3[79]. Both bands display a similar increase of a factor of 2.5 between the x = 1% and x ≈ 8% samples, evolving smoothly across the metal-insulator transition near x = 4%. The high effective mass in metallic samples is in rough agreement with, though somewhat higher than, values from a recent work in which the mass enhancement is indirectly measured using infrared spectroscopy[80].

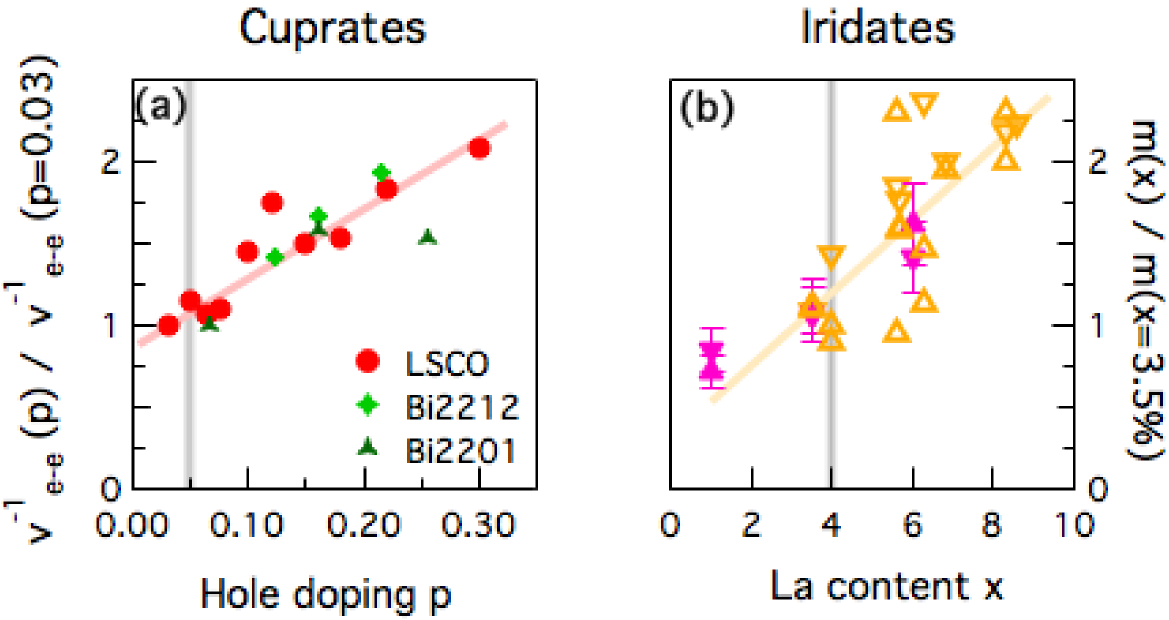

Figure 3.11: Doping dependence of band renormalization in cuprates and iridates. (a): Doping dependence of band renormalization in $La_{2-x}Sr_xCuO_4$ (LSCO, red circles) $Bi_2Sr_2CaCu_2O_{8+\delta}$(Bi2212, light green diamonds) and $Bi_2Sr_2CuO_{4+\delta}$ (Bi2201, dark green triangles) from [81]. (b): doping dependence of effective mass in lower Hubbard band (downward pointing triangles) and conduction band (upward pointing triangles) in $(Sr_{1-x}La_x)_3Ir_2O_7$, from figure 3.10.

Figure 3.11 compares the doping dependent effective mass of the conduction band and lower Hubbard band of $(Sr_{1-x}La_x)_3Ir_2O_7$ with phenomena observed in cuprate superconductors, shown in figure panel (a). Since the bands in the cuprates are approximately half filled, the mass renormalization is extracted from linear fits to the dispersion near the chemical potential crossing rather than parabolic fits near band extrema as was done in $Sr_3Ir_2O_7$. Filled symbols correspond to the ratio of band velocities measured at binding energies $E_B \geq 100$ meV for three families of cuprate superconductors. This energy range is chosen to exclude explicit renormalization effects from electron-boson coupling which only impact states within an energy window of $E_b \approx \hbar\omega$ of the Fermi level. For all three cuprate families, the inverse band velocity, and thus the effective mass, increase with doping at roughly the same rate. This is in line with the observed change in effective mass in $(Sr_{1-x}La_x)_3Ir_2O_7$, suggesting a connection between the change in effective mass with doping observed in the iridates to this high-energy renormalization observed in cuprates. In cuprates, this slope change has been associated with a “high energy anomaly” wherein the band velocity drastically changes at an energy between 0.3 and 0.5 eV[82, 83]. A similar anomaly is present at high energy (near

1 eV) in Sr_2IrO_4[84], though no such feature has been reported in $Sr_3Ir_2O_7$. In studies with data at sufficiently high binding energy [3, 76] the ARPES spectra become broad near 1 eV, making the detailed study of dispersions at this binding energy difficult. This type of feature is thought to be a manifestation of strong correlations, though its doping dependence does run counter to the basic picture of mass increasing with strengthening correlations[82, 85].

3.4 Effects of spin-orbit coupling and bilayer splitting

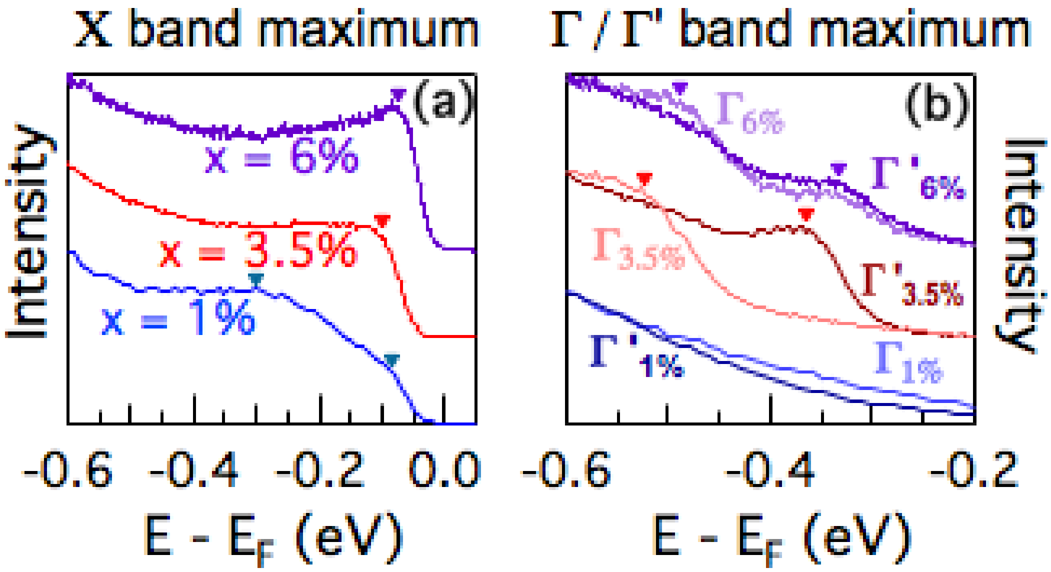

Figure 3.12: X and Γ band extrema locations in $(Sr_{1-x}La_x)_3Ir_2O_7$. (a): EDCs at the X point through the maximum of the lower Hubbard band for the x = 1%, x = 3.5 %, and x = 6% samples, with triangles marking the extracted feature locations. (b): EDCs at the Γ and Γ' points for the same samples.

The evolution of band separations can be most easily quantified via the analysis of energy distribution curves (EDCs) as in figure 3.12. In panels (a) and (b), we show the EDCs corresponding to the band maxima at X and Γ/Γ', respectively, for each doping level measured here. From the EDCs taken at the X point in each sample (panel a), it appears that there is a transfer of spectral weight from the 300 meV feature to the 100 meV feature with increasing doping. There are two clearly visible distinct features in the x = 1% spectrum, a flat spectrum with a leading edge near 100 meV in the x = 3.5% measurement, and a more pronounced peak near 100 meV in the x = 6% sample. The peak at higher binding energy more closely matches the lower Hubbard band position in undoped $Sr_3Ir_2O_7$, especially considering the downward shift due to the introduction of electrons. This crossover from a high-energy feature to a low-energy feature at X, which has been observed in a previous ARPES study of $(\mathrm{Sr}_{1-x}\mathrm{La}_x)_3\mathrm{Ir}_2\mathrm{O}_7$[74] (though at a different doping level), may be due either to the formation of an in-gap state or due to inhomogeneity in the doping level within the measured area. STM measurements of lightly doped $(\mathrm{Sr}_{1-x}\mathrm{La}_x)_3\mathrm{Ir}_2\mathrm{O}_7$ have revealed metallic regions within tens of nanometers of regions with a density of states that is fully gapped, well within the size of the beam spot used here[86, 57]. This sample-dependent coexistence of metallic and insulating regions could explain the different doping level at which this spectral weight transfer occurs between the present study and the literature (in a previous study[74], this crossover is observed near a doping level of x = 4%). As previously discussed, the separation between the two bands at the Γ point (or the band at Γ and the band at Γ' in the case of the x = 3.5% sample) is related to the bilayer splitting in the system. Published studies of the x = 0% compound show a splitting of 180 meV between these bands[3, 76], while the splitting in both the x = 3.5% and x = 6% samples is 158 and 157 meV, respectively. The EDCs at the Γ and Γ' points in the x = 1% sample do not show clear peaks corresponding to these bands, and thus it is difficult to extract a precise value of this splitting. The difference between literature values for undoped $\mathrm{Sr}_3\mathrm{Ir}_2\mathrm{O}_7$ and the doped samples here appears significant (though different handling of the spectral background in the literature may play a role), but no significant change is observed across the metal-insulator transition. Finally, the splitting between the bands at X ($\mathrm{J}_{\mathrm{eff}} = \frac{1}{2}$) and Γ/Γ' ($\mathrm{J}_{\mathrm{eff}} = \frac{3}{2}$) is ≈ 255 meV in the x = 6% sample and ≈ 265 meV in the x = 3.5% sample, indicating a highly similar but potentially weaker effect of spin-orbit coupling with increased doping.

3.5 Low energy spectral weight suppression

In addition to straightforward shifts of the band positions and dispersions with doping, lightly doped $\mathrm{Sr}_3\mathrm{Ir}_2\mathrm{O}_7$ populates a conduction band that does not reach the chemical potential– rather, spectral weight at low energies is suppressed. This suppression of spectral weight, together with the lack of back bending at E_F and the shape of the symmetrized EDCs resembles the pseudogap feature observed in other correlated materials[87, 88, 89]. In this section the doping, temperature, and momentum dependence of this spectral weight suppression are explored, revealing close ties to the antiferromagnetic insulating ground state.

3.5.1 Doping dependence

The spectral weight suppression (SWS) is identified by its behavior in the conduction band of $(\mathrm{Sr}_{1-x}\mathrm{La}_x)_3\mathrm{Ir}_2\mathrm{O}_7$, as seen in figure 3.13. The effect is most prominent in the x = 1% sample as shown in panel b, where the cut is taken along the widest part of the electron-like pockets (black arrow in panel a). The band is well removed from the chemical potential in both this sample and in the x = 3.5% sample (data in panel c), where some dispersion is becoming evident but clearly stops short of E_F. As the doping increases to 4.5% and 6%, no suppression of spectral weight is observed and the band crosses the chemical potential.

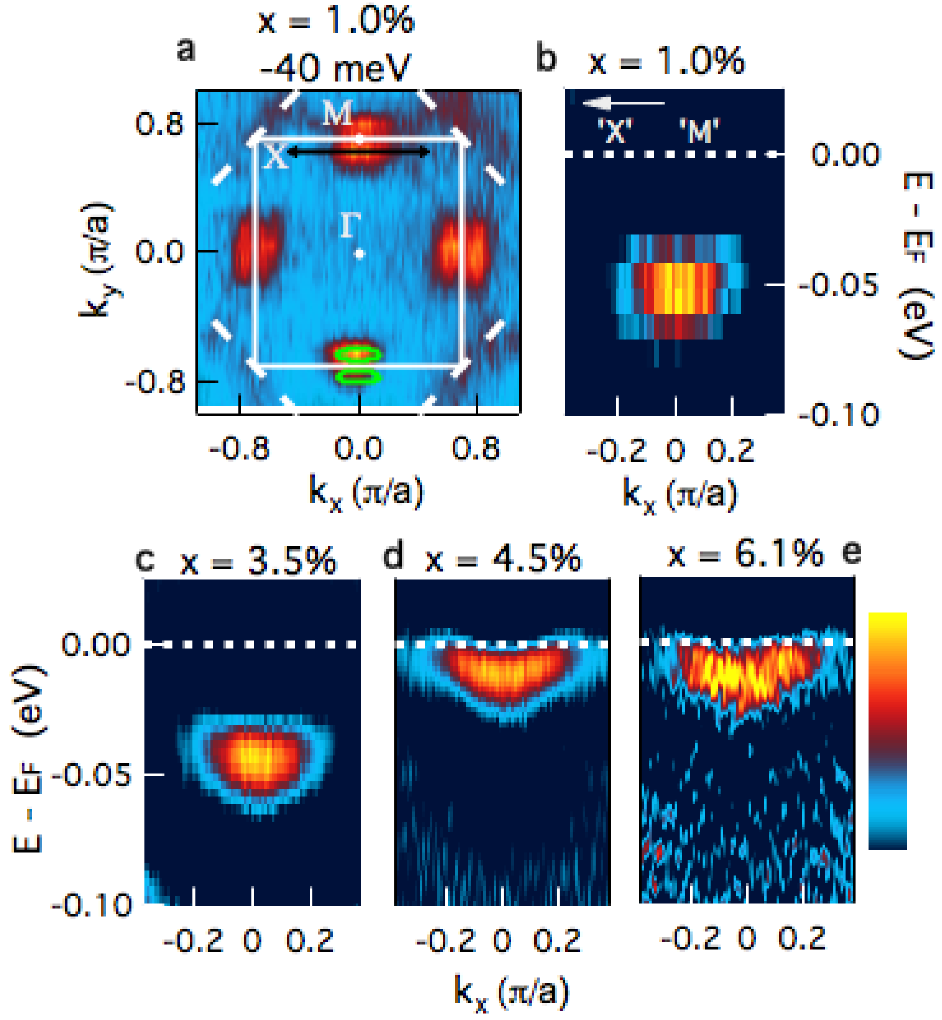

Figure 3.13: Conduction band dispersions in $(\mathrm{Sr}_{1-x}\mathrm{La}_x)_3\mathrm{Ir}_2\mathrm{O}_7$. (a): Constant energy map in an x = 1% sample at 40 meV below the Fermi level, showing the cut location for subsequent panels with a black arrow. (b): Second derivative with respect to energy of the energy-momentum cut along the M-X direction in an x = 1% sample. (c)-(e): Same as (b) for a x = 3.5%, 4.5%, and 6% sample, respectively

While the occupied bandwidth of this conduction band increases with doping as expected, the band bottom moves toward the chemical potential with doping from x = 1% until x = 4.5% as the energy scale of the spectral weight suppression decreases more quickly than the chemical potential shift induced by doping.

In order to investigate the origin of this suppression, we studied its evolution with both temperature and doping across the reported metal-insulator transition. In figure 3.14, we

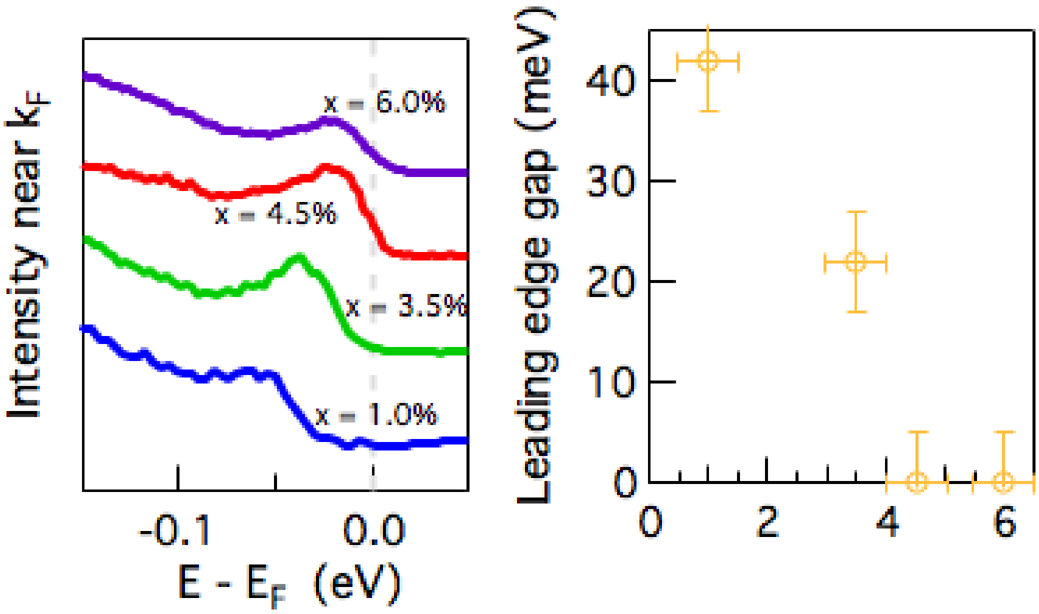

Figure 3.14: Doping dependence of the spectral weight suppression at low temperature. Left: EDCs near k_F for each doping level measured. Right: Extracted leading edge gap as a function of doping

plot EDCs integrated over a small angular range near k_F (±0.05°) along the $\Gamma - M$ direction as a function of doping. For the x = 1% and 3.5%, samples where there is no spectral weight at the chemical potential, we used a momentum corresponding to the MDC peak at the lowest binding energy for which such peaks were distinguishable. The left panel shows the low-temperature (15-20 K) EDCs for each doping. Consistent with our observations from the energy-momentum second derivative plots, there is a gap between the leading edge of the EDC and E_F in the x=1% and x=3.5% samples, while the spectral weight crosses the chemical potential in the x=4.5% and x=6% samples. By fitting the leading edge of these integrated EDCs we extract a gap value of 42 meV for the x = 1% sample and of 21 meV for the x = 3.5% sample, while there is no gap in the other two samples.

3.5.2 Temperature dependence

In figure 3.15 we show the temperature dependence of the integrated EDCs for the x = 1% sample. In the low-temperature regime, a relatively sharp quasiparticle peak is present at energies near 50 meV with a narrow leading edge. As the temperature further increases, the leading edge appears to shift closer to the Fermi level, followed by a decrease of the quasiparticle peak. Panel b depicts the gap value extracted from this leading edge method

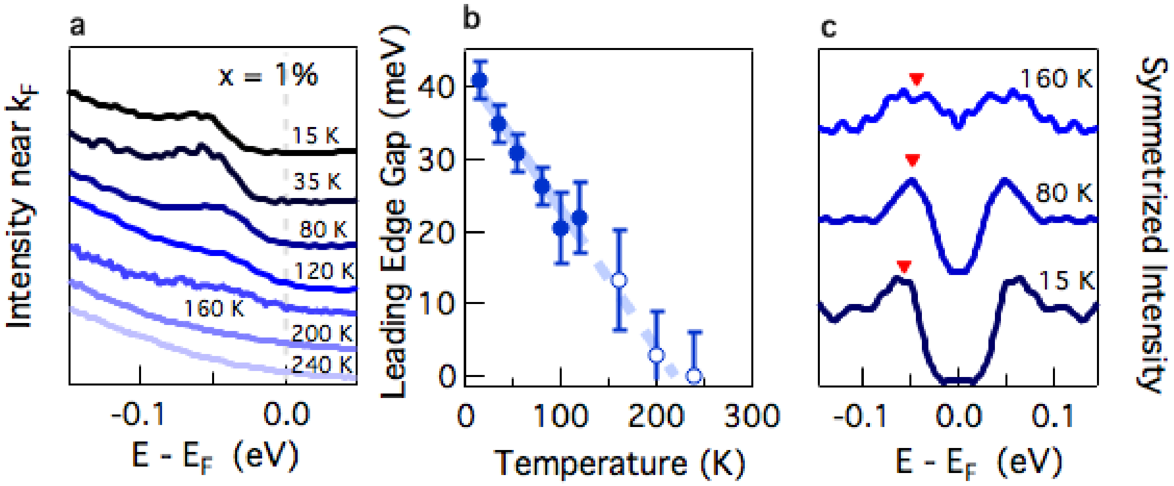

Figure 3.15: Temperature dependence of the observed spectral weight suppression (a): Temperature dependence of the same integrated EDCs in an x=1% sample. EDCs are normalized by their value at -150 meV for clarity. (b) Temperature dependence of the leading-edge gap value extracted from integrated EDCs in (a). (c) Symmetrized EDCs for selected temperatures in the x = 1 % sample showing the evolution of the quasiparticle peak position for each temperature. In each, a smooth background fit for -0.15 eV $\leq$ E $\leq$ -0.1 eV was subtracted. Red triangles mark approximate peak positions, determined from the second derivative.

for each temperature, which appears to fall off approximately linearly with temperature to a closure around the Neel temperature at 240 K. This method is less reliable at higher temperatures where the peak is less well defined, particularly at and above 160 K, where open symbols and a dashed guide to the eye are used to indicate this uncertainty. An alternative method for examining the temperature dependence of the gap is the use of symmetrized EDCs, like those shown in panel c. In the approximation of particle-hole symmetry, this symmetrization removes the effect of the Fermi-Dirac distribution on the lineshape, which can be of particular importance with small gaps and at higher temperatures. In the 15 K and 80 K data, we can see that the peak corresponding to the conduction band (marked with a red triangle) remains well-defined, with a slight shift and broadening between these two temperatures. A major effect of increasing temperature appears to be the filling of the gap, reminiscent of the pseudogap behavior in cuprate superconductors[90, 91]. The EDCs measured at 200 K and 240 K are nearly featureless when symmetrized, a signature of the gap “filling in” with additional spectral weight near E_F.

One potential spurious effect that would mimic the spectral weight suppression observed here is sample charging: in insulating samples, the photoemission process leaves a net positive charge on the sample which exerts an attractive force on subsequent bunches of photoelectrons,lowering their kinetic energy. While this would result in superficially similar experimental phenomenology, including the decreasing change in the band maximum position with higher temperatures and dopings, it would depend upon photon flux and affect all bands within a single measurement equally. While we did not perform a thorough photon flux dependence, we do observe a difference in the thermal shift of band positions between the M point band and a deeper valence band at Γ in an x = 3.5% sample, as shown in figure **??** In panel a we show the change in EDCs between 20 K and 100 K for this deeper valence band, showing a shift of less than 9 meV in the leading edge position, which sets an upper bound for the change in any sample charging voltage between those two measurements. In contrast we have the EDCs for the near-M band in panel b, which show a change of approximately 18 meV between those two measurements, clearly above the magnitude that might be explained by charging.

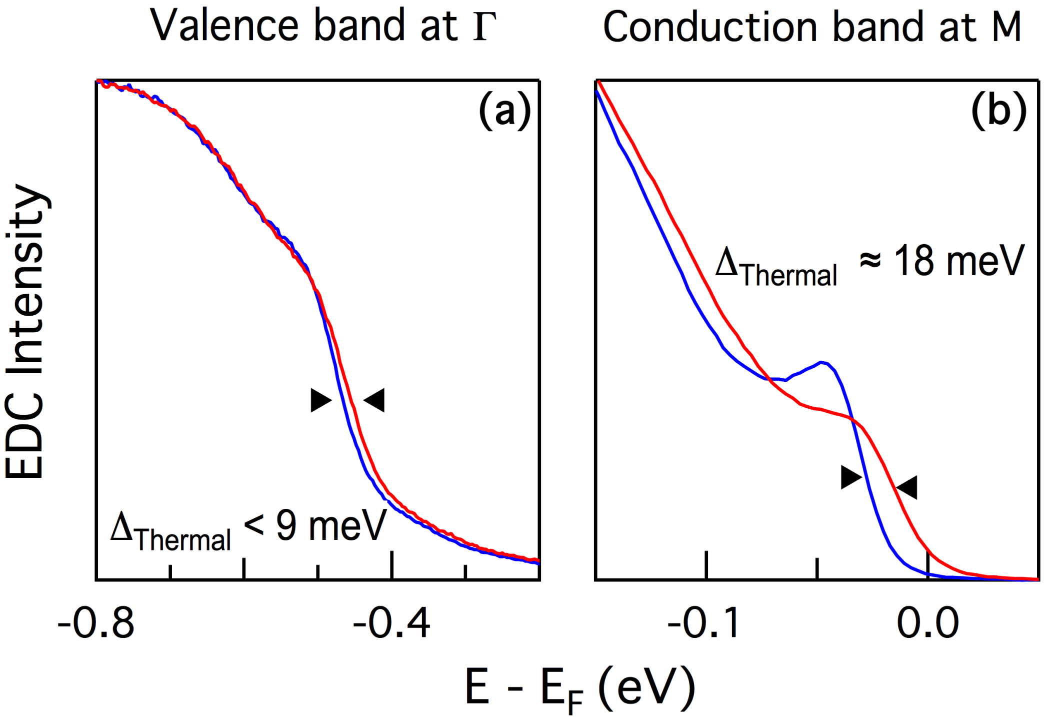

Figure 3.16: Thermal shifts of band features in $(Sr_{1-x}La_x)_3Ir_2O_7$. Left: shift in the valence band maximum at the Γ point corresponding to warming from 20 K to 100 K in an x = 3.5% sample. Right: corresponding shift in the EDC at k_F for the conduction band.

3.5.3 Momentum dependence

The momentum dependence of gaps is of critical importance to theoretical efforts to understand them. In cuprates, the superconducting gap is defined by its *d*-wave nature, and the momentum anisotropy of the pseudogap is key to interpretations of its origin–similarity to the symmetry of the superconducting gap lends credibility to Cooper pairing origins, and the proximity to so-called nesting vectors at which charge density wave order might be favorable suggest that as a possible source of the pseudogap. While the 'gapped' pocket in the present case is a much smaller portion of the Brillouin zone, looking at the SWS as a function of momentum should constrain its possible origins. Data to this effect are shown in figure 3.17, and appear to suggest an isotropic SWS. The left panel shows the near-E_F constant energy map in an x = 1% sample with six momentum locations around the edge of the electron-like pocket. EDCs corresponding to these momentum locations are shown in the panel at right. The leading edge gap in each is well within the error bars on such a measurement, suggesting a SWS that does not depend strongly on momentum. This does not, however, rule out (momentum-dependent) density wave orders as an origin, as the entire 'Fermi surface' is very nearly nested by vectors near the AF ordering vector.

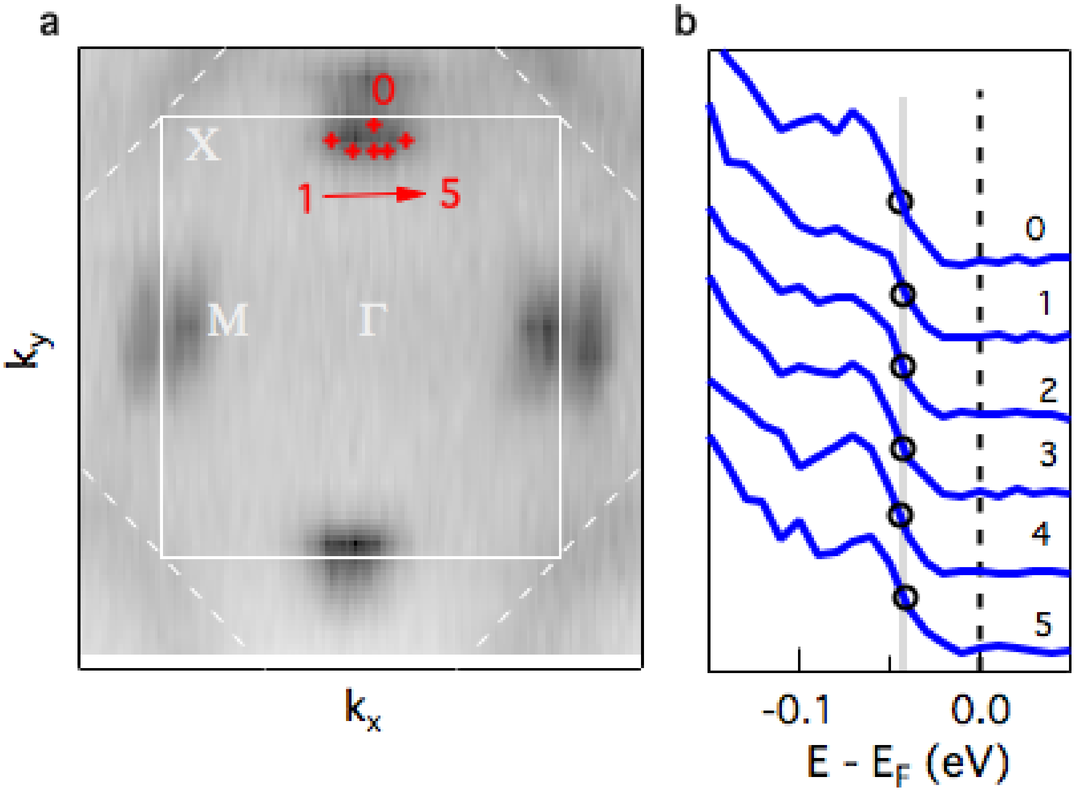

Figure 3.17: Momentum dependence of the observed spectral weight suppression

3.6 Temperature-dependent coherence loss

A further examination of the EDCs as a function of temperature reveals another interesting property of these data: the well-defined coherent peak observed at low temperature for the conduction band has a peculiar dependence on temperature and doping. Specifically, the peak area remains constant across the low-temperature region then diminishes rapidly across a narrow temperature range. This evolution of the quasiparticle peak is depicted in figure 3.18 for the x = 1%, 3.5%, and 6% samples. To extract the quasiparticle weight (corresponding to the grey areas in panel a) for each EDC, we fit a background function consisting of a Fermi-Dirac distribution paired with a linear density of states to the energy regions away from the peak (e.g., from -0.2 to -0.1 eV and 0.01 eV to 0.05 eV). Subtracting this background from the integrated EDC isolates the peak, whose integral is taken as a measure of the quasiparticle weight. Panels d-f display the evolution of this peak area with respect to temperature for each measured doping. The curves are guides to the eye. We observe a reduction of nearly 50% over a temperature range of approximately 40 K in each of these samples and find that the transition temperature increases monotonically with doping.

In order to rule out sample aging as a possible origin for the observed loss of coherence, we present a set of EDCs measured on an x = 1% sample, from a measurement in which the temperature was cycled from 15 K up to 120 K and then returned to 15 K. The results of this measurement are shown in figure 3.19. At left are the EDCs for the initial 15 K measurement, the intermediate 120 K measurement, and the subsequent measurement at 15 K. As expected, there is some change to the background between the two low temperature measurements, and an apparent downward shift of the leading edge due to inelastic scattering. To better analyze the behavior of the coherent peak, the background-subtracted EDCs are shown at right. In these, we see the two 15 K measurements are nearly identical, with a significantly smaller peak in the 120 K data. If aging were the origin of the coherence loss, the blue aged 15 K EDC should be even smaller than the one at 120 K, as the cooling process causes additional adsorbates to stick to the sample at low temperature after the pressure increases with raising the temperature.

This loss of coherence is similar to that previously observed in the related manganite $La_{1.2}Sr_{1.8}Mn_2O_7$ (LSMO). In this system, a coherent quasiparticle is observed near the Fermi level at low temperatures and undergoes a rapid decrease in weight over a narrow temperature range and eventually disappears at the ferromagnetic metal to paramagnetic insulator transition temperature. The low-temperature coherence is attributed to a condensed polaron state[87], though a later work questions this interpretation[92]. This polaron condensation is suggested as a mechanism for the stabilization of the metallic state. Similar physics may be present in the presently-studied compound where both the sharpness of the coherent peak and the coherence loss temperature increase in the metallic regime, suggesting a connection between the low-temperature coherence and the formation of the metallic state. Indeed, polaronic physics have been suggested in undoped $Sr_3Ir_2O_7$ by a recent ARPES study[93] and have been suggested to explain other signatures in layered perovskite iridates [51], including the destruction of the magnetic state at temperatures much smaller than the magnon gap

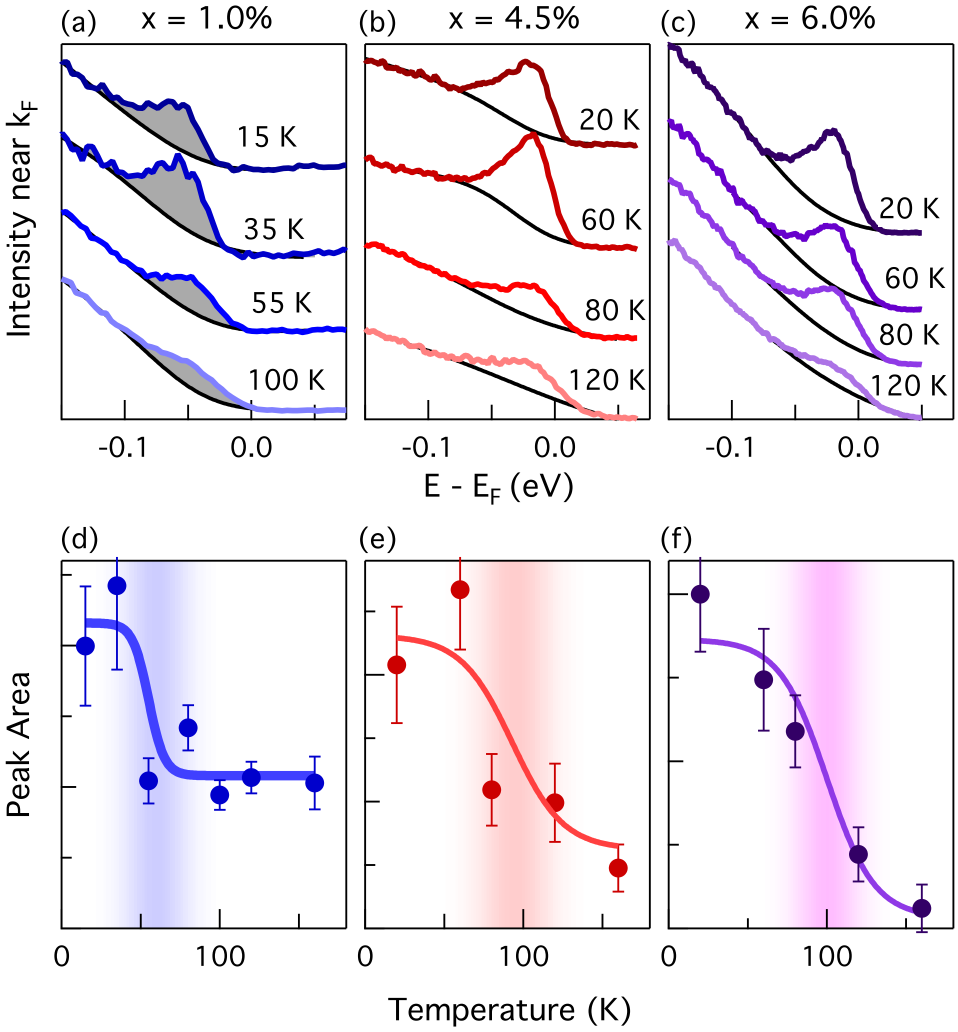

Figure 3.18: Temperature dependent coherence loss in $(\mathrm{Sr}_{1-x}\mathrm{La}_x)_3\mathrm{Ir}_2\mathrm{O}_7$. (a): EDcs at k_F near the M point for the $x = 1\%$ sample at range of temperatures. Black curves are a smooth background fit outside the peak region, and the shaded area is taken as a measure of quasiparticle weight. (b), (c): The same as (a) for $x = 4.5\%, 6\%$, respectively. (d)-(f): Background-subtracted peak area as a function of temperature for each doping measured.

temperature in $\mathrm{Sr}_3\mathrm{Ir}_2\mathrm{O}_7$. Alternatively, the loss of coherence may be related to that observed in the layered cobaltates $(\mathrm{Bi}_{0.5}\mathrm{Pb}_{0.5})_2\mathrm{Ba}_3\mathrm{Co}_2\mathrm{O}_y$ and $\mathrm{NaCo}_2\mathrm{O}_4$[88], where such a loss is attributed to a crossover in dimensionality as c-axis transport becomes incoherent. The lower resistivity anisotropy in $\mathrm{Sr}_3\mathrm{Ir}_2\mathrm{O}_7$ relative to the cobaltates, however, suggests that this is an unlikely explanation for the coherence loss as such a transition would likely occur at significantly higher temperature.

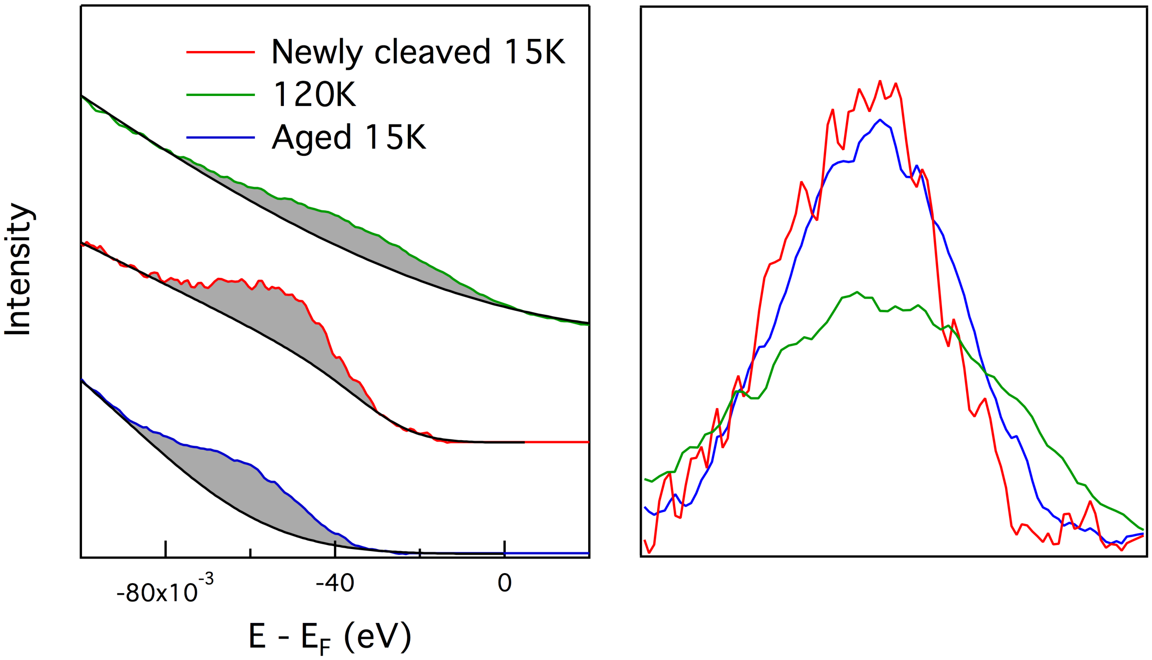

Figure 3.19: Doping and temperature dependence of coherent peak. (a) - (c) Integrated EDCs at M for various temperatures for x = 1%, 4.5%, and 6% samples with background fits (black traces) and extracted peak areas. (d) - (f) Temperature evolution of the background-subtracted peak area for x = 1%, 4.5%, and 6% samples, respectively.

3.7 Electronic phase diagram

To summarize the data, we compare the phase diagram as determined via ARPES to that from a recent scattering, transport, and magnetization study[57] on the same system in figure 3.20. The doping and temperature dependence of the spectral weight suppression suggests an identification of this feature with the magnetic ordering along (π, π) observed via X-ray scattering[94, 57]. We note also that the drastic change in the gap magnitude over the short doping range from x = 3.5% to x = 4.5% is consistent with the reported first-order melting of the antiferromagnetic state[57]. The doping dependence of the coherence-loss temperature for the conduction band suggests that it may be connected to the onset of the metallic state with doping. It is unlikely to be connected to the structural transition reported from scattering[57] as the structural transition temperature is significantly higher in the fully metallic samples where both are observed.

This phase diagram highlights several of the ways in which $(\mathrm{Sr}_{1-x}\mathrm{La}_x)_3\mathrm{Ir}_2\mathrm{O}_7$ and its spectral weight suppression are similar to other Mott systems, including $\mathrm{Sr}_2\mathrm{IrO}_4$. In both cases, a low-doping state marked by the absence of quasiparticles near the chemical potential emerges near the antiferromagnetic Mott state and then vanishes with further doping.

While the spectral weight suppression appears to be linked to the antiferromagnetic state in $(\mathrm{Sr}_{1-x}\mathrm{La}_x)_3\mathrm{Ir}_2\mathrm{O}_7$, further work is required to identify a microscopic mechanism giving rise to the suppression. No clear identification exists in pseudogapped systems as magnetism, superconductivity, and charge density waves, among other phenomena, provide possible and contested origins of the pseudogap [95, 89]. In fact, the role of magnetism in the cuprate pseudogap is called into question by a similar gap magnitude in nickelates with much weaker magnetism[96]. The apparent lack of momentum dependence in the spectral weight suppression differs from the highly anisotropic pseudogap, though the smaller size of the Fermi surface limits a full exploration of the momentum dependence.This may be due to different nesting conditions provided by the Fermi surface geometry, as the entire M-point pocket in $(\mathrm{Sr}_{1-x}\mathrm{La}_x)_3\mathrm{Ir}_2\mathrm{O}_7$ is nearly nested by a vector near (π, π) while pseudogapped systems are nested only near the antinodal direction. Further, this low-doping state gives way to a metallic region with signatures of another ordering; in $(\mathrm{Sr}_{1-x}\mathrm{La}_x)_3\mathrm{Ir}_2\mathrm{O}_7$ this is marked by the coherence loss transition instead of superconductivity. Lastly, we note the different band signatures of the metal-insulator transition: in $(\mathrm{Sr}_{1-x}\mathrm{La}_x)_3\mathrm{Ir}_2\mathrm{O}_7$ metallicity is reached when the spectral weight suppression decreases to zero energy leaving small electron-like Fermi surface pockets while in $(\mathrm{Sr}_{1-x}\mathrm{La}_x)_2\mathrm{IrO}_4$ the Mott gap collapses at low doping and a large hole-like Fermi surface emerges [78, 97].

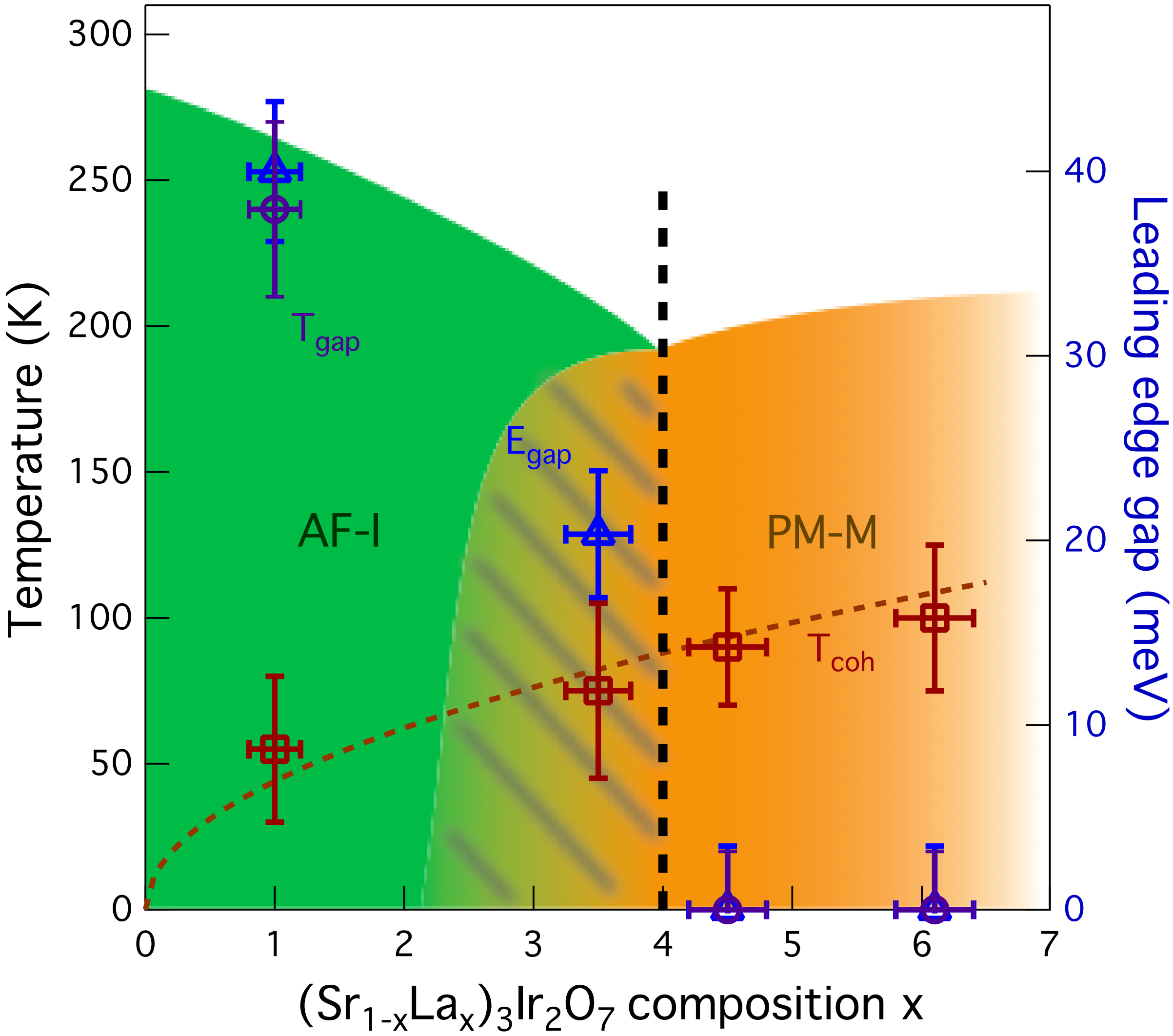

Figure 3.20: Phase diagram of $(Sr_{1-x}La_x)_3Ir_2O_7$. T_{gap} is the temperature at which the leading edge gap appears to vanish. E_{gap} denotes the leading edge gap magnitude in the lowest temperature measurement. T_{coh} denotes the characteristic temperature associated with the loss in coherent spectral weight as discussed in section 3.5 . AF-I and PM-M regions are taken from a recent scattering-based study[57]

Chapter 4

Spin-polarized photoemission from $(\mathbf{Sr}_{1-x}\mathbf{La}_x)_3\mathbf{Ir}_2\mathbf{O}_7$

This chapter describes results of spin-resolved ARPES measurements conducted on doped samples of $(Sr_{1-x}La_x)_3Ir_2O_7$. While traditional spin-integrated ARPES has provided significant insight into the role of electron correlations, collective excitations, and doping effects in $(Sr_{1-x}La_x)_3Ir_2O_7$, the only signature of spin-orbit coupling in the previous chapter was a small possible shift in band splittings between the $j_{\text{eff}} = \frac{1}{2}$ and $j_{\text{eff}} = \frac{3}{2}$ states. Spin-resolved ARPES, however, has been instrumental in studying spin-orbit effects in the broken-symmetry states discussed in chapter 1, including the surface[98, 99] and bulk[100] Rashba effect. Importantly, it is also the main mechanism for experimentally identifying and studying topological states in materials such as Bi_2Se_3 [101, 64] and antimony [102, 103, 104]. A search for proposed topological states in the iridates will certainly involve spin-resolved ARPES.

One previous study reported spin-resolved ARPES measurements of $Sr_3Ir_2O_7$ [77], with a primary focus on a Rashba-like surface state. This signal was a small polarization difference from an otherwise large signal that was attributed as possibly due to surface antiferromagnetism. The measurements in this chapter extend the observation of that state across the phase diagram of $(Sr_{1-x}La_x)_3Ir_2O_7$ well into the metallic, antiferromagnetic regime. This state is unusual in that it has nonzero spin polarization at the edge of the Brillouin zone, which apparently violates the combination of time reversal symmetry and lattice translation symmetry. Further, additional photon polarization-dependent measurements here show that this signal is derived from strongly spin-orbit coupled moments, and a photon energy dependence suggests similarities to the analogous to the local Rashba state discussed in the context of $PtSe_2$ in chapter 1.

This work was conducted at the Advanced Light Source using our group's custom-built spin-TOF spectrometer while the synchrotron was running in its two-bunch mode (as the normal multibunch mode results in a repetition rate that is too high for the TOF instrument to distinguish between slow electrons from one bunch and fast electrons from the next). Data were collected at two complementary beamlines. Beamline 4.0.3 provided light with controllable linear polarization that is essential to the discussion in section **??**. Beamline 10.0.1, on the other hand, had only p-polarized light available but gave much higher flux, enabling some of the more high statistics measurements as the measurement rate in these experiments was otherwise quite low.

4.1 Unusual momentum dependence

Figure 4.1 summarizes the basic spin structure observed in an $(\mathrm{Sr}_{1-x}\mathrm{La}_x)_3\mathrm{Ir}_2\mathrm{O}_7$ sample with x = 2.5%. Panels (a) - (c) show spin-resolved ARPES energy distribution curves (EDCs) at several high symmetry points in the Brillouin zone of a $(\mathrm{Sr}_{1-x}\mathrm{La}_x)_3\mathrm{Ir}_2\mathrm{O}_7$ sample with x = 2.5% with spins measured along a direction perpendicular to the electron momentum. In each, the blue curve represents the intensity of measured electrons with spins in the "up" direction, and red for electrons with spins in the "down" direction. The lower half of each of these panels depicts the photoelectron polarization as a function of binding energy, calculated as P = $\frac{I_\uparrow - I_\downarrow}{I_\uparrow + I_\downarrow}$. In all three of these measurements, the $J_{\mathrm{eff}}= \frac{1}{2}$ lower Hubbard band nearest the Fermi energy has a 10-20% polarization in the "up" direction, while deeper bands show signs of opposite polarization. Panel (d) shows the band structure in $\mathrm{Sr}_3\mathrm{Ir}_2\mathrm{O}_7$ from an LDA+SOC+U calculation (adapted from [3]), with $J_{\mathrm{eff}}= \frac{1}{2}$ ($\frac{3}{2}$) bands in red (black). The primary differences between the calculation and experimental observations in this sample are the population of the electron-like band at M and a decrease in the gap between a maximum at X and minimum at M, as well as the higher binding energy of the first band at Γ. The cartoon in panel (e) shows the most relevant features in the Brillouin zone–the electron-like pockets at M are depicted with dark ellipses, while lighter curves show the location of the maxima for the $J_{\mathrm{eff}}= \frac{1}{2}$ band near X. Arrows show the direction of measured spins, with filled in arrowheads for the direction near E_F and open arrows for the spin polarization at higher binding energy.

One of the curious features about this result is the apparent indifference of the observed spin texture to periodicity requirements corresponding to the Brillouin zone of $(\mathrm{Sr}_{1-x}\mathrm{La}_x)_3\mathrm{Ir}_2\mathrm{O}_7$, even considering the larger Brillouin zone that does not account for the staggered rotation of Ir-O octahedra, as shown in panel (e). In either case, the spin at the X point should be zero as it is related to the X point at the opposite corner of the Brillouin zone by both time reversal symmetry and a reciprocal lattice vector. The observation of spin polarization at the Brillouin zone boundary was explored in more detail using the same time-of-flight spectrometer coupled to an 11 eV laser system in our lab. The results of this measurement are shown in figure 4.2. Spin-resolved EDCs at the M point, as well as just inside (M-) and outside (M+) are shown in panels (a)-(c), while the spin-resolved EDC measured at the Γ point is in panel (d). The nonzero polarization at Γ is due to an understood spin-resolved matrix element effect [64] (see section2.4.1) observed in measurements with p-polarized light, and the polarization measured there (≈ 5%) should be read as the effective "zero" of spin polarization for this measurement geometry. Surprisingly, only the measurement precisely at the M point has a spin polarization significantly above this zero (≈ 18%). This is strong

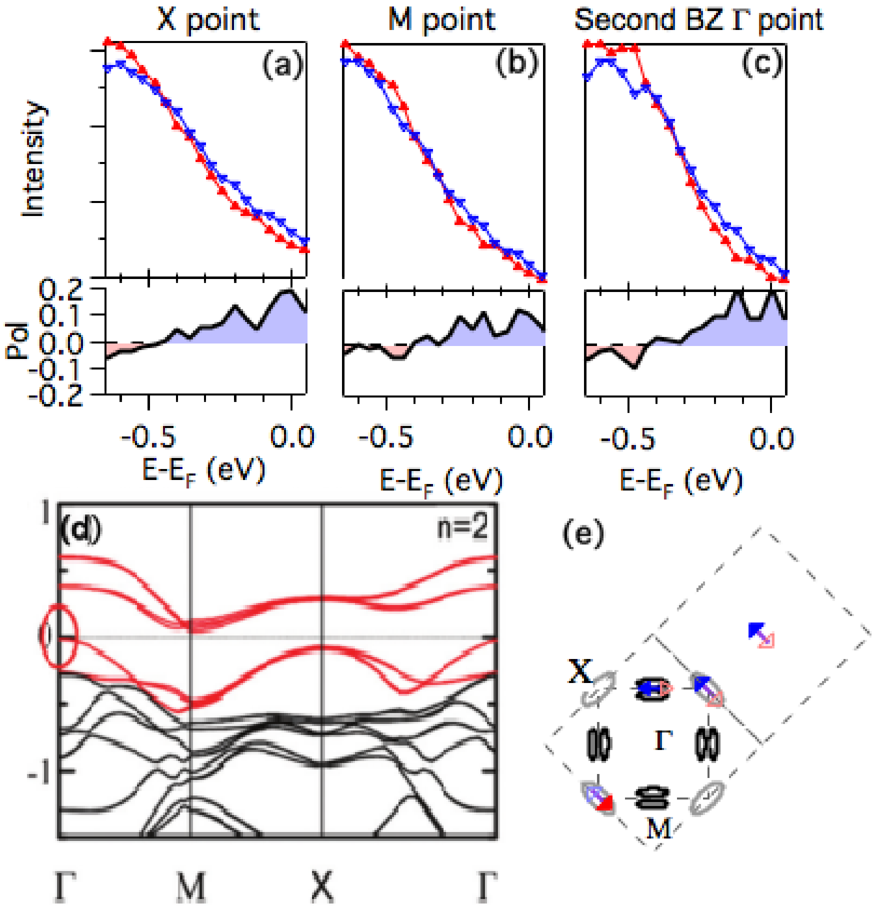

Figure 4.1: Momentum dependence of spin polarizations in an x = 3.1% sample with p-polarized light. (a): Spin-resolved EDCs and spin polarization for the X point of the first Brillouin zone. (b), (c): Same as (a) for an M point in the first Brillouin zone and the Γ point in the second Brillouin zone, respectively. (d): LDA+SOC+U calculation from [2] showing the contributions of $J_{\text{eff}}=\frac{1}{2}$ and $J_{\text{eff}}=\frac{3}{2}$ bands in red and black, respectively. (e): Cartoon of the spin polarization near E_F (filled arrowheads) and near -0.8 eV (open arrowheads)

confirmation that the spins measured at the Brillouin zone boundary is not due to broad momentum resolution. This aspect of the data is not understood, though the fact that the polarization changes sign with kinetic energy and the dependence on incident photon energy and polarization discussed following figures 4.5 and 4.4 rule out simple extrinsic effects. Further, this observation is consistent with the results in $Sr_3Ir_2O_7$ from a previous study [77], which shows peaks in the polarization near the Brillouin zone corners.

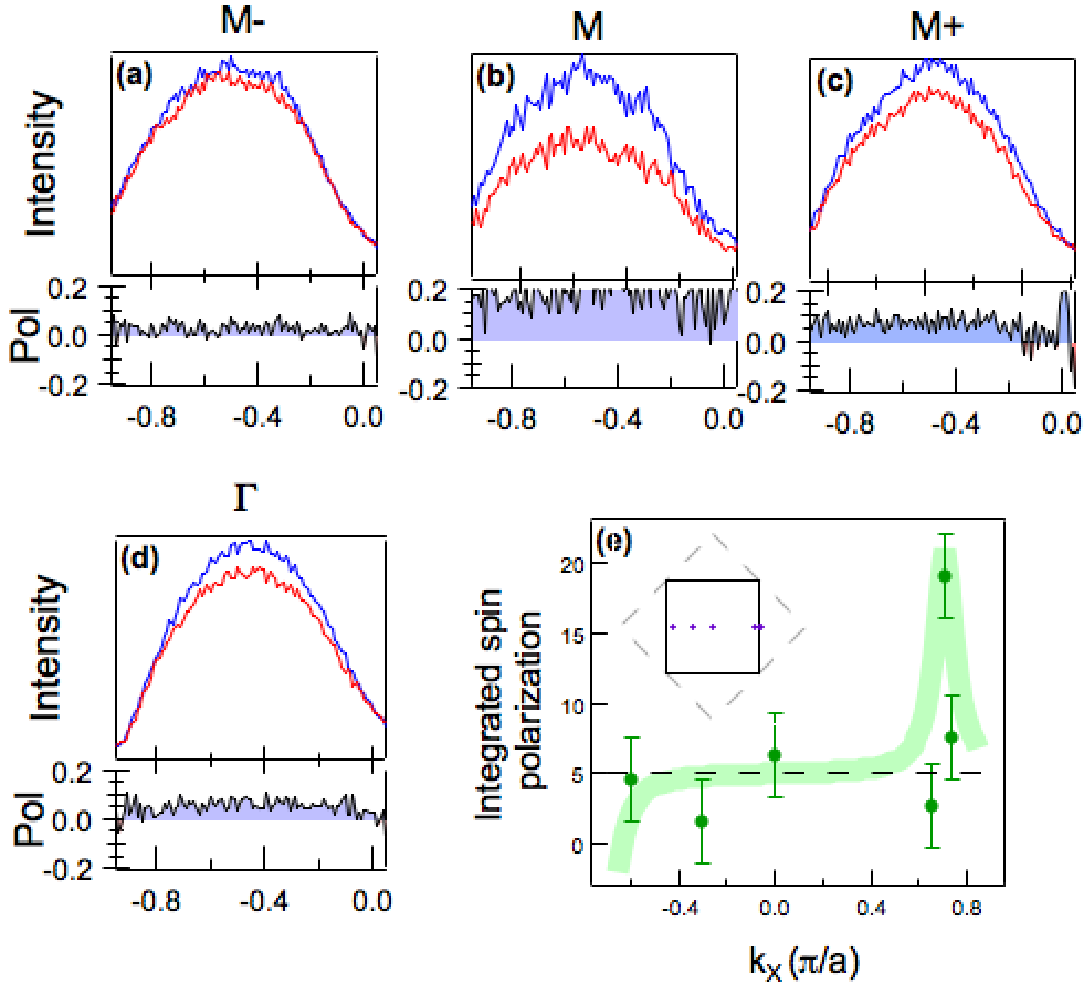

Figure 4.2: Fine momentum dependence of the spin polarization in x = 7%$(Sr_{1-x}La_x)_3Ir_2O_7$ measured with 11eV light. (a) - (c): spin-resolved EDCs just inside (M-), at (M), and outside (M+) the M point, respectively. (d): spin-resolved EDC at Γ for matrix element reference. (e): Spin polarization as a function of k_x along the M-Γ-M direction, with antisymmetric guide to the eye. Inset: momentum locations of the measured spins.

4.2 Doping dependence

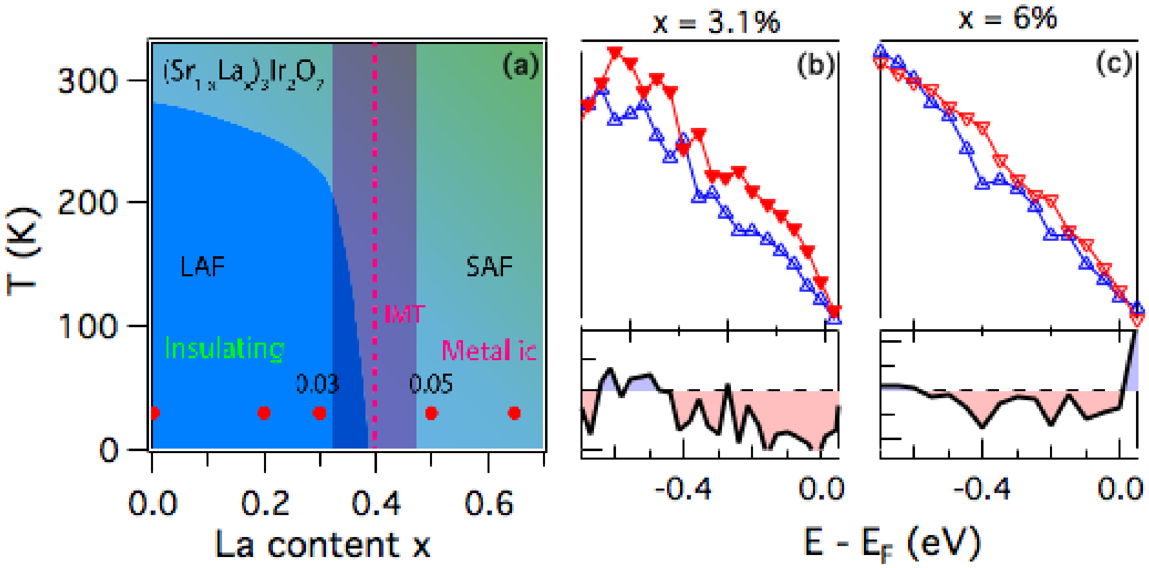

Figure 4.3: Doping dependence of spin polarization at X. (a): Magnetic phase diagram for $(Sr_{1-x}La_x)_3Ir_2O_7$, from [.] (b): Spin-resolved EDC and spin polarization near E_F for an x = 3.1% sample. (c) same as (b) for a x = 6% samples.

The typically-mentioned collinear *c*-axis antiferromagnetic ordering in this system does not break time reversal symmetry, though there have been suggestions of a small canting[105] that would break this symmetry and allow for an observed spin polarization. To this end, we explore the nature of the spin signal as a function across the magnetic transition in $(Sr_{1-x}La_x)_3Ir_2O_7$. In panel a of figure 4.3 we reproduce a phase diagram from [106] which shows the most current understanding of the magnetic ordering in this system. The parent long-range antiferromagnetic insulating state melts in a first-order transition near x = 4% [57], while a short-range magnetic ordering persists in the metallic regime. At high doping levels, the system remains correlated but apparently lacks 3D magnetic ordering. In panels b and c, we show spin-resolved EDCs for the maximum of the lower Hubbard band near the X point for samples at x = 3.1%, and x = 6%, respectively, measured with s-polarized light. The spectral features of the lower Hubbard band become more pronounced with increasing doping (as observed in spin-integrated ARPES experiments), though a spin-polarized signal persists across the phase transition near x = 4% and this it is unlikely that magnetism plays a role in the observed spin signal.

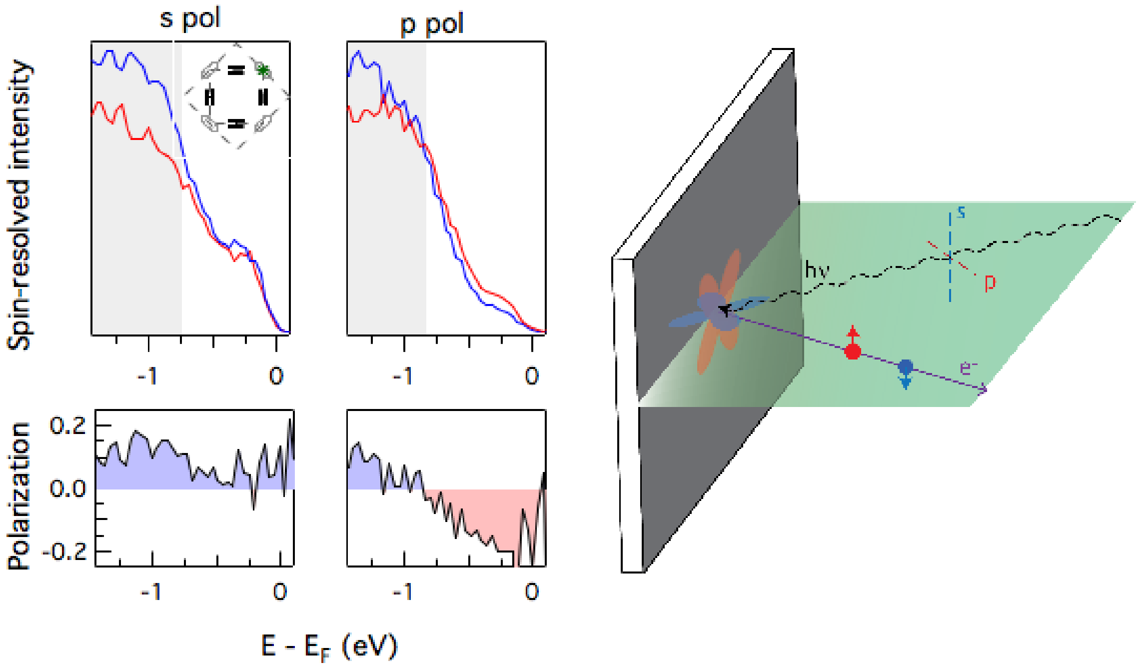

Figure 4.4: Spin flipping in $(Sr_{1-x}La_x)_3Ir_2O_7$. (a): Spin-resolved EDCs and spin polarization at the X point of the first Brillouin zone in a x = 2.5% sample taken with s-polarized light at 55 eV. (b): Same as (a) with p-polarized light. (c) Cartoon for spin flipping mechanism as well as experimental geometry

4.3 Photon polarization dependence

Spin resolved EDCs for the X point in a x = 2.5% samples taken with both s and p polarized light are shown in figure 4.4 for an energy range from 1.5 eV below to 100 meV above E_F. In each, there is are two distinct features near 250 meV and 1 eV corresponding to the $J_{\text{eff}}= \frac{1}{2}$ and $J_{\text{eff}}= \frac{3}{2}$ bands, respectively. The $J_{\text{eff}}= \frac{3}{2}$ band has 15% polarization up in both measurement conditions, while the peak corresponding to the $J_{\text{eff}}= \frac{1}{2}$ peak switches from 20% down to 10% up when switching from s to p polarization. Also noticeable is the relative intensity difference between the $J_{\text{eff}}= \frac{1}{2}$ bands near E_F and the $J_{\text{eff}}= \frac{3}{2}$ bands at deeper binding energies with polarization. A cartoon related to the origin for this spin-flipping phenomenon (which has been previously reported in Bi_2Se_3[107]) is shown in panel c. Though the underlying orbitals for these $J_{\text{eff}}= \frac{1}{2}$ states are Ir 5d orbitals rather than the p orbitals of a $j = \frac{1}{2}$ state, a similar calculation gives this spin flipping effect. The essential physics is the entanglement between the spin and orbital angular momenta of electrons in the solid. By changing the polarization of the incoming light, the photoemission matrix elements will select for electrons with different spatial symmetry, which depends only on the orbital portion of the angular momentum. Depending on the details of the wave functions and final states involved, this can give spin polarizations from P = -1 to +1 for a j = $\frac{1}{2}$ state, though the polarizations measured here are more modest. The same idea suggests an explanation for the lack of flipping in the J_{eff}= $\frac{3}{2}$ bands: for a fully polarized j = $\frac{3}{2}$ state, there is only one combination of $\vec{\ell}$ and $\vec{s}$ that contribute, and changing the polarization of incident light will only affect the intensity rather than contributing to the spin polarization.

4.4 Photon energy dependence

While the overall spin polarization from the bulk in this system must be zero due to simultaneous inversion and time-reversal symmetry, it is possible for our observed signal to be a surface effect (where inversion symmetry is explicitly broken) or due to a local inversion symmetry breaking, as observed in $PtSe_2$ and other systems [15, 16]. In this picture, inversion symmetry is broken at the Ir site by a different atom in the layer above than in the layer below its oxygen octahedron (Sr rather than Ir, or vice versa). This can give rise to an electric field near the Ir site that induces a Rashba-like splitting of the bands in each layer that cancels out in the bulk crystal on average. Treating this as a layer-dependent electric field along the c-axis gives rise to a layer-dependent spin polarization in the bonding and antibonding bands which should cancel in each layer, as shown in figure 4.5. Two factors are then sufficient to give rise to a nonzero spin signal–stronger photoemission signal from the top layer of the unit cell, and preference for either the bonding or antibonding band. The surface sensitive nature of photoemission is well known, and $Sr_3Ir_2O_7$ has a preferential cleaving plane (shown by the horizontal dashed line in panel e), so the signal from the top layer of each unit cell will be at stronger than that from the bottom layer. It is also known from a photon-energy-dependent ARPES study of undoped $Sr_3Ir_2O_7$ that the relative contributions of the bonding and antibonding bands to the photoemission intensity at the X point near E_F is strongly photon-energy dependent[76]. Assuming a periodicity in k_z of $10\pi/c$ and an inner potential of 10 eV as seen in that work gives the curve in panel f. Panels a-d show spin-resolved EDCs and corresponding spin polarizations in insulating samples at the X point for a range of photon energies which are consistent with this picture of the origin of the observed spin signal. Namely, both the $h\nu = 35$ eV and $h\nu = 82$ eV measurements should be dominated by the contribution of the antibonding band, and have the same sign of observed spin polarization. The $h\nu = 55$ eV measurement should have more signal from the bonding band, and shows the opposite spin polarization. Lastly, the $h\nu =$ 100 eV measurement in panel d should have roughly equal contributions from the bonding and antibonding bands, and shows no clear spin polarization in the valence band.

4.5 Conclusion

Together these observations reveal a a consistent spin-polarized photoemission signal across the metal-insulator transition in $(Sr_{1-x}La_x)_3Ir_2O_7$. The lack of periodicity in this signal

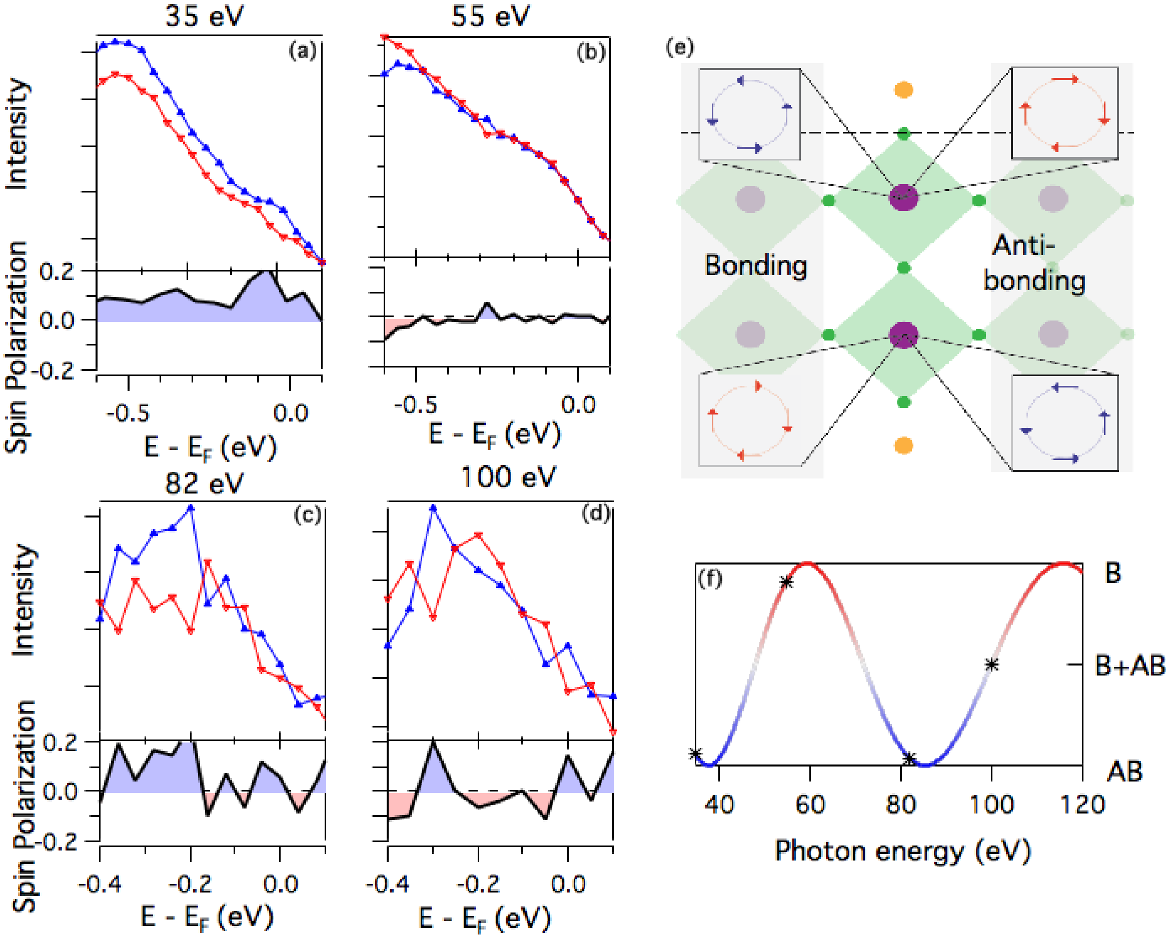

Figure 4.5: Photon energy dependence of the observed spin signal. (a): Spin-resolved EDC and spin polarization near E_F for an insulating sample at the X point measured with a photon energy of $h\nu = 35$ eV. (b)-(d) Same as (a) for $h\nu = 55$ eV, 82 eV, and 100 eV. (e): Cartoon of bilayer structure in $Sr_3Ir_2O_7$ with proposed layer and band-dependent spin polarization. (f): Relative contributions of banding and antibonding bands to photoemission intensity in $Sr_3Ir_2O_7$, from [76]

with the Brillouin zone of $(Sr_{1-x}La_x)_3Ir_2O_7$ is unusual, and suggests a need for further development in the theory of how spin-orbit coupling can effect correlated states, or that the photoemission process is more complicated than currently understood when viewed in the light of spins. The dependence of the spin signal on electron binding energy indicate that this signal originates in the physics of the crystal rather than some external process. The dependence on photon polarization and energy suggest a strong role of spin-orbit coupling and a possible layer-dependent spin texture.

Aside from the lack of periodicity, these results are similar to recent measurements from our group on $Bi_2Sr_2CaCu_2O_{8+\delta}$, where a consistent spin structure is observed across the superconducting dome and displays a photon energy dependence similar to here [108]. As in the case of spin-integrated ARPES, a thorough comparison between these results and spin-resolved ARPES on the single-layer Sr_2IrO_4 (for which no results currently exist in the literature) is warranted to ascertain the essential ingredients of this new phenomenon.

Bibliography

[1] B. J. Kim et al. “Novel $J_{\text{eff}} = 1/2$ Mott State Induced by Relativistic Spin-Orbit Coupling in Sr_2IrO_4”. In: *Phys. Rev. Lett.* 101 (7 2008), p. 076402. DOI: 10.1103/PhysRevLett.101.076402. URL: http://link.aps.org/doi/10.1103/PhysRevLett.101.076402.

[2] S. J. Moon et al. “Dimensionality-Controlled Insulator-Metal Transition and Correlated Metallic State in $5d$ Transition Metal Oxides $Sr_{n+1}Ir_nO_{3n+1}$ ($n = 1$, 2, and ∞)”. In: *Phys. Rev. Lett.* 101 (22 2008), p. 226402. DOI: 10.1103/PhysRevLett.101.226402. URL: http://link.aps.org/doi/10.1103/PhysRevLett.101.226402.

[3] Q. Wang et al. “Dimensionality-controlled Mott transition and correlation effects in single-layer and bilayer perovskite iridates”. In: *Phys. Rev. B* 87 (24 2013), p. 245109. DOI: 10.1103/PhysRevB.87.245109. URL: http://link.aps.org/doi/10.1103/PhysRevB.87.245109.

[4] Yogesh Singh and P. Gegenwart. “Antiferromagnetic Mott insulating state in single crystals of the honeycomb lattice material Na2IrO3”. In: *Physical Review B - Condensed Matter and Materials Physics* 82.6 (2010), pp. 1–7. ISSN: 10980121. DOI: 10.1103/PhysRevB.82.064412. arXiv: 1006.0437.

[5] R. Comin et al. “Na_2IrO_3 as a Novel Relativistic Mott Insulator with a 340-meV Gap”. In: *Phys. Rev. Lett.* 109 (26 2012), p. 266406. DOI: 10.1103/PhysRevLett.109.266406. URL: https://link.aps.org/doi/10.1103/PhysRevLett.109.266406.

[6] Yogesh Singh et al. “Relevance of the Heisenberg-Kitaev Model for the Honeycomb Lattice Iridates A_2IrO_3”. In: *Phys. Rev. Lett.* 108 (12 2012), p. 127203. DOI: 10.1103/PhysRevLett.108.127203. URL: https://link.aps.org/doi/10.1103/PhysRevLett.108.127203.

[7] Ji Chaloupka, George Jackeli, and Giniyat Khaliullin. “Kitaev-Heisenberg Model on a Honeycomb Lattice: Possible Exotic Phases in Iridium Oxides A_2IrO_3”. In: *Phys. Rev. Lett.* 105 (2 2010), p. 027204. DOI: 10.1103/PhysRevLett.105.027204. URL: https://link.aps.org/doi/10.1103/PhysRevLett.105.027204.

[8] Fa Wang and T. Senthil. "Twisted Hubbard Model for Sr2IrO4: Magnetism and Possible High Temperature Superconductivity". In: *Phys. Rev. Lett.* 106 (13 2011), p. 136402. DOI: 10.1103/PhysRevLett.106.136402. URL: http://link.aps.org/doi/10.1103/PhysRevLett.106.136402.

[9] Dmytro Pesin and Leon Balents. "Mott physics and band topology in materials with strong spin–orbit interaction". In: *Nature Physics* 6 (Mar. 2010), 376 EP –. URL: http://dx.doi.org/10.1038/nphys1606.

[10] L. D. Landau. "The Theory of a Fermi Liquid". In: *Soviet Physics JETP* 3.6 (1957), pp. 920–925.

[11] N F Mott and R Peierls. "Discussion of the paper by de Boer and Verwey". In: *Proceedings of the Physical Society* 49.4S (1937), p. 72. URL: http://stacks.iop.org/0959-5309/49/i=4S/a=308.

[12] "Electron correlations in narrow energy bands". In: *Proceedings of the Royal Society of London A: Mathematical, Physical and Engineering Sciences* 276.1365 (1963), pp. 238–257. ISSN: 0080-4630. DOI: 10.1098/rspa.1963.0204. eprint: http://rspa.royalsocietypublishing.org/content/276/1365/238.full.pdf. URL: http://rspa.royalsocietypublishing.org/content/276/1365/238.

[13] P. YU and M. Cardona. *Fundamentals of Semiconductors: Physics and Materials Properties*. Advanced texts in physics v. 3. Springer Berlin Heidelberg, 2005. ISBN: 9783540254706. URL: https://books.google.com/books?id=W9pdJZoAeyEC.

[14] Drew W. Latzke et al. "Electronic structure, spin-orbit coupling, and interlayer interaction in bulk MoS_2 and WS_2". In: *Phys. Rev. B* 91 (23 2015), p. 235202. DOI: 10.1103/PhysRevB.91.235202. URL: https://link.aps.org/doi/10.1103/PhysRevB.91.235202.

[15] Xiuwen Zhang et al. "Hidden spin polarization in inversion-symmetric bulk crystals". In: *Nature Physics* 10 (Apr. 2014), 387 EP –. URL: http://dx.doi.org/10.1038/nphys2933.

[16] Wei Yao et al. "Direct observation of spin-layer locking by local Rashba effect in monolayer semiconducting PtSe2 film". In: 8 (Jan. 2017), 14216 EP –. URL: http://dx.doi.org/10.1038/ncomms14216.

[17] Chetan Dhital et al. "Neutron scattering study of correlated phase behavior in Sr_2IrO_4". In: *Physical Review B* 87.14 (2013), p. 144405. ISSN: 1098-0121. DOI: 10.1103/PhysRevB.87.144405. arXiv: 1212.1489. URL: http://link.aps.org/doi/10.1103/PhysRevB.87.144405.

[18] Tom Hogan et al. "Structural investigation of the bilayer iridate Sr 3 Ir 2 O 7". In: *Phys. Rev. B* 134110 (2016), pp. 2–7. DOI: 10.1103/PhysRevB.93.134110.

[19] M. Moretti Sala et al. “Resonant X-Ray Scattering and the jeff=1/2 Electronic Ground State in Iridate Perovskites”. In: *Physical Review Letters* 112.2 (2014), p. 026403. ISSN: 0031-9007. DOI: 10.1103/PhysRevLett.112.026403. URL: http://link.aps.org/doi/10.1103/PhysRevLett.112.026403.

[20] G. Jackeli and G. Khaliullin. “Mott Insulators in the Strong Spin-Orbit Coupling Limit: From Heisenberg to a Quantum Compass and Kitaev Models”. In: *Phys. Rev. Lett.* 102 (1 2009), p. 017205. DOI: 10.1103/PhysRevLett.102.017205. URL: http://link.aps.org/doi/10.1103/PhysRevLett.102.017205.

[21] Alexei Kitaev. “Anyons in an exactly solved model and beyond”. In: *Annals of Physics* 321.1 (2006). January Special Issue, pp. 2 –111. ISSN: 0003-4916. DOI: https://doi.org/10.1016/j.aop.2005.10.005. URL: http://www.sciencedirect.com/science/article/pii/S0003491605002381.

[22] G. Baskaran, Saptarshi Mandal, and R. Shankar. “Exact Results for Spin Dynamics and Fractionalization in the Kitaev Model”. In: *Phys. Rev. Lett.* 98 (24 2007), p. 247201. DOI: 10.1103/PhysRevLett.98.247201. URL: https://link.aps.org/doi/10.1103/PhysRevLett.98.247201.

[23] Itamar Kimchi, James G. Analytis, and Ashvin Vishwanath. “Three-dimensional quantum spin liquids in models of harmonic-honeycomb iridates and phase diagram in an infinite- D approximation”. In: *Physical Review B - Condensed Matter and Materials Physics* 90.20 (2014), pp. 1–20. ISSN: 1550235X. DOI: 10.1103/PhysRevB.90.205126. arXiv: 1309.1171.

[24] Ji Chaloupka, George Jackeli, and Giniyat Khaliullin. “Zigzag magnetic order in the iridium oxide Na2IrO3”. In: *Physical Review Letters* 110.9 (2013), pp. 1–5. ISSN: 00319007. DOI: 10.1103/PhysRevLett.110.097204. arXiv: 1209.5100.

[25] S. K. Choi et al. “Spin Waves and Revised Crystal Structure of Honeycomb Iridate Na_2IrO_3”. In: *Phys. Rev. Lett.* 108 (12 2012), p. 127204. DOI: 10.1103/PhysRevLett.108.127204. URL: https://link.aps.org/doi/10.1103/PhysRevLett.108.127204.

[26] Hong-Chen Jiang et al. “Possible proximity of the Mott insulating iridate Na 2 IrO 3 to a topological phase: Phase diagram of the Heisenberg-Kitaev model in a magnetic field”. In: *Phys. Rev. B* 83 (24 2011), p. 245104. DOI: 10.1103/PhysRevB.83.245104. URL: http://link.aps.org/doi/10.1103/PhysRevB.83.245104.

[27] Fabien Trousselet et al. “Hidden quasiparticles and incoherent photoemission spectra in Na 2IrO3”. In: *Physical Review Letters* 111.3 (2013), pp. 1–5. ISSN: 00319007. DOI: 10.1103/PhysRevLett.111.037205. arXiv: 1302.0187.

[28] Feng Ye et al. “Direct evidence of a zigzag spin-chain structure in the honeycomb lattice: A neutron and x-ray diffraction investigation of single-crystal Na 2IrO 3”. In: *Physical Review B - Condensed Matter and Materials Physics* 85.18 (2012), pp. 1–4. ISSN: 10980121. DOI: 10.1103/PhysRevB.85.180403. arXiv: 1202.3995v2.

[29] Atsuo Shitade et al. “Quantum Spin Hall Effect in a Transition Metal Oxide Na_2IrO_3”. In: *Phys. Rev. Lett.* 102 (25 2009), p. 256403. DOI: 10.1103/PhysRevLett.102.256403. URL: http://link.aps.org/doi/10.1103/PhysRevLett.102.256403.

[30] Choong H. Kim et al. “Topological Quantum Phase Transition in $5d$ Transition Metal Oxide Na_2IrO_3”. In: *Phys. Rev. Lett.* 108 (10 2012), p. 106401. DOI: 10.1103/PhysRevLett.108.106401. URL: http://link.aps.org/doi/10.1103/PhysRevLett.108.106401.

[31] K a Modic et al. “Realization of a three-dimensional spin-anisotropic harmonic honeycomb iridate.” In: *Nature communications* 5.May (2014), p. 4203. ISSN: 2041-1723. DOI: 10.1038/ncomms5203. arXiv: 1402.3254. URL: http://www.ncbi.nlm.nih.gov/pubmed/24969742.

[32] Hongbin Zhang, Kristjan Haule, and David Vanderbilt. “Effective J=1/2 Insulating State in Ruddlesden-Popper Iridates: An LDA+DMFT Study”. In: *Physical Review Letters* 111.24 (2013), p. 246402. ISSN: 0031-9007. DOI: 10.1103/PhysRevLett.111.246402. URL: http://link.aps.org/doi/10.1103/PhysRevLett.111.246402.

[33] Jean-Michel Carter and Hae-Young Kee. “Microscopic theory of magnetism in $Sr_3Ir_2O_7$”. In: *Physical Review B* 87.1 (2013), p. 014433. ISSN: 1098-0121. DOI: 10.1103/PhysRevB.87.014433. URL: http://link.aps.org/doi/10.1103/PhysRevB.87.014433.

[34] Jean-Michel Carter, V. Vijay Shankar, and Hae-Young Kee. “Theory of magnetism and metal-insulator transition in layered perovskite iridates”. In: (2012), p. 11. DOI: 10.1103/PhysRevB.88.035111. arXiv: 1207.2183. URL: http://arxiv.org/abs/1207.2183.

[35] D a Zocco et al. “Persistent non-metallic behavior in Sr2IrO4 and Sr3Ir2O7 at high pressures.” In: *Journal of physics. Condensed matter : an Institute of Physics journal* 26.25 (2014), p. 255603. ISSN: 1361-648X. DOI: 10.1088/0953-8984/26/25/255603. URL: http://www.ncbi.nlm.nih.gov/pubmed/24888379.

[36] Z Zhao et al. “Pressure induced second-order structural transition in Sr3Ir2O7.” In: *Journal of physics. Condensed matter : an Institute of Physics journal* 26.21 (2014), p. 215402. ISSN: 1361-648X. DOI: 10.1088/0953-8984/26/21/215402. URL: http://www.ncbi.nlm.nih.gov/pubmed/24805299.

[37] C. Donnerer et al. “Pressure-induced metallization of the spin-orbit Mott insulator Sr3Ir2O7”. In: *arXiv* 15 (2015), pp. 1–5. arXiv: 1508.04320. URL: http://arxiv.org/abs/1508.04320.

[38] Y. J. Yan et al. “Electron-Doped Sr_2IrO_4: An Analogue of Hole-Doped Cuprate Superconductors Demonstrated by Scanning Tunneling Microscopy”. In: *Phys. Rev. X* 5 (4 2015), p. 041018. DOI: 10.1103/PhysRevX.5.041018. URL: https://link.aps.org/doi/10.1103/PhysRevX.5.041018.

[39] YK Kim et al. “Observation of a d-wave gap in electron-doped Sr2IrO4”. In: *Nature Physics* 12.1 (2016), pp. 37–41.

[40] Carlos Cosio-Castaneda et al. “Structure and magnetic properties of the weak ferromagnet Sr 2-x La x IrO 4”. In: *Journal of Physics: Condensed Matter* 19.44 (2007), p. 446210. URL: http://stacks.iop.org/0953-8984/19/i=44/a=446210.

[41] Xiang Chen et al. “Influence of electron doping on the ground state of $(\mathrm{Sr}_{1-x}\mathrm{La}_x)_2\mathrm{IrO}_4$”. In: *Phys. Rev. B* 92 (7 2015), p. 075125. DOI: 10.1103/PhysRevB.92.075125. URL: https://link.aps.org/doi/10.1103/PhysRevB.92.075125.

[42] Yue Cao et al. “Hallmarks of the Mott Metal Crossover in the Hole Doped J=1/2 Insulator Sr2IrO4”. In: *arXiv* (2014).

[43] a. Glamazda et al. “Effects of hole doping on magnetic and lattice excitations in Sr2Ir1-xRuxO4 (x=0–0.2)”. In: *Physical Review B* 89.10 (2014), p. 104406. ISSN: 1098-0121. DOI: 10.1103/PhysRevB.89.104406. URL: http://link.aps.org/doi/10.1103/PhysRevB.89.104406.

[44] O. B. Korneta et al. “Electron-doped $\mathrm{Sr}_2\mathrm{IrO}_{4-\delta}$ $(0 \leq \delta \leq 0.04)$: Evolution of a disordered $J_{\text{eff}} = \frac{1}{2}$ Mott insulator into an exotic metallic state”. In: *Phys. Rev. B* 82 (11 2010), p. 115117. DOI: 10.1103/PhysRevB.82.115117. URL: http://link.aps.org/doi/10.1103/PhysRevB.82.115117.

[45] T. F. Qi et al. “Electron-doped $\mathrm{Sr}_2\mathrm{IrO}_{4-\delta}$ $(0 \leq \delta \leq 0.04)$: Evolution of a disordered $J_{\text{eff}} = \frac{1}{2}$ Mott insulator into an exotic metallic state”. In: *Journal of Applied Physics* 109.7 (2011), p. 07D906. ISSN: 00218979. DOI: 10.1063/1.3545803. URL: http://scitation.aip.org/content/aip/journal/jap/109/7/10.1063/1.3545803.

[46] T. F. Qi et al. “Spin-orbit tuned metal-insulator transitions in single-crystal $\mathrm{Sr}_2\mathrm{Ir}_{1-x}\mathrm{Rh}_x\mathrm{O}_4$ $(0 \leq \mathrm{x} \leq 0.16)$”. In: *Physical Review B - Condensed Matter and Materials Physics* 86.12 (2012), pp. 1–6. ISSN: 10980121. DOI: 10.1103/PhysRevB.86.125105.

[47] J. S. Lee et al. “Insulator-metal transition driven by change of doping and spin-orbit interaction in Sr 2IrO 4”. In: *Physical Review B - Condensed Matter and Materials Physics* 85.3 (2012), pp. 2–7. ISSN: 10980121. DOI: 10.1103/PhysRevB.85.035101.

[48] L. Li et al. “Tuning the $J_{\text{eff}} = \frac{1}{2}$ insulating state via electron doping and pressure in the double-layered iridate $\mathrm{Sr}_3\mathrm{Ir}_2\mathrm{O}_7$”. In: *Phys. Rev. B* 87 (23 2013), p. 235127. DOI: 10.1103/PhysRevB.87.235127. URL: http://link.aps.org/doi/10.1103/PhysRevB.87.235127.

[49] S Boseggia et al. “On the magnetic structure of $\mathrm{Sr}_3\mathrm{Ir}_2\mathrm{O}_7$: an x-ray resonant scattering study.” In: *Journal of physics. Condensed matter : an Institute of Physics journal* 24.31 (2012), p. 312202. ISSN: 1361-648X. DOI: 10.1088/0953-8984/24/31/312202. URL: http://www.ncbi.nlm.nih.gov/pubmed/22776837.

[50] S. Fujiyama et al. “Weak antiferromagnetism of $J_{\text{eff}} = \frac{1}{2}$ band in bilayer iridate $Sr_3Ir_2O_7$”. In: *Physical Review B* 86.17 (2012), p. 174414. ISSN: 1098-0121. DOI: 10.1103/PhysRevB.86.174414. URL: http://link.aps.org/doi/10.1103/PhysRevB.86.174414.

[51] Jungho Kim et al. “Large Spin-Wave Energy Gap in the Bilayer Iridate $Sr_3Ir_2O_7$: Evidence for Enhanced Dipolar Interactions Near the Mott Metal-Insulator Transition”. In: *Physical Review Letters* 109.15 (2012), p. 157402. ISSN: 0031-9007. DOI: 10.1103/PhysRevLett.109.157402. URL: http://link.aps.org/doi/10.1103/PhysRevLett.109.157402.

[52] S. Boseggia et al. “Robustness of Basal-Plane Antiferromagnetic Order and the J_{eff}=1/2 State in Single-Layer Iridate Spin-Orbit Mott Insulators”. In: *Phys. Rev. Lett.* 110 (11 2013), p. 117207. DOI: 10.1103/PhysRevLett.110.117207. URL: https://link.aps.org/doi/10.1103/PhysRevLett.110.117207.

[53] S. Calder et al. “Evolution of competing magnetic order in the $J_{\text{eff}} = 1/2$ insulating state of $Sr_2Ir_{1-x}Ru_xO_4$”. In: *Phys. Rev. B* 92 (16 2015), p. 165128. DOI: 10.1103/PhysRevB.92.165128. URL: https://link.aps.org/doi/10.1103/PhysRevB.92.165128.

[54] S. Calder et al. “Magnetic structural change of Sr_2IrO_4 upon Mn doping”. In: *Phys. Rev. B* 86 (22 2012), p. 220403. DOI: 10.1103/PhysRevB.86.220403. URL: https://link.aps.org/doi/10.1103/PhysRevB.86.220403.

[55] Bongjae Kim, Peitao Liu, and Cesare Franchini. “Magnetic properties of bilayer $Sr_3Ir_2O_7$: Role of epitaxial strain and oxygen vacancies”. In: *Physical Review B* 95.2 (2017), p. 024406. ISSN: 2469-9950. DOI: 10.1103/PhysRevB.95.024406. URL: http://link.aps.org/doi/10.1103/PhysRevB.95.024406.

[56] Jia-wei Mei. “Bilayer Twisted Hubbard Model for Sr3Ir2O7”. In: c (2012), pp. 1–5. arXiv: arXiv:1210.1974v1.

[57] Tom Hogan et al. “First-order Melting of a Weak Spin-Orbit Mott Insulator into a Correlated Metal”. In: *Phys. Rev. Lett.* 114 (2015), p. 257203.

[58] Chetan Dhital et al. “Spin ordering and electronic texture in the bilayer iridate $Sr_3Ir_2O_7$”. In: *Physical Review B* 86.10 (2012), p. 100401.

[59] Tom Hogan et al. “Disordered dimer state in electron-doped Sr3Ir2 O7”. In: *Physical Review B - Condensed Matter and Materials Physics* 94.10 (2016), pp. 1–5. ISSN: 1550235X. DOI: 10.1103/PhysRevB.94.100401. arXiv: 1608.03565.

[60] H. J. Park et al. “Phonon-assisted optical excitation in the narrow bandgap Mott insulator Sr3Ir2O7”. In: *Physical Review B* 89.15 (2014), p. 155115. ISSN: 1098-0121. DOI: 10.1103/PhysRevB.89.155115. URL: http://link.aps.org/doi/10.1103/PhysRevB.89.155115.

[61] H. Chu et al. "A charge density wave-like instability in a doped spin-orbit-assisted weak Mott insulator". In: *Nat Mater* 16.2 (Feb. 2017), pp. 200–203. URL: `http://dx.doi.org/10.1038/nmat4836`.

[62] Andrea Damascelli, Zahid Hussain, and Zhi-Xun Shen. "Angle-resolved photoemission studies of the cuprate superconductors". In: *Rev. Mod. Phys.* 75 (2 2003), pp. 473–541. DOI: `10.1103/RevModPhys.75.473`. URL: `http://link.aps.org/doi/10.1103/RevModPhys.75.473`.

[63] Andrea Damascelli. "Probing the Electronic Structure of Complex Systems by ARPES". In: *Physica Scripta* 2004.T109 (2004), p. 61. URL: `http://stacks.iop.org/1402-4896/2004/i=T109/a=005`.

[64] C. Jozwiak et al. "A high-efficiency spin-resolved photoemission spectrometer combining time-of-flight spectroscopy with exchange-scattering polarimetry". In: *Review of Scientific Instruments* 81.5 (2010), p. 053904. DOI: `10.1063/1.3427223`. eprint: `https://doi.org/10.1063/1.3427223`. URL: `https://doi.org/10.1063/1.3427223`.

[65] N A Cherepkov. "Spin polarisation of photoelectrons ejected from unpolarised atoms". In: *Journal of Physics B: Atomic and Molecular Physics* 12.8 (1979), p. 1279. URL: `http://stacks.iop.org/0022-3700/12/i=8/a=005`.

[66] Ch. Roth et al. "Spin Polarization in Cu Core-Level Photoemission with Linearly Polarized Soft X Rays". In: *Phys. Rev. Lett.* 73 (14 1994), pp. 1963–1966. DOI: `10.1103/PhysRevLett.73.1963`. URL: `https://link.aps.org/doi/10.1103/PhysRevLett.73.1963`.

[67] H. B. Rose et al. "Spin-orbit-induced spin polarization in W 4f photoemission". In: *Phys. Rev. B* 53 (3 1996), pp. 1630–1634. DOI: `10.1103/PhysRevB.53.1630`. URL: `https://link.aps.org/doi/10.1103/PhysRevB.53.1630`.

[68] S.-W. Yu and J. G. Tobin. "Breakdown of spatial inversion symmetry in core-level photoemission of Pt(001)". In: *Phys. Rev. B* 77 (19 2008), p. 193409. DOI: `10.1103/PhysRevB.77.193409`. URL: `https://link.aps.org/doi/10.1103/PhysRevB.77.193409`.

[69] C. Jozwiak et al. "Widespread spin polarization effects in photoemission from topological insulators". In: *Phys. Rev. B* 84 (16 2011), p. 165113. DOI: `10.1103/PhysRevB.84.165113`. URL: `https://link.aps.org/doi/10.1103/PhysRevB.84.165113`.

[70] Gregory Affeldt et al. "Spectral weight suppression near a metal-insulator transition in a double-layer electron-doped iridate". In: *Phys. Rev. B* 95 (23 2017), p. 235151. DOI: `10.1103/PhysRevB.95.235151`. URL: `https://link.aps.org/doi/10.1103/PhysRevB.95.235151`.

[71] Gregory Affeldt et al. "Doping-dependent correlation effects in $(Sr_{1-x}La_x)_3Ir_2O_7$". In: *Phys. Rev. B* 97 (12 2018), p. 125111. DOI: `10.1103/PhysRevB.97.125111`. URL: `https://link.aps.org/doi/10.1103/PhysRevB.97.125111`.

[72] Bastian M Wojek et al. "The $J_{\text{eff}} = \frac{1}{2}$ insulator $Sr_3Ir_2O_7$ studied by means of angle-resolved photoemission spectroscopy". In: *Journal of Physics: Condensed Matter* 24.41 (2012), p. 415602.

[73] Junfeng He et al. "Spectroscopic evidence for negative electronic compressibility in a quasi-three-dimensional spin-orbit correlated metal". In: *Nat Mater* 14.6 (June 2015), pp. 577–582. ISSN: 1476-1122. URL: http://dx.doi.org/10.1038/nmat427310.1038/nmat4273http://www.nature.com/nmat/journal/v14/n6/abs/nmat4273.html\#supplementary-information.

[74] Junfeng He et al. "Fermi Arcs vs. Fermi Pockets in Electron-doped Perovskite Iridates". In: *Sci. Rep.* 5 (Feb. 2015). URL: http://dx.doi.org/10.1038/srep0853310.1038/srep08533http://www.nature.com/srep/2015/150223/srep08533/abs/srep08533.html\#supplementary-information.

[75] A. de la Torre et al. "Coherent Quasiparticles with a Small Fermi Surface in Lightly Doped $Sr_3Ir_2O_7$". In: *Phys. Rev. Lett.* 113 (25 2014), p. 256402. DOI: 10.1103/PhysRevLett.113.256402. URL: http://link.aps.org/doi/10.1103/PhysRevLett.113.256402.

[76] L. Moreschini et al. "Bilayer splitting and wave functions symmetry in $Sr_3Ir_2O_7$". In: *Phys. Rev. B* 89 (20 2014), p. 201114. DOI: 10.1103/PhysRevB.89.201114. URL: http://link.aps.org/doi/10.1103/PhysRevB.89.201114.

[77] Chang Liu et al. "Spin-correlated electronic state on the surface of a spin-orbit Mott system". In: *Phys. Rev. B* 90 (4 2014), p. 045127. DOI: 10.1103/PhysRevB.90.045127. URL: http://link.aps.org/doi/10.1103/PhysRevB.90.045127.

[78] A. de la Torre et al. "Collapse of the Mott Gap and Emergence of a Nodal Liquid in Lightly Doped Sr_2IrO_4". In: *Phys. Rev. Lett.* 115 (17 2015), p. 176402. DOI: 10.1103/PhysRevLett.115.176402. URL: http://link.aps.org/doi/10.1103/PhysRevLett.115.176402.

[79] Wilfried Wunderlich, Hiromichi Ohta, and Kunihito Koumoto. "Enhanced effective mass in doped SrTiO3 and related perovskites". In: *Physica B: Condensed Matter* 404.16 (2009), pp. 2202 –2212. ISSN: 0921-4526. DOI: https://doi.org/10.1016/j.physb.2009.04.012. URL: http://www.sciencedirect.com/science/article/pii/S0921452609002257.

[80] Gihyeon Ahn et al. "Infrared Spectroscopic Evidences of Strong Electronic Correlations in (Sr1?xLax)3Ir2O7". In: *Scientific Reports* 6 (Sept. 2016), 32632 EP –. URL: http://dx.doi.org/10.1038/srep32632.

[81] X. J. Zhou et al. "Universal nodal Fermi velocity". In: *Nature* 423.May (2003), pp. 398–399. ISSN: 0028-0836. DOI: 10.1038/423398a. URL: http://www.nature.com/nature/journal/v423/n6938/full/423398a.html.

[82] W. Meevasana et al. “Hierarchy of multiple many-body interaction scales in high-temperature superconductors”. In: *Physical Review B - Condensed Matter and Materials Physics* 75.17 (2007), pp. 1–7. ISSN: 10980121. DOI: `10.1103/PhysRevB.75.174506`. arXiv: `0612541 [cond-mat]`.

[83] J. Graf et al. “Universal high energy anomaly in the angle-resolved photoemission spectra of high temperature superconductors: Possible evidence of spinon and holon branches”. In: *Physical Review Letters* 98.6 (2007), pp. 1–4. ISSN: 00319007. DOI: `10.1103/PhysRevLett.98.067004`. arXiv: `0607319 [cond-mat]`.

[84] Yan Liu et al. “Anomalous High-Energy Waterfall-Like Electronic Structure in 5 d Transition Metal Oxide Sr2IrO4 with a Strong Spin-Orbit Coupling”. In: *Scientific Reports* 5 (2015), p. 13036. URL: `http://dx.doi.org/10.1038/srep1303610.1038/srep13036http://www.nature.com/articles/srep13036{\#}supplementary-information`.

[85] B. Moritz, S. Johnston, and T.P. Devereaux. “Insights on the cuprate high energy anomaly observed in {ARPES}”. In: *Journal of Electron Spectroscopy and Related Phenomena* 181.1 (2010). Proceedings of International Workshop on Strong Correlations and Angle-Resolved Photoemission Spectroscopy 2009, pp. 31 –34. ISSN: 0368-2048. DOI: `https://doi.org/10.1016/j.elspec.2010.06.001`. URL: `http://www.sciencedirect.com/science/article/pii/S0368204810001337`.

[86] Yoshinori Okada et al. “Imaging the evolution of metallic states in a correlated iridate.” In: *Nature materials* 12.8 (2013), pp. 707–13. ISSN: 1476-1122. DOI: `10.1038/nmat3653`. arXiv: `1303.6027`. URL: `http://www.ncbi.nlm.nih.gov/pubmed/23708328`.

[87] N. Mannella et al. “Polaron coherence condensation as the mechanism for colossal magnetoresistance in layered manganites”. In: *Phys. Rev. B* 76 (23 2007), p. 233102. DOI: `10.1103/PhysRevB.76.233102`. URL: `http://link.aps.org/doi/10.1103/PhysRevB.76.233102`.

[88] T Valla et al. “Coherence-incoherence and dimensional crossover in layered strongly correlated metals”. In: *Nature* 417.6889 (2002), pp. 627–630. DOI: `http://dx.doi.org/10.1038/nature00774`.

[89] A. A. Kordyuk. “Pseudogap from ARPES experiment: Three gaps in cuprates and topological superconductivity (Review Article)”. In: *Low Temperature Physics* 41.5 (2015), pp. 319–341. DOI: `http://dx.doi.org/10.1063/1.4919371`. URL: `http://scitation.aip.org/content/aip/journal/ltp/41/5/10.1063/1.4919371`.

[90] T. J. Reber et al. “Prepairing and the “filling” gap in the cuprates from the tomographic density of states”. In: *Physical Review B - Condensed Matter and Materials Physics* 87.6 (2013). ISSN: 10980121. DOI: `10.1103/PhysRevB.87.060506`. arXiv: `1408.6084`.

[91] Christopher L. Smallwood et al. “Time- and momentum-resolved gap dynamics in $Bi_2Sr_2CaCu_2O_{8+\delta}$”. In: *Phys. Rev. B* 89 (11 2014), p. 115126. DOI: 10.1103/PhysRevB.89.115126. URL: http://link.aps.org/doi/10.1103/PhysRevB.89.115126.

[92] F. Massee et al. “Bilayer manganites: polarons in the midst of a metallic breakdown”. In: *Nature Physics* 7.9 (2011), p. 7. ISSN: 1745-2473. DOI: 10.1038/nphys2089. arXiv: 1103.3804. URL: http://arxiv.org/abs/1103.3804.

[93] P. D. C. King et al. “Spectroscopic indications of polaronic behavior of the strong spin-orbit insulator $Sr_3Ir_2O_7$”. In: *Phys. Rev. B* 87 (24 2013), p. 241106. DOI: 10.1103/PhysRevB.87.241106. URL: http://link.aps.org/doi/10.1103/PhysRevB.87.241106.

[94] S. Boseggia et al. “Antiferromagnetic order and domains in $Sr_3Ir_2O_7$ probed by x-ray resonant scattering”. In: *Phys. Rev. B* 85 (18 2012), p. 184432. DOI: 10.1103/PhysRevB.85.184432. URL: http://link.aps.org/doi/10.1103/PhysRevB.85.184432.

[95] C. M. Varma. “Theory of the pseudogap state of the cuprates”. In: *Phys. Rev. B* 73 (15 2006), p. 155113. DOI: 10.1103/PhysRevB.73.155113. URL: http://link.aps.org/doi/10.1103/PhysRevB.73.155113.

[96] M. Uchida et al. “Pseudogap of Metallic Layered Nickelate $R_{2-x}Sr_xNiO_4$ ($R = \mathrm{Nd, Eu}$) Crystals Measured Using Angle-Resolved Photoemission Spectroscopy”. In: *Phys. Rev. Lett.* 106 (2 2011), p. 027001. DOI: 10.1103/PhysRevLett.106.027001. URL: http://link.aps.org/doi/10.1103/PhysRevLett.106.027001.

[97] Y. K. Kim et al. “Fermi arcs in a doped pseudospin-1/2 Heisenberg antiferromagnet”. In: *Science* 345.6193 (2014), pp. 187–190. DOI: 10.1126/science.1251151. eprint: http://www.sciencemag.org/content/345/6193/187.full.pdf. URL: http://www.sciencemag.org/content/345/6193/187.abstract.

[98] M. Hoesch et al. “Spin structure of the Shockley surface state on Au(111)”. In: *Phys. Rev. B* 69 (24 2004), p. 241401. DOI: 10.1103/PhysRevB.69.241401. URL: https://link.aps.org/doi/10.1103/PhysRevB.69.241401.

[99] Koichiro Yaji et al. “Large Rashba spin splitting of a metallic surface-state band on a semiconductor surface”. In: *Nature Communications* 1.2 (2010), pp. 1–5. DOI: 10.1038/ncomms1016. URL: http://dx.doi.org/10.1038/ncomms1016.

[100] K Ishizaka et al. “Giant Rashba-type spin splitting in bulk BiTeI”. In: *Nature Materials* 10.7 (2011), pp. 521–526. ISSN: 1476-1122. DOI: 10.1038/nmat3051. URL: http://dx.doi.org/10.1038/nmat3051.

[101] D. Hsieh et al. “Observation of Time-Reversal-Protected Single-Dirac-Cone Topological-Insulator States in Bi_2Te_3 and Sb_2Te_3”. In: *Phys. Rev. Lett.* 103 (14 2009), p. 146401. DOI: 10.1103/PhysRevLett.103.146401. URL: https://link.aps.org/doi/10.1103/PhysRevLett.103.146401.

[102] T. Kadono et al. “Direct evidence of spin-polarized band structure of Sb(111) surface”. In: *Applied Physics Letters* 93.25 (2008), p. 252107. DOI: `10.1063/1.3049610`. eprint: `https://doi.org/10.1063/1.3049610`. URL: `https://doi.org/10.1063/1.3049610`.

[103] D. Hsieh et al. “Observation of Unconventional Quantum Spin Textures in Topological Insulators”. In: *Science* 323.5916 (2009), pp. 919–922. ISSN: 0036-8075. DOI: `10.1126/science.1167733`. eprint: `http://science.sciencemag.org/content/323/5916/919.full.pdf`. URL: `http://science.sciencemag.org/content/323/5916/919`.

[104] Kenneth Gotlieb et al. “Symmetry rules shaping spin-orbital textures in surface states”. In: *Phys. Rev. B* 95 (24 2017), p. 245142. DOI: `10.1103/PhysRevB.95.245142`. URL: `https://link.aps.org/doi/10.1103/PhysRevB.95.245142`.

[105] I Nagai et al. “Canted antiferromagnetic ground state in $Sr_3Ir_2O_7$”. In: *Journal of Physics: Condensed Matter* 19.13 (2007), p. 136214. ISSN: 0953-8984. DOI: `10.1088/0953-8984/19/13/136214`. URL: `http://stacks.iop.org/0953-8984/19/i=13/a=136214?key=crossref.b6ec9b77eca3fd86cb9dd52ea2b72faf`.

[106] Xingye Lu et al. “Doping Evolution of Magnetic Order and Magnetic Excitations in $(Sr_{1-x}La_x)_3Ir_2O_7$”. In: *Physical Review Letters* 118.2 (2017), p. 027202. ISSN: 0031-9007. DOI: `10.1103/PhysRevLett.118.027202`. URL: `http://link.aps.org/doi/10.1103/PhysRevLett.118.027202`.

[107] Chris Jozwiak et al. “Photoelectron spin-flipping and texture manipulation in a topological insulator”. In: *Nature Physics* 9 (Mar. 2013), 293 EP –. URL: `http://dx.doi.org/10.1038/nphys2572`.

[108] Kenneth Gotlieb et al. “Revealing Hidden Spin-Momentum Locking in a High Temperature Cuprate Superconductor”. In: *Science* (2018).